

**INVESTIGATION OF THE OPTICAL AND CLOUD FORMING PROPERTIES
OF POLLUTION, BIOMASS BURNING, AND MINERAL DUST AEROSOLS**

A Dissertation

by

YONG SEOB LEE

Submitted to the Office of Graduate Studies of
Texas A&M University
in partial fulfillment of the requirements for the degree of

DOCTOR OF PHILOSOPHY

May 2005

Major Subject: Atmospheric Sciences

**INVESTIGATION OF THE OPTICAL AND CLOUD FORMING PROPERTIES
OF POLLUTION, BIOMASS BURNING, AND MINERAL DUST AEROSOLS**

A Dissertation

by

YONG SEOB LEE

Submitted to Texas A&M University
in partial fulfillment of the requirements
for the degree of

DOCTOR OF PHILOSOPHY

Approved as to style and content by:

Donald R. Collins
(Chair of Committee)

Renyi Zhang
(Member)

Ping Yang
(Member)

George Kattawar
(Member)

Richard Orville
(Head of Department)

May 2005

Major Subject: Atmospheric Sciences

ABSTRACT

Investigation of the Optical and Cloud Forming Properties of Pollution, Biomass
Burning, and Mineral Dust Aerosols.

(May 2005)

Yong Seob Lee, B.S.; M.S., Pusan National University, Korea

Chair of Advisory Committee: Dr. Donald R. Collins

This dissertation describes the use of measured aerosol size distributions and size-resolved hygroscopic growth to examine the physical and chemical properties of several particle classes. The primary objective of this work was to investigate the optical and cloud forming properties of a range of ambient aerosol types measured in a number of different locations. The tool used for most of these analyses is a differential mobility analyzer / tandem differential mobility analyzer (DMA / TDMA) system developed in our research group. To collect the data described in two of the chapters of this dissertation, an aircraft-based version of the DMA / TDMA was deployed to Japan and California. The data described in two other chapters were conveniently collected during a period when the aerosol of interest came to us. The unique aspect of this analysis is the use of these data to isolate the size distributions of distinct aerosol types in order to quantify their optical and cloud forming properties.

I used collected data during the Asian Aerosol Characterization Experiment (ACE-Asia) to examine the composition and homogeneity of a complex aerosol generated in the deserts and urban regions of China and other Asian countries. An

aircraft-based TDMA was used for the first time during this campaign to examine the size-resolved hygroscopic properties of the aerosol. The Asian Dust Above Monterey (ADAM-2003) study was designed both to evaluate the degree to which models can predict the long-range transport of Asian dust, and to examine the physical and optical properties of that aged dust upon reaching the California coast. Aerosol size distributions and hygroscopic growth were measured in College Station, Texas to investigate the cloud nucleating and optical properties of a biomass burning aerosol generated from fires on the Yucatan Peninsula. Measured aerosol size distributions and size-resolved hygroscopicity and volatility were used to infer critical supersaturation distributions of the distinct particle types that were observed during this period. The predicted cloud condensation nuclei concentrations were used in a cloud model to determine the impact of the different aerosol types on the expected cloud droplet concentration. RH-dependent aerosol extinction coefficients were also calculated.

DEDICATION

To My Parents and Parents-in-Law

My Wife, Youngjin and Two Sons, Myeongshin and Jaeshin

ACKNOWLEDGEMENTS

First, I would like to thank my advisor, Dr. Don R. Collins. Throughout my research, his patience, support and direction were consistent and his scientific insights guided me to go the right way. His sincere advice has led me to pursue scientific thoughts. I want to also thank my other committee members, Dr. Renyi Zang, Dr. Ping Yang, and Dr. George Kattwar for their helpful comments during this effort.

Certainly, I also appreciate all fellows of the Aerosol Research Group who have helped me in so many ways throughout this research. Special thanks should be given to Dr. Runjun Lee and Mr. Roberto Gasparini. For many programming works, they gave me a lot of help. I would also like to thank Mr. Joshua Santarpia, Mr. Jason Tomlinson, Mr. Chris Allen, and Mr. Chance Spencer for their help and comments.

There are also a few people outside of United States that I would like to thank. Prof. Yoo-Keun Kim, Hwa-Woon Lee and Jong-Kil Park constantly providing support and love. Also Prof. Byung-Il Jeon always cheers me up.

Most importantly, not to be forgotten are my parents and parents-in-law for their support from my home country Korea. Their deepest love has been instrumental in my study here in the U.S.A. My gratitude is warmest, however, to my wife YoungJin, who followed me without complaint and always encouraged me throughout my study was neglected for long times. Special thanks also should be given to my lovely babies MyeongShin and JaeShin.

The author also acknowledges financial support from the NASA programs.

TABLE OF CONTENTS

	Page
ABSTRACT	iii
DEDICATION	v
ACKNOWLEDGEMENTS	vi
TABLE OF CONTENTS	vii
LIST OF TABLES	ix
LIST OF FIGURES.....	x
 CHAPTER	
I INTRODUCTION	1
II SIZE-RESOLVED AEROSOL HYGROSCOPICITY MEASUREMENTS ON BOARD THE TWIN OTTER DURING THE ACE-ASIA FIELD CAMPAIGN.....	6
2.1 Introduction	7
2.2 Aircraft operations.....	9
2.3 In situ measurements	10
2.4 Analysis procedure	18
2.5 Results and discussions	21
2.6 Summary and conclusion	32
III IN SITU MEASUREMENTS OF ASIAN DUST AEROSOLS OFF THE CALIFORNIA COAST.....	33
3.1 Introduction	34
3.2 Aircraft operations.....	35
3.3 In situ measurements	41
3.4 Results and discussions	45
3.5 Summary and conclusions.....	73

CHAPTER	Page
IV DERIVED CCN SPECTRA OF AN AGED BIOMASS BURNING AEROSOL	75
4.1 Introduction	76
4.2 2003 smoke episode	78
4.3 In situ measurements	82
4.4 Analysis procedure	85
4.5 Results and discussion.....	93
4.6 Summary and conclusions.....	119
V INVESTIGATION OF THE OPTICAL PROPERTIES OF AN AGED BIOMASS BURNING AEROSOL	121
5.1 Introduction	121
5.2 2003 May smoke event	123
5.3 In situ measurements	132
5.4 Analysis procedure	135
5.5 Results and discussion.....	142
5.6 Summary	158
VI SUMMARY AND CONCLUSIONS	160
REFERENCES	164
VITA	171

LIST OF TABLES

TABLE	Page
2.1 Statistical summary of hygroscopic growth factors and dominant mode standard deviations.....	30
2.2 Statistical summary of the parameter S'	31
3.1 Summary of flight level information for the Twin Otter during ADAM.....	37
3.2 Instrumentation operated on board the Twin Otter during ADAM-2003	43
3.3 Parameters prescribing dust lognormals	49
3.4 Estimated mass concentration ($\mu\text{g}/\text{m}^3$) for dust and non-dust fractions. Values in parentheses represent the fractional contribution of the dust to the total concentration.....	71
3.5 Estimated extinction coefficients (Mm^{-1}) for dust and non-dust fractions. Values in parentheses represent the fractional contribution of dust to the total extinction coefficients.....	71
3.6 Mass extinction efficiencies for dust and non-dust aerosols.....	73
4.1 The number fraction N , geometric mean diameter D_{pg} , and geometric standard deviation σ_g for the lognormals used to fit the growth factor distributions measured on May 10 at 02:20.....	90
4.2 Aerosol size distribution parameters for the five aerosol types identified in the hygroscopic growth factor distributions	107
4.3 CCN concentrations $N_{CCN}(\text{cm}^{-3})$ at different critical supersaturation. Values in parentheses represent the fractional contribution of the biomass burning aerosol to the total CCN concentration.....	114
5.1 Averaged growth factors for 25 - 600 nm diameter particles	137
5.2 Aerosol number size distribution lognormal parameters for the five aerosol types identified in the hygroscopic growth factor distributions.....	149

LIST OF FIGURES

FIGURE	Page
1.1 Global mean radiative forcing of the climate system for the year 2000, relative to 1750 [<i>IPCC</i> , 2001]	2
2.1 The sampling region of the Twin Otter during ACE-Asia	10
2.2 Growth factor distributions expected for a number of pure and mixed aerosol types.....	12
2.3 Schematic of the TDMA system operated during the ACE-Asia campaign	13
2.4 Example of the RH control accuracy during an ACE-Asia flight. The time is local standard time.....	15
2.5 Example of the sheath flow control during an ACE-Asia flight	15
2.6 Aircraft altitude and instrument RH (upper) and growth factors distributions measured with the TDMA (bottom) on 8 April 2001.....	17
2.7 Example distributions corresponding to different S' values.....	20
2.8 Histogram of the hygroscopic properties measured throughout the study. Growth factor is shown in the leftmost column, standard deviation in the center column, and the fraction of distributions containing 1, 2, or 3 modes is shown in the pie charts in the rightmost column	22
2.9 Box plots showing the median growth factor, dominant mode standard deviation, and S' parameter for all TDMA measurements made during the 12 flights considered here.....	23
2.10 Box plots of S' at each diameter for all TDMA measurements analyzed	25
2.11 Frequency of identification of one, two, or more modes	26
2.12 Box plots showing the median growth factor and standard deviation of TDMA measurements as a function of height.....	28
2.13 Box plots showing the size dependence of S' as a function of sampling height	29

FIGURE	Page
3.1 Flight tracks of the Twin Otter for flights conducted on 20, 21, and 22 April 2003.....	36
3.2 All vertical profiles of the scattering coefficient (550 nm) measured with a nephelometer. The altitude range over which dust was observed is shaded and the flight legs aimed at characterizing those layers are shown as horizontal lines	38
3.3 Ten-day backward trajectories computed using the NOAA HYSPLIT model. The trajectories terminate at the positions and altitudes of the aircraft during constant level flight legs on 20 April, 2003	39
3.4 Eight-day backward trajectories computed using the NOAA HYSPLIT model. The trajectories terminate at the positions and altitudes of the aircraft during constant level flight legs on 21 April, 2003	40
3.5 Eight-day backward trajectories computed using the NOAA HYSPLIT model. The trajectories terminate at the positions and altitudes of the aircraft during constant level flight legs on 22 April, 2003	41
3.6 Example of airborne size distribution measurements on 22 April 2003	43
3.7 Example of airborne volume distribution measurements on 22 April 2003	44
3.8 Simplistic representation of the behavior of distinct aerosol types as measured by a TDMA	46
3.9 An example of lognormal fitting of the aerosol particle hygroscopic growth factor distributions measured on 22 April 2003. Each lognormal is shaded based on the inferred composition of the aerosol within the mode it represents.....	47
3.10 An example of a dust aerosol volume size distribution (left) and number size distribution (right) measured on 22 April 2003 (L3). Circles are measured data and solid lines are lognormal fits.....	48
3.11 (A) Flight altitude and corresponding scattering coefficient at 550 nm for the flight on 20 April. The shaded box represents the segment used in this analysis. (B) Vertical profile of the scattering coefficient (550 nm) measured with the nephelometer (C) Growth factor distributions for 200, 400, and 600 nm particles. The dust distribution is shaded dark gray	52

FIGURE	Page
3.12 Size-dependent dust fraction and number, mass, and extinction coefficient distributions for 450, 550, and 700 nm determined for the aerosol sampled on 20 April. The contribution of the dust aerosol is shaded black and that of the remaining aerosol is shaded gray	54
3.13 (A) Flight altitude and corresponding scattering coefficient at 550 nm for the flight on 21 April. The shaded boxes labeled L1 and L2 represents the segments used in this analysis. (B) Vertical profile of the scattering coefficient (550 nm) measured with the nephelometer (C) Growth factor distributions for 200, 400, and 600 nm particles. The dust distribution is shaded dark gray	57
3.14 Size-dependent dust fraction and number, mass, and extinction coefficient distributions for 450, 550, and 700 nm determined for the aerosol sampled in leg L1 on 21 April. The contribution of the dust aerosol is shaded black and that of the remaining aerosol is shaded gray	59
3.15 Size-dependent dust fraction and number, mass, and extinction coefficient distributions for 450, 550, and 700 nm determined for the aerosol sampled in leg L2 on 21 April. The contribution of the dust aerosol is shaded black and that of the remaining aerosol is shaded gray	60
3.16 (A) Flight altitude and corresponding scattering coefficient at 550 nm for the flight on 22 April. The shaded boxes labeled L1, L2, and L3 represents the segments used in this analysis. (B) Vertical profile of the scattering coefficient (550 nm) measured with the nephelometer (C) Growth factor distributions for 200, 400, and 600 nm particles. The dust distribution is shaded dark gray	62
3.17 Size-dependent dust fraction and number, mass, and extinction coefficient distributions for 450, 550, and 700 nm determined for the aerosol sampled in leg L1 on 22 April. The contribution of the dust aerosol is shaded black and that of the remaining aerosol is shaded gray	64
3.18 Size-dependent dust fraction and number, mass, and extinction coefficient distributions for 450, 550, and 700 nm determined for the aerosol sampled in leg L2 on 22 April. The contribution of the dust aerosol is shaded black and that of the remaining aerosol is shaded gray	65
3.19 Size-dependent dust fraction and number, mass, and extinction coefficient distributions for 450, 550, and 700 nm determined for the aerosol sampled in leg L3 on 22 April. The contribution of the dust aerosol is shaded black and that of the remaining aerosol is shaded gray	66

FIGURE	Page
3.20 Closure comparisons between directly measured and derived total scattering coefficient for 450, 550, and 700 nm wavelengths	68
3.21 Closure comparisons between directly measured and derived hemispherical backscattering coefficient for 450, 550, and 700 nm wavelengths	69
3.22 Averaged mass extinction efficiencies for dust and non-dust aerosols	72
4.1 Measurement locations and maximum PM 2.5 concentrations on May 10, 2003 (circle: Texas A&M University, triangles: TCEQ sites)	78
4.2 Hourly PM 2.5 concentrations at four TCEQ cities during the measurement period.	80
4.3 Time series of visibility, temperature, and relative humidity recorded at Eastwood airport in College Station, Texas. Along the x-axis, 8.0 corresponds to midnight on May 8, and 8.5 corresponds to noon on May 8	80
4.4 PM2.5 concentrations recorded in Houston and Galveston during the smoke episode in May, 2003. The light shaded area in each graph represents the average PM2.5 concentration measured at each of the sites during the same time period in May of 2002	81
4.5 Box plots of hourly PM 2.5 mass concentrations recorded at four cities in Texas in the month of May between 2000 and 2003	82
4.6 Fixed-RH hygroscopic growth factor distributions measured at 02:20 CDT on 10 May 2003	88
4.7 Example lognormal curve fits to growth factor distributions for 50, 100 and 600 nm particles on 10 May 2003. The dotted lines represent the lognormal fits, while the solid lines represent the measured distributions	89
4.8 All aerosol size distributions measured during the smoke episode. The solid line represents the measurement made at 02:20 on 10 May 2003	91
4.9 Size-resolved fractional categorization of the aerosol (top) and single particle-type size distributions (bottom) for the aerosol measured during the sequence centered at 02:20 CDT on May 10, 2003	92
4.10 Number and volume distributions of the aerosol measured during the biomass burning aerosol event	94

FIGURE	Page
4.11 Measured hygroscopic growth factor distributions for particles with diameters between 25 and 600 nm	96
4.12 Plots of RH scan data from May 7 to 8, 2003 for 50, 100, 200 nm	98
4.13 Plots of RH scan data from May 8 to 9, 2003 for 50, 100, 200 nm	99
4.14 Plots of RH scan data from May 10 to 11, 2003 for 50, 100, 200 nm	100
4.15 Plots of volatility scan data from 02:20 10 May 2003 for 50, 100, and 200 nm	102
4.16 Plots of volatility scan data from 17:00 10 May 2003 for 50, 100, and 200 nm	103
4.17 Plots of volatility scan data from 02:00 11 May 2003 for 50, 100, and 200 nm	104
4.18 Partitioned size distributions during the measurement period	106
4.19 Differential (top) and cumulative (middle) CCN spectra for each of the measurement sequences completed between 7 and 8 May 2003. The bottom graphs show the fractional contribution of each of the aerosol types to the cumulative CCN concentration.	109
4.20 Differential (top) and cumulative (middle) CCN spectra for each of the measurement sequences completed between 9 and 10 May 2003. The bottom graphs show the fractional contribution of each of the aerosol types to the cumulative CCN concentration	110
4.21 Differential (top) and cumulative (middle) CCN spectra for each of the measurement sequences completed between 10 and 11 May 2003. The bottom graphs show the fractional contribution of each of the aerosol types to the cumulative CCN concentration	111
4.22 Total CCN concentrations $N(cm^{-3})$ at different critical supersaturation	112
4.23 Time-dependent inferred total and biomass burning-only CCN concentration	113

FIGURE	Page
4.24 Biomass burning fractional contribution to the total CCN concentration as a function of critical supersaturation.....	114
4.25 CCN spectra normalized by aerosol number concentration (top), mass concentration (middle), and scattering coefficient (bottom). The solid line represents the mean value and the shaded area bounds +/- one standard deviation.....	116
4.26 Cloud droplet number concentration as a function of updraft speed.....	118
4.27 Ratio of cloud drop number concentration calculated when both the biomass burning and sulfate aerosol entered the modeled cloud to that when only the biomass burning aerosol entered	119
5.1 Locations of measurement sites (Circle: Texas A&M University, triangle: TCEQ, square: IMPROVE).....	124
5.2a Example back trajectories ending in College Station, Texas on 7 May 2003	126
5.2b Example back trajectories ending in College Station, Texas on 10 May 2003 ..	127
5.3 Earth Probe GRID TOMS Aerosol index on 7 (left) and 10 May 2003 (right). Index maxima and minima for the two days are 2.4 and -2.5, and 2.8 and -2.1, respectively.....	128
5.4 Aerosol extinction coefficients calculated from compositionally-resolved aerosol mass concentration at Big Bend National Park and Wichita Mountains during April-May 2003	129
5.5 Time series of visibility and relative humidity recorded at Easterwood airport in College Station. Along the x-axis, 9.0 corresponds to midnight on May 9, and 9.5 corresponds to noon on May 9	131
5.6 PM _{2.5} concentrations in Galveston and Houston during the smoke episode in 2003. The light shaded region represents the average PM _{2.5} concentration measured at these locations over the same time period in 2002.....	131
5.7 Schematic of the DMA / TDMA system operated in College Station	133
5.8 Hygroscopic growth factor distribution measured at 09:40 CDT 10 May 2003.....	136

FIGURE	Page
5.9 All aerosol size distributions measured during the smoke episode	138
5.10 Top graph shows the size-dependent fractional contribution of each of the particle types considered to the overall size distribution. The bottom graph shows the measured total size distribution and the calculated distributions for each of the different particle types.....	140
5.11 Evolution of the aerosol number size distribution during the four-day sampling period	143
5.12 Hygroscopic growth factor distributions for each of the seven particle sizes for which measurements were made.....	144
5.13 a) HS-TDMA measurements and b) HT-TDMA measurements on 10 May 2003. Solid markers represent growth factors measured as the RH was decreased, while hollow markers represent growth factors measured as the RH was increased. Separation between these measurements at a given RH indicates that deliquescent particles are present. Marker size reflects the concentration within each mode when multiple modes were present	146
5.14 Partitioned size distributions	148
5.15 Contour plot of biomass burning aerosol extinction coefficient distribution for a wavelength of 550 nm.....	151
5.16 Aerosol extinction coefficients at ambient and 40% RH at a wavelength of 550 nm.....	152
5.17 Variation of aerosol extinction coefficients at 550 nm as a function of relative humidity	152
5.18 Dependence of specific aerosol class extinction coefficients at 550 nm on relative humidity.....	153
5.19 Mass extinction efficiency for biomass and non-biomass burning aerosols for a wavelength of 550 nm.....	154
5.20 Extinction and back scattering coefficients at 532 nm and 1064 nm as functions of particle diameter and RH at 09:40 on 10 May 2003	155
5.21 Time series of the calculated lidar ratio at 532 and 1064 nm at ambient RH	156

FIGURE	Page
5.22 Time series of the lidar ratio at 532 nm and 1064 nm as a function of RH	157
5.23 RH-dependence of the lidar ratio normalized by the lidar ratio calculated at 30% RH. The means and standard deviations are shown for each RH	158

CHAPTER I

INTRODUCTION

The influence of aerosols resulting from human activities on climate and clouds is still poorly understood. The emitted particles alter the Earth's radiation budget directly by scattering and absorbing solar and infrared radiation and indirectly by changing cloud lifetime and albedo. The level of scientific understanding of these impacts is very low due to the complex relationships between aerosol mass, cloud condensation nuclei (CCN) concentration, and optical behavior [IPCC, 2001]. Figure 1.1 shows current estimates of the radiative forcing due to changes over the past 250 years. The vertical line about the rectangular bars indicates a range of estimates, guided by the spread in the published values of the forcing and on our physical understanding of the impacts. No estimates of the mean forcing due to changes in mineral dust concentrations and due to cloud / aerosol interactions are provided because remaining uncertainties are so large. Much of the uncertainty in these and the other aerosol effects results from inadequate data describing the vertical and horizontal distribution of the particulates [IPCC, 2001].

In order to accurately determine the impacts of aerosols, it is necessary to ensure that observations reflect the actual spatial and temporal heterogeneity. Several field studies combining ground-, ship-, aircraft-, and satellite-based measurements have been conducted in the past decades that have aimed to provide the necessary dataset. Most of these have been conducted in locations downwind of major aerosol source

This dissertation follows the style and format of the *Journal of Geophysical Research*.

regions. My analysis of mineral dust aerosol will focus on data collected during two such studies, the Asian Aerosol Characterization Experiment (ACE-Asia) and the Asian Dust Above Monterey (ADAM) study. In contrast to these highly coordinated studies, our measurements of biomass burning aerosol were made independently, directly from our lab in College Station, Texas.

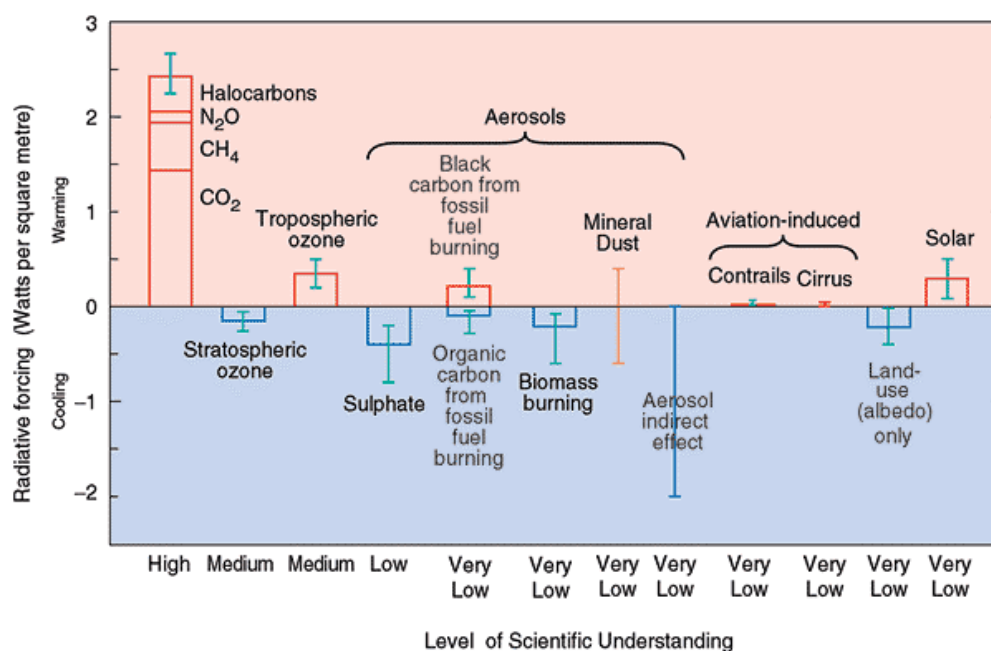


Figure 1.1 Global mean radiative forcing of the climate system for the year 2000, relative to 1750 [IPCC, 2001].

ACE-Asia was conducted in the spring of 2001 in a region centered roughly on the southern end of Japan. Three aircraft, two research ships, a network of lidars, and many surface sites were employed during the study to investigate the chemical, physical, and optical properties of the local aerosol. Of greatest interest were pollution aerosols originating from the major industrial regions in China, Korea, and Japan, and mineral

dust aerosols generated in the Gobi desert. Our group operated a tandem differential mobility analyzer (TDMA) on the Center for Interdisciplinary Remotely Piloted Aircraft Studies (CIRPAS) Twin Otter aircraft to measure the hygroscopic growth behavior of the aerosol. Although the locations at which dust concentrations were greatest were typically out of range of the Twin Otter, significant dust loadings were measured during several of the flights.

ADAM was also aimed at assessing the transport and properties of Asian dust. Unlike ACE-Asia, the dust was sampled after being transported thousands of kilometers across the Pacific Ocean. One of the primary objectives of this project was testing the ability of the Naval Research Laboratory Aerosol Analysis and Prediction System (NAAPS) model to predict the radiative properties of dust reaching the coast of California. Our research group again operated a TDMA on board the CIRPAS Twin Otter during this project. Although no major dust event was captured during the study, elevated concentrations were measured during a several-day period near the end of the project.

Intentionally set fires in agricultural regions on and near the Yucatan Peninsula generate elevated concentrations of particulates that impact aerosol loadings in the U.S. every spring. The severity of these episodes varies widely depending on the rainfall received preceding the burning season and the meteorology that is responsible for the transport to the U.S. Biomass burning aerosol loadings in Texas during May of 2003 were significantly higher than during the previous four years. Our group took advantage of this unique opportunity to measure the concentration and properties of this aged

aerosol. Unlike the analysis of data from ACE-Asia and ADAM, no complementary measurements were available to aid in interpreting the data. Even so, the range of measurements made with our TDMA system was sufficient to permit examination of many of the important properties of the biomass burning aerosol.

The primary objective of this research is to examine the optical and cloud forming properties of specific classes of aerosols. With very few exceptions, ambient aerosols are composed of mixtures of a range of different particle types. Therefore, it is necessary to isolate individual aerosol classes based on observable physical or chemical properties. This cannot be accomplished through bulk measurements such as those of light scattering intensity or CCN concentration. Instead, the properties of interest are predicted through a combination of measured size distributions and measured size-resolved behavior. Most of the analysis is based on size-resolved measurements of aerosol hygroscopic growth. Measured hygroscopicity is typically quantified by the growth factor (GF), which is simply the ratio of the diameter of a particle following exposure to high RH (D_p) to its initial, or dry, diameter at low RH, D_p^* .

The primary objectives of this research are:

- (1) Determine the light scattering properties of Asian dust particles from measured aerosol size distributions and hygroscopic growth on board the CIRPAS Twin Otter
 - i) off the coast of California during ADAM, and ii) off the coast of Japan during ACE-Asia. The interaction of dust and anthropogenic emissions will also be investigated. The predicted light scattering behavior will be compared with that measured directly with a nephelometer.

- (2) Determine the light scattering and cloud forming properties of biomass burning aerosols transported to the U.S. from the Yucatan Peninsula during May of 2003.

These data are used to assess the evolution of the aerosol during the 1.5 day transit time to College Station. The predicted CCN concentrations are used in a cloud parcel model to determine the impact of the different aerosol types on the expected cloud droplet concentration.

CHAPTER II

SIZE-RESOLVED AEROSOL HYGROSCOPICITY MEASUREMENTS ON BOARD THE TWIN OTTER DURING THE ACE-ASIA FIELD CAMPAIGN

A tandem differential mobility analyzer (TDMA) system on board the Center for Interdisciplinary Remotely Piloted Aircraft (CIRPAS) Twin Otter aircraft was used to measure aerosol hygroscopic properties during the Aerosol Characterization Experiment (ACE)–Asia campaign from 31 March to 1 May 2001. Two high flow differential mobility analyzers (DMA, Aerosol Dynamics, Inc.) were used to maximize the count rate, which was essential for these and other aircraft measurements. Hygroscopic growth factor distributions of particles having initial diameters of 40, 59, 86, 126, 186, 273, 400, and 586 nm were measured during 19 research flights. Data collected during 12 of those flights were used for the analysis described here. Measured hygroscopicity was used to investigate aerosol mixing state and to gain insight into composition. In contrast to measurements made in urban regions, growth factor distributions were typically dominated by a single hygroscopic mode having a growth factor that usually exceeded 1.4 for all particle sizes considered. Consistent with measurements made in other locations by our research group and others, growth factors tended to increase with increasing particle size. Bimodal growth factor distributions were most often observed for particles larger than 86 nm, which indicates that multiple particle types were sometimes present. The standard deviation of the growth factor distributions generally increased with increasing particle size, although this trend often reversed for the largest

particles analyzed. The uniformity in size-resolved hygroscopicity was quantified to facilitate comparison between measurements made on different days and at different altitudes.

2.1 Introduction

The Asian Aerosol Characterization Experiment (ACE-Asia) was organized by the International Global Atmospheric Chemistry (IGAC) Program to investigate the influence of atmospheric aerosols on Earth's climate system [Huebert *et al.*, 2003]. In order to accurately determine the impacts of aerosols, it is necessary to ensure that observations reflect the actual spatial and temporal heterogeneity. ACE-Asia is one of a number of recent field studies that have combined ground-, ship-, aircraft-, and satellite-based measurements to provide the necessary dataset. Most of these intensive studies have been conducted in locations downwind of major aerosol source regions. ACE-Asia was conducted in the spring of 2001 in a region centered roughly on the southern end of Japan. Multiple aircraft and research ships, a network of lidars, and several surface sites were employed during the study to investigate the chemical, physical, and optical properties of the local aerosol. Of greatest interest were pollution aerosols originating from the major industrial regions in China, Korea, and Japan, and mineral dust aerosols generated in the Gobi desert. A number of scientists measured vertical and spatial distributions of aerosol concentrations and properties on board the Center for Interdisciplinary Remotely Piloted Aircraft Studies (CIRPAS) Twin Otter aircraft. Similar measurements on board a slightly smaller aircraft during the ACE-2 study were

described by *Collins et al.* [2000]. *Wang et al.* [2002] evaluated the extent to which aerosol physical and chemical properties measured on board the Twin Otter could be used to predict light scattering and extinction coefficients. A range of instruments including a DMA, an aerodynamic particle sizer (APS), and a micro-orifice uniform deposit impactor (MOUDI) were used in that analysis. That study focused primarily on comparison with extinction coefficients determined by measuring the altitude-resolved aerosol optical thickness using the 14-wavelength NASA Ames Airborne Tracking Sun photometer (AATS-14). *Bahreini et al.* [2003] described the first ever aircraft measurements of time-resolved aerosol composition using an Aerodyne aerosol mass spectrometer (AMS). Their analysis focused on the size distributions of sulfate, nitrate, ammonium, and organic compounds. Observed concentrations of sulfate and organic aerosol mass were as high as $10 \mu\text{g m}^{-3}$ and $13 \mu\text{g m}^{-3}$, respectively. *Gao et al.* [2003] described compositional analysis of aerosols collected on filters and impactor substrates on board the Twin Otter. They observed that composition was both vertically and spatially inhomogeneous during the study period.

Our group operated a TDMA on board the Twin Otter aircraft to measure size-resolved hygroscopic growth of the aerosol. The hygroscopic properties of an aerosol directly influence its overall radiative properties, although this link to the overall goals of ACE-Asia was of secondary importance for the measurements and subsequent analysis. The primary motivation for operation of a TDMA during the study was to better understand both the size-resolved composition of submicron particles and the association of different classes of compounds. Unlike the data provided by most other

measurement techniques, hygroscopicity can be used to infer the mixing state of the aerosol. In addition to the TDMA system, two other instruments were operated on board the Twin Otter to examine the hygroscopic behavior of the aerosol. *Gao et al.* [2003] described the impact of aerosol hygroscopicity on light scattering based on data collected with three nephelometers, each of which was operated at a different relative humidity (RH). The overall influence of hygroscopic growth on the submicron size distribution was measured using parallel differential mobility analyzers operated at different RH [*Wang et al.*, 2002]. Although the other measures of aerosol hygroscopicity lack the size resolution afforded by a TDMA, they do benefit from sampling times that are substantially shorter than those needed for a series of TDMA measurements. In addition to the goal of characterizing aerosol mixing state, the TDMA data were also useful for identification of non-hygroscopic submicron dust particles. Although the locations at which dust concentrations were greatest were typically out of range of the Twin Otter, significant dust loadings were measured during several of the flights.

2.2 Aircraft operations

To adequately characterize pollution and dust plumes typical of the study region, several aircraft were employed during the project. The Twin Otter completed 19 flights originating from the Iwakuni Marine Corps Air Station (IMCAS), Japan from March 31 to May 1, 2001. Figure 2.1 shows the region in which the ACE-Asia study was conducted. The analysis here focuses on 12 flights for which the collected TDMA data

were of the highest quality. These flights were conducted on April 8, 9, 12, 13, 17, 19, 20, 23, 25, 26, 27 and 28.

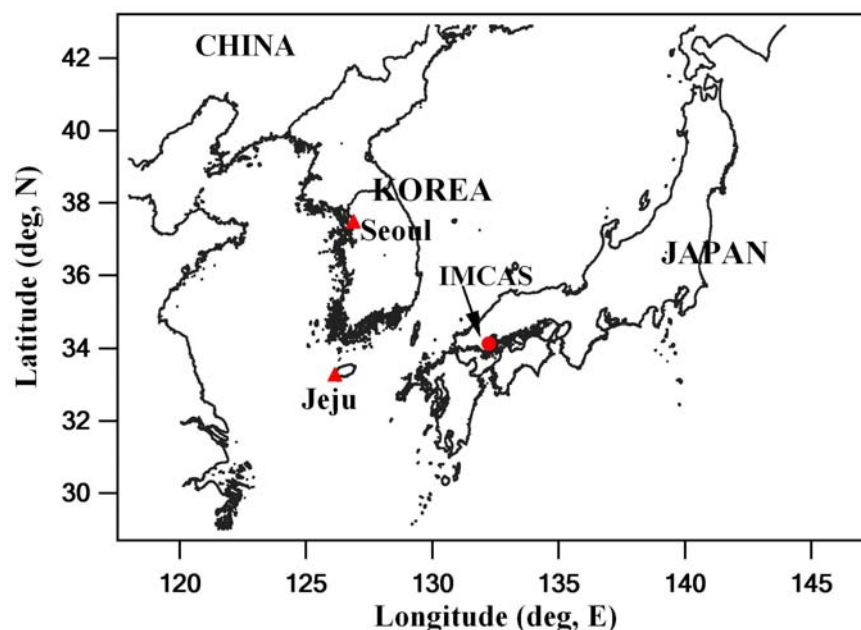


Figure 2.1. The sampling region of the Twin Otter during ACE-Asia.

2.3 In situ measurements

2.3.1 Aerosol growth factor measurement

Hygroscopic properties of particles have been examined through the use of humidified TDMA systems in several areas. A summary of recent applications is included in Cocker *et al.* [2001]. A humidified TDMA consists of two DMAs in series, between which the aerosol is exposed to an elevated RH. The voltage applied to the first DMA is fixed to select a monodisperse aerosol. Following exposure to high RH, the initially monodisperse aerosol enters the second DMA in which the applied voltage is

continuously varied to characterize the resulting size distribution of the humidified aerosol. In this way, the change in particle size due to interaction with water vapor is determined. The hygroscopic growth factor (GF) distribution of the aerosol is described by the resulting size distribution with the final particle size following exposure to high RH (D_p) normalized with respect to the initial dry particle size, D_p^* . Figure 2.2 depicts the growth factor distributions that are expected for a number of pure and mixed aerosol types. An inversion algorithm is used to relate the measured counts array to growth factor distributions. The composition of an ambient aerosol can be inferred through a combination of a measured hygroscopic growth factor distribution and the expected hygroscopicity of pure aerosol types such as ammonium sulfate and soot. The schematic of the TDMA system operated during ACE-Asia is shown in Figure 2.3. The primary components of this instrument are the two DMAs, a Condensation Nuclei Counter (CNC), and a humidity conditioner.

Hygroscopic growth factor distributions of particles having dry diameters from 40 to 586 nm were sequentially measured over a period of approximately 45 minutes. The exact time needed to complete a measurement was dependent upon the aerosol concentration since the instrument advanced to the next particle size only after sufficient particle counts were recorded. Aerosol Dynamics, Inc. high flow DMAs were used in the instrument to maximize count rate in order to minimize the integration time necessary. Relative to the commonly used TSI 3071, these DMAs operate with 6.7 times higher flow rates for a given particle size and applied voltage.

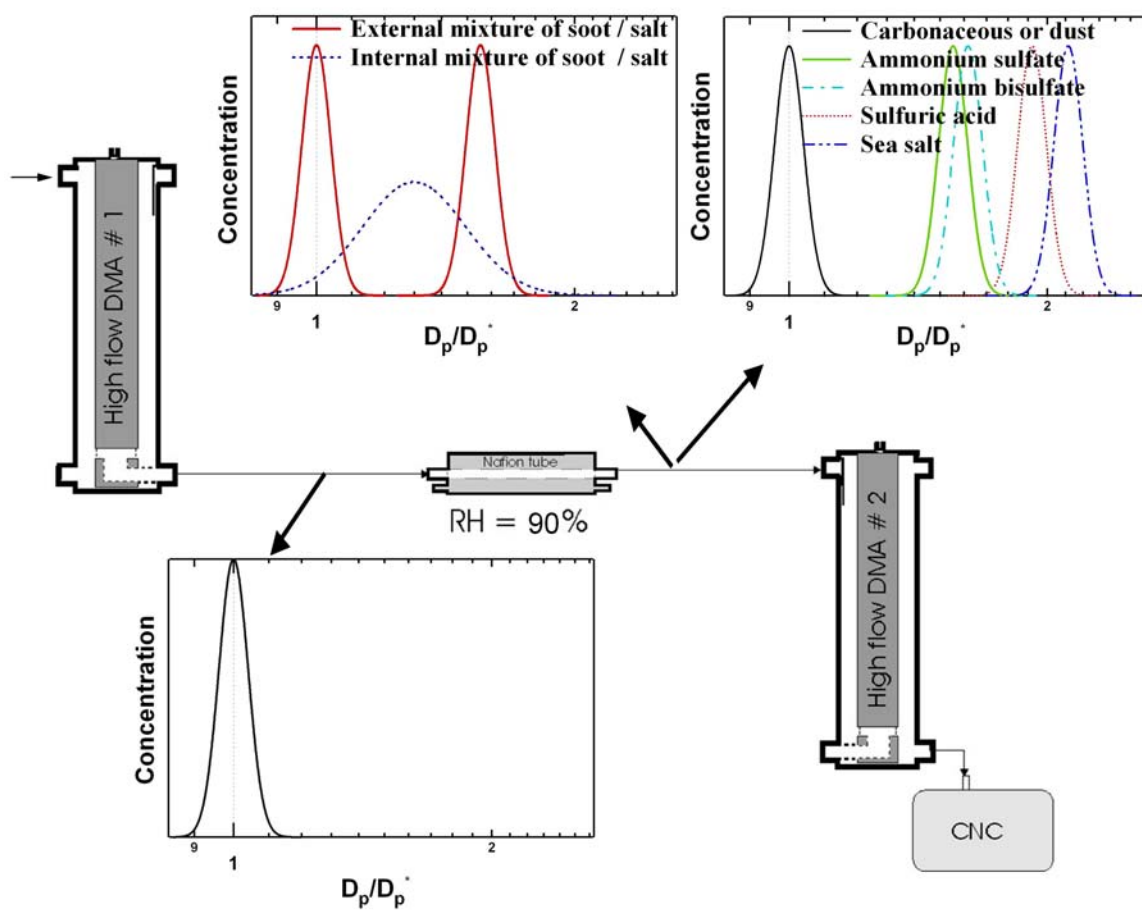


Figure 2.2. Growth factor distributions expected for a number of pure and mixed aerosol types.

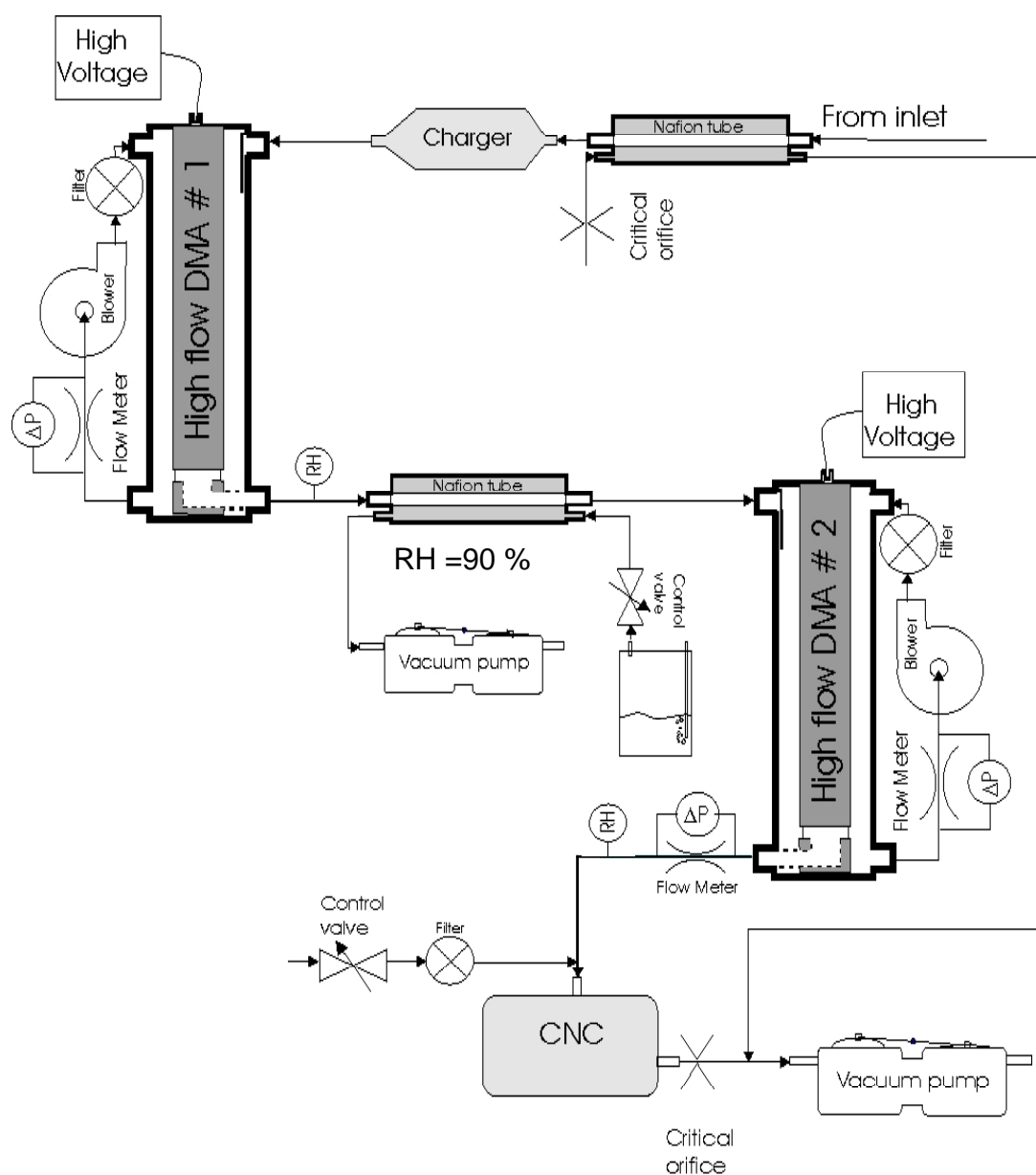


Figure 2.3. Schematic of the TDMA system operated during the ACE-Asia campaign.

Humidity control was achieved by varying the pressure of an initially saturated air stream through the use of a proportional control valve. The pressure reduction across the valve orifice is reflected in an equivalent fractional decrease in water vapor content. This flow is used as the purge flow through a custom Nafion tube bundle. The water vapor pressure in the sample flow inside the Nafion tubes equilibrates with that in the purge flow surrounding the Nafion tubes. In this way, humidity can be controlled accurately between approximately 20% and 90% through the use of a simple LabVIEW PID (Proportional, Integral and Differential) control algorithm. Figure 2.4 shows an example of the RH control accuracy during an ACE-Asia flight on 8 April 2001. The time shown in this figure and hereafter is local standard time.

Variable speed regenerative blowers were used to control the DMA sheath and excess flows over a wide flow rate range. Recirculation of the sheath / excess flows in this way simplifies flow control, and minimizes the amount of flow to be humidified, although it also limits the speed at which RH can be changed. However, even with independent RH control of the sample and sheath flows, the rate at which RH could be controlled would be only slightly improved due to the slow response of Nafion tubes. Figure 2.5 shows an example of the sheath flow control during an ACE-Asia flight on 8 April 2001. The step changes in flow rates shown in the figure reflect changes in particle size analyzed.

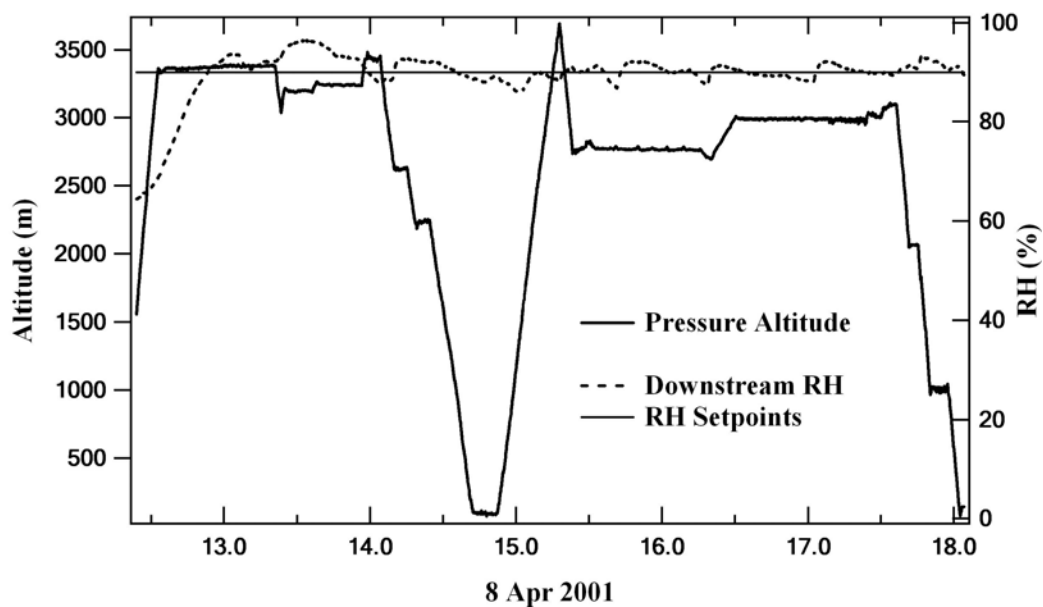


Figure 2.4. Example of the RH control accuracy during an ACE-Asia flight. The time is local standard time.

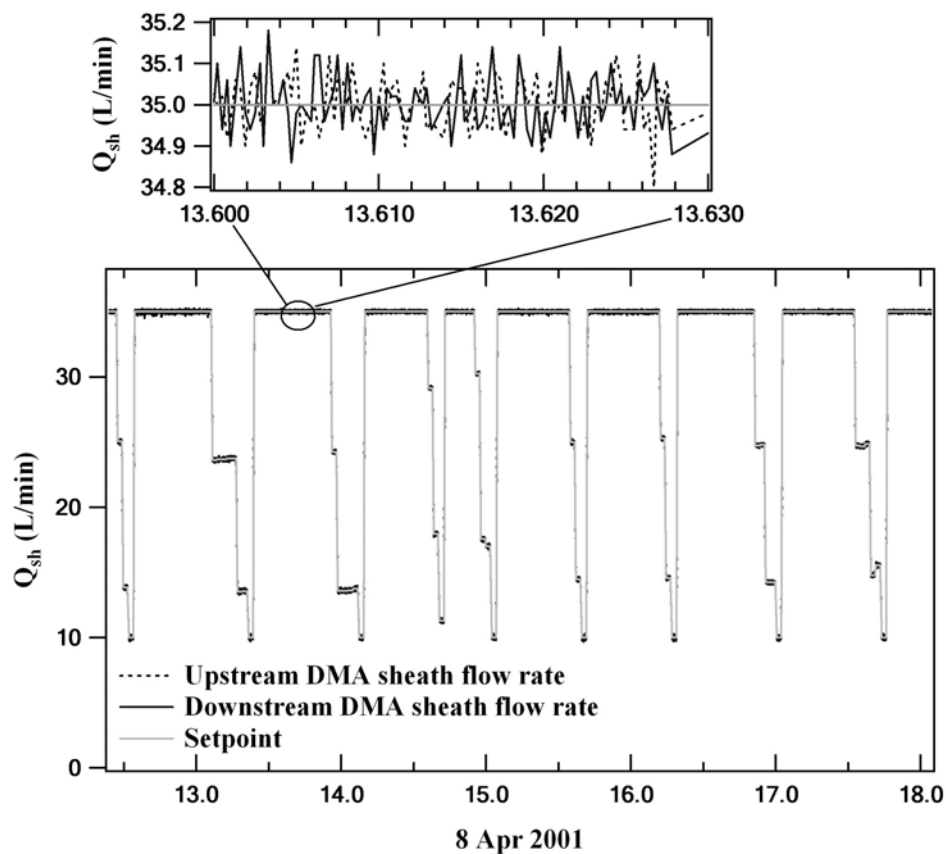


Figure 2.5. Example of the sheath flow control during an ACE-Asia flight.

2.3.2 Example data collected during one flight

From the 12 research flights considered in this analysis, data collected during one flight are shown to illustrate the appearance of the distributions used in the subsequent analyses. The aircraft altitude and TDMA RH during the flight on 8 Apr 2001 are shown in the top graph in Figure 2.6. Hygroscopic growth factor distributions for dry particle diameters of 40, 59, 86, 126, 186, 273, 400, and 586 nm are shown in the lower graphs. The numbers included in each graph link the measured distributions with the corresponding sampling interval identified in the top graph. T1 correspond to 40 nm, T2 corresponds to 59 nm, and so on. The aircraft remained at approximately 3000 m for most of this flight. The breadth of the growth factor distribution for the largest particles considered is in part due to low count rates. The presence of very hygroscopic 40 nm particles during several of the sampling intervals suggests recent nucleation of sulfuric acid particles. As was true for the majority of flights, most distributions measured on this date are monomodal, which suggests that the aerosol was internally mixed. This observation is not surprising given the relatively long transit time from source regions in China and Korea. Nevertheless, the sensitivity of radiative and cloud nucleating properties of the aerosol to the mixing state makes this an important observation. Although growth factors varied as a function of size and time during the flight, most distributions were centered at approximately 1.4 to 1.6, which suggests the aerosol was most likely composed of a mixture of sulfate and some less soluble species such as organics.

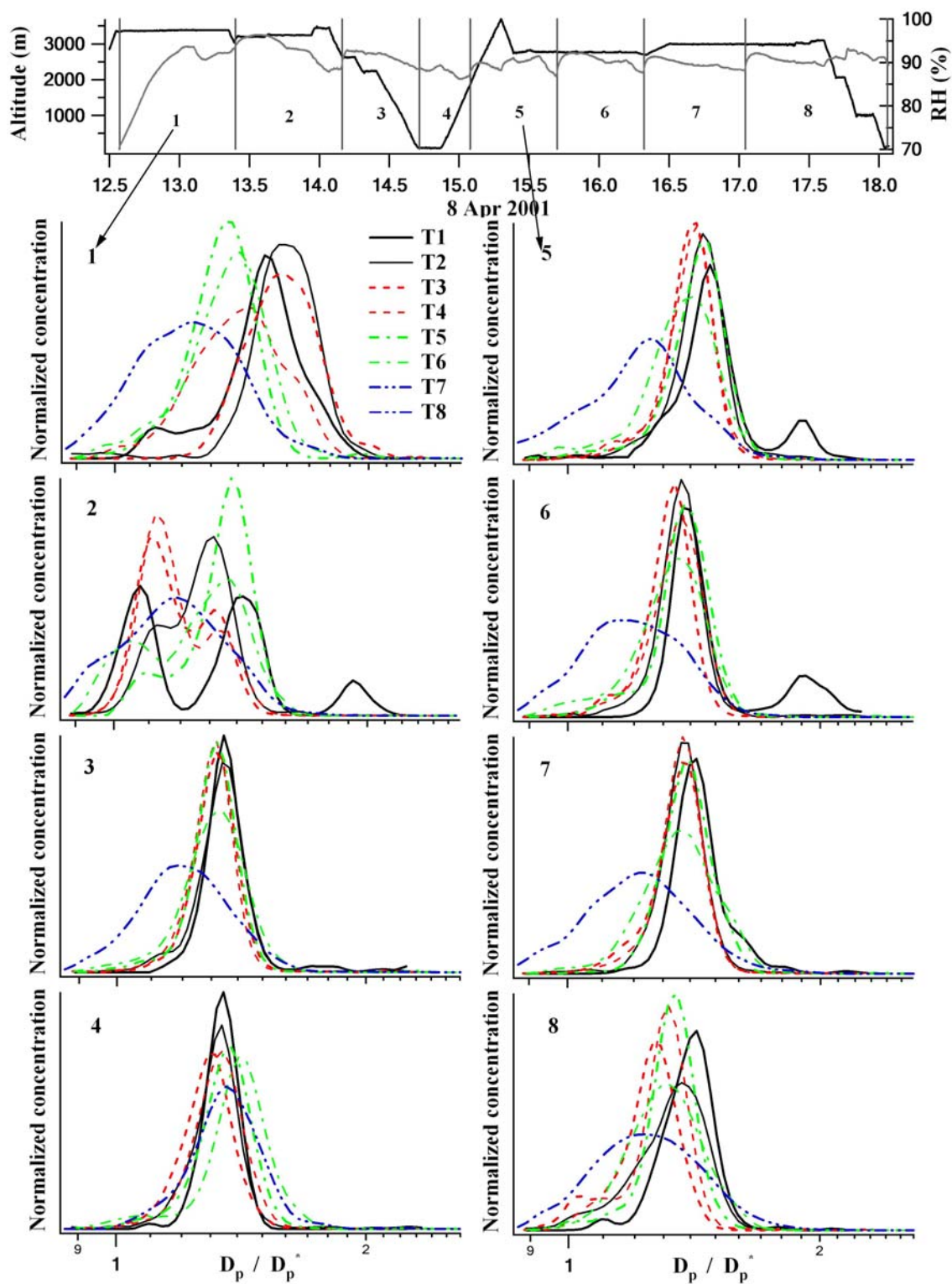


Figure 2.6. Aircraft altitude and instrument RH (upper) and growth factors distributions measured with the TDMA (bottom) on 8 April 2001.

2.4 Analysis procedure

2.4.1 Parameterizations of growth factors

The lognormal distribution often provides a good fit of aerosol size and hygroscopicity distributions, and is regularly used in atmospheric applications [Seinfeld and Pandis, 1998]. Computer software was developed to fit each hygroscopic growth factor distribution with between one and four lognormals. Each lognormal is prescribed by a geometric mean diameter (or equivalently, growth factor), a mode concentration, and the geometric standard deviation of the mode through the following expression,

$$\frac{dN_i}{d \log D_p} = \frac{N_i}{\sqrt{2\pi} \cdot \log(\sigma_{g,i})} \exp \left[-\frac{(\log D_p - \log D_{pg,i})^2}{2 \cdot (\log \sigma_{g,i})^2} \right], \quad (2.1)$$

where N_i is the total number concentration, $D_{pg,i}$ is the geometric mean diameter, and $\sigma_{g,i}$ is the geometric standard deviation for mode i .

2.4.2 Parameterizations of geometric standard deviation

The compositional heterogeneity of an aerosol is reflected in the spread in the hygroscopic growth factor distribution. One measure of this spread is the geometric standard deviation of lognormals used to fit each of the modes within a growth factor distribution. The greater the standard deviation, the more varied is the composition of particles of a given size. The limiting minimum standard deviation is a function of the finite resolution of the two DMAs. Although this minimum is dependent upon operating conditions and sources of error in the instrument or analysis, a value of about 1.035 is reasonable for this analysis. While comparison of the geometric standard deviation of

the dominant hygroscopic mode measured for different particle sizes and during different flights provides some detail of the compositional uniformity, it does not reflect the inhomogeneity characterized by the presence of multiple modes. Therefore, the approach taken here to quantify the breadth of each hygroscopic growth factor distribution was to calculate a geometric standard deviation, S , for an entire distribution.

$$S = \frac{\sum_{i=0}^j N(\overline{GF} / GF_i)}{\sum_{i=0}^j N} + \frac{\sum_{i=j}^{\infty} N(GF_i / \overline{GF})}{\sum_{i=j}^{\infty} N}, \quad (2.2)$$

where \overline{GF} , $\frac{\sum N \cdot GF}{\sum N}$, is the mean growth factor for each distribution, and j represents

the bin at which the growth factor is nearest the mean growth factor. Rather than directly comparing the absolute values of these standard deviations, each is normalized to that corresponding to a compositionally homogeneous aerosol having a growth factor distribution described by a single lognormal with a geometric standard deviation of 1.035. The new parameter, S' , is defined as

$$S' = \frac{S_{Dist}}{S_{1.035}}. \quad (2.3)$$

$S_{1.035}$ is the minimum achievable geometric standard deviation, and S_{Dist} is that calculated for a measured distribution. Figure 2.7 shows example distributions that result in a range of geometric standard deviations. Both the geometric standard deviation of the dominant mode in a given hygroscopic growth factor distribution, and the normalized geometric standard deviation of a complete hygroscopic growth factor

distribution will be used to describe the compositional uniformity of the aerosol. These will be referred to as the dominant mode standard deviation and the entire distribution standard deviation, respectively.

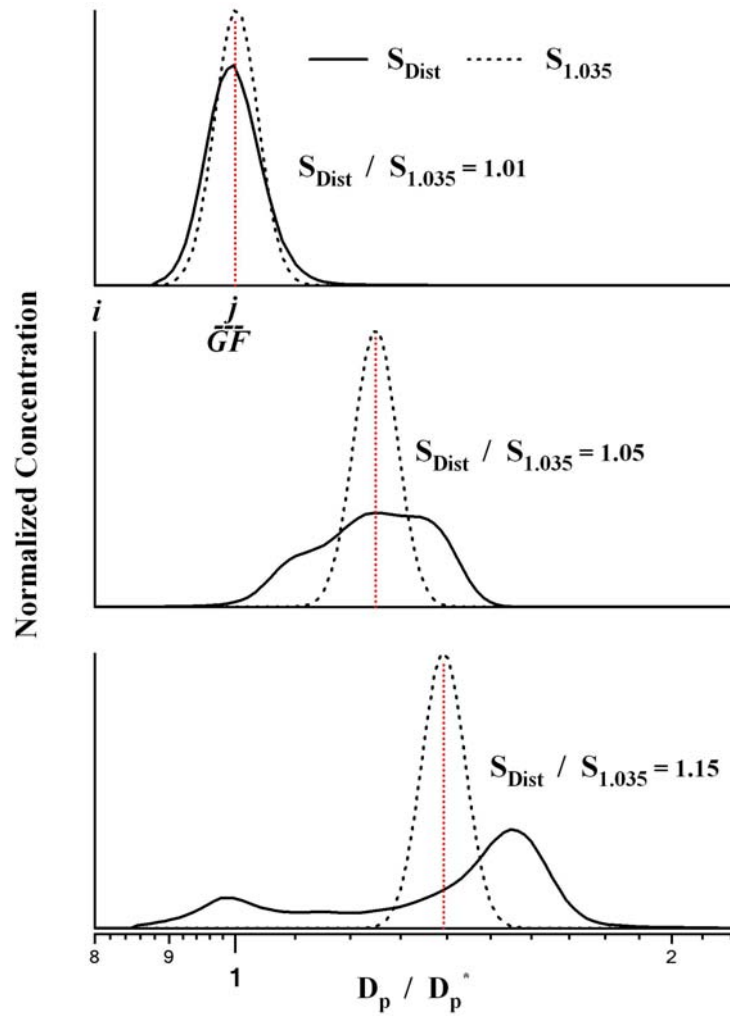


Figure 2.7. Example distributions corresponding to different S' values.

2.5 Results and discussions

2.5.1 Study-average hygroscopic properties

Statistics of measured growth factor distributions during 12 of the 19 total research flights are shown in Figure 2.8. The plots in the leftmost column of Figure 2.8 show histograms of the median growth factor for each particle size analyzed. The vertical dotted line represents the growth factor of pure ammonium bisulfate at 90% RH for each diameter. Compared to measurements made in an urban area [*Gasparini et al.*, 2004], there are relatively few non-hygroscopic modes for particles smaller than 273 nm. Hygroscopic growth factor distributions for particles 273 nm and larger did occasionally possess a non-hygroscopic mode, which was probably composed of dust particles during at least some of the flights. The plots in the center column are histograms of the normalized standard deviation of growth factor distributions. The shift in these histograms to greater standard deviation with increasing particle size suggests a greater degree of heterogeneity with the larger particles considered. The exact cause of this size dependence is not understood. Condensational growth of an aerosol population tends to tighten the size distribution and result in a more compositionally uniform aerosol, which is inconsistent with these observations. A greater concentration of primary particles at larger sizes, which are typically less hygroscopic than secondary particles, may contribute to the observed trend. The size dependence of the hygroscopic behavior of the aerosol is summarized in Figure 2.9. In these graphs, the lower and upper edges of the boxes represent the 25th and 75th percentile values, respectively, while the lower and upper whiskers represent the 10th and 90th percentiles, respectively. The horizontal lines near the center of each box represent the median.

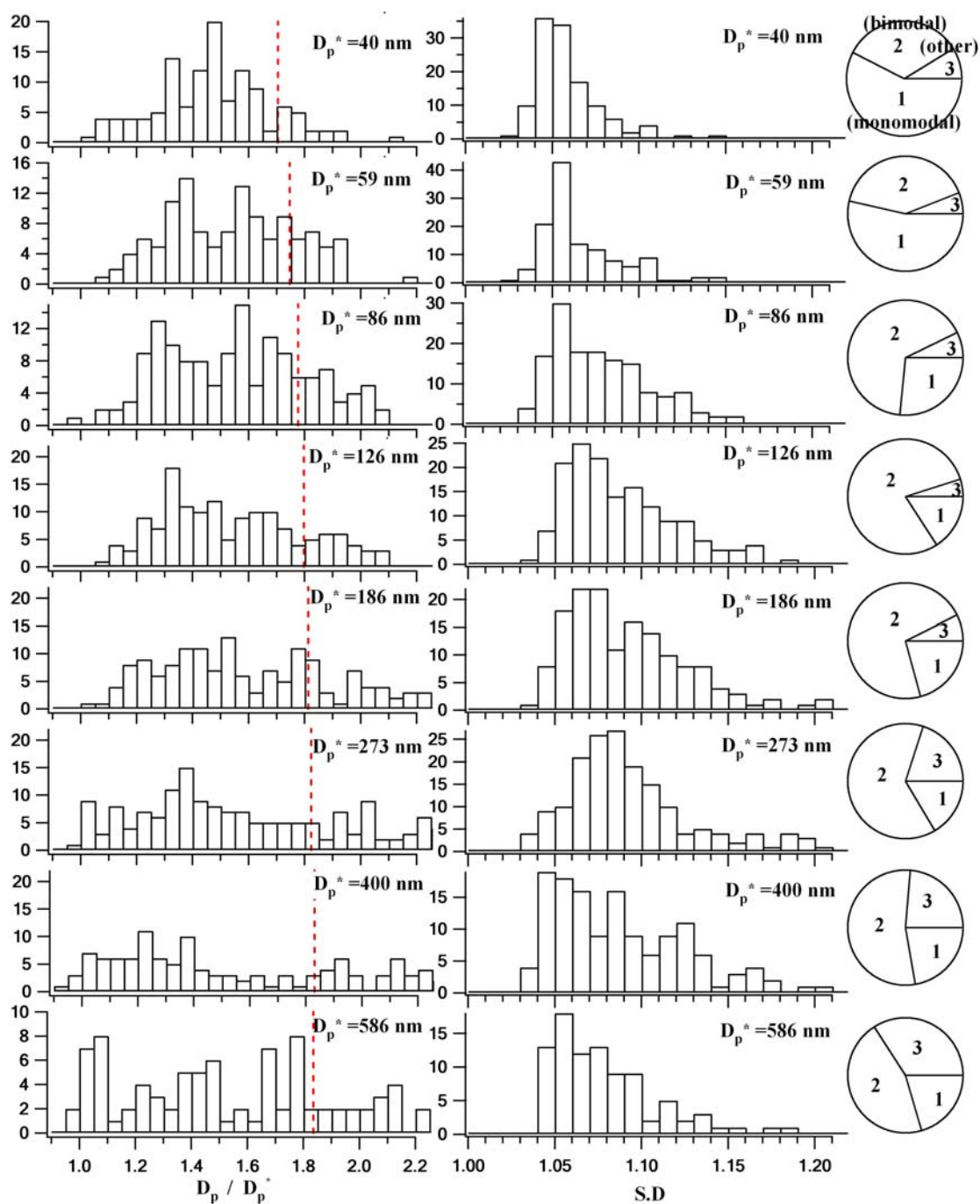


Figure 2.8. Histogram of the hygroscopic properties measured throughout the study. Growth factor is shown in the leftmost column, standard deviation in the center column, and the fraction of distributions containing 1, 2, or 3 modes is shown in the pie charts in the rightmost column.

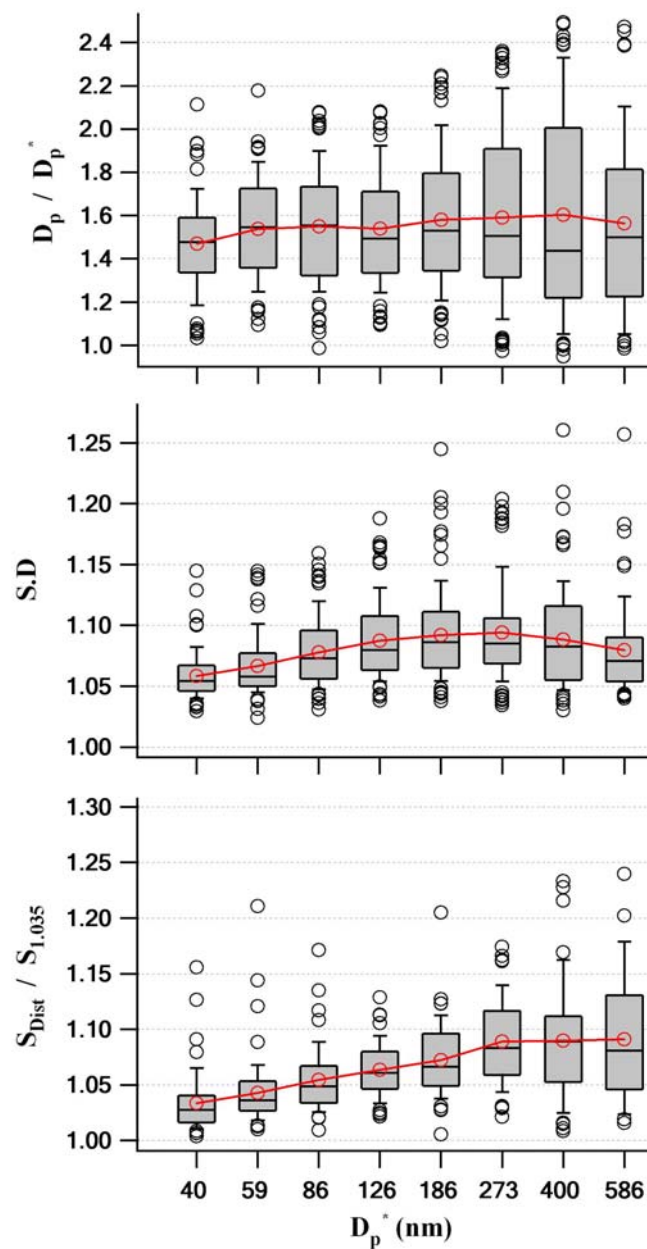


Figure 2.9. Box plots showing the median growth factor, dominant mode standard deviation, and S' parameter for all TDMA measurements made during the 12 flights considered here.

Despite differences between the aerosol observed on different flights, the trend of increasing compositional uniformity with decreasing particle size was consistently observed, as reflected Figure 2.10, which shows the size-dependence of S' for each of

the 12 flights considered. Lower count rates contribute to the increased variability observed for the larger particles considered, although the altitude-dependent abundance of more hygroscopic sulfate containing particles and less hygroscopic dust particles may be partly responsible. The pie charts in the third column of Figure 2.9 show the fraction of TDMA scans that were considered monomodal (1), bimodal (2) and those considered other (3). These classifications were based on the number of lognormals needed to represent each of the measured distributions. The hygroscopic growth factor distributions of both 40 and 59 nm particles were usually monomodal, whereas additional modes were frequently observed in the distributions for larger particles. Secondary modes are often apparent only as an asymmetry in the primary mode and did not result in more than one local maxima in the distribution. Because of this, simple peak detection algorithms would not be able to resolve many of the secondary modes. The size dependence of the categorization based on number of modes is shown more clearly in Figure 2.11. In general, the normalized standard deviation of a distribution will increase as the number of modes increases, which is reflected in the trends in both of these parameters shown in Figure 2.9.

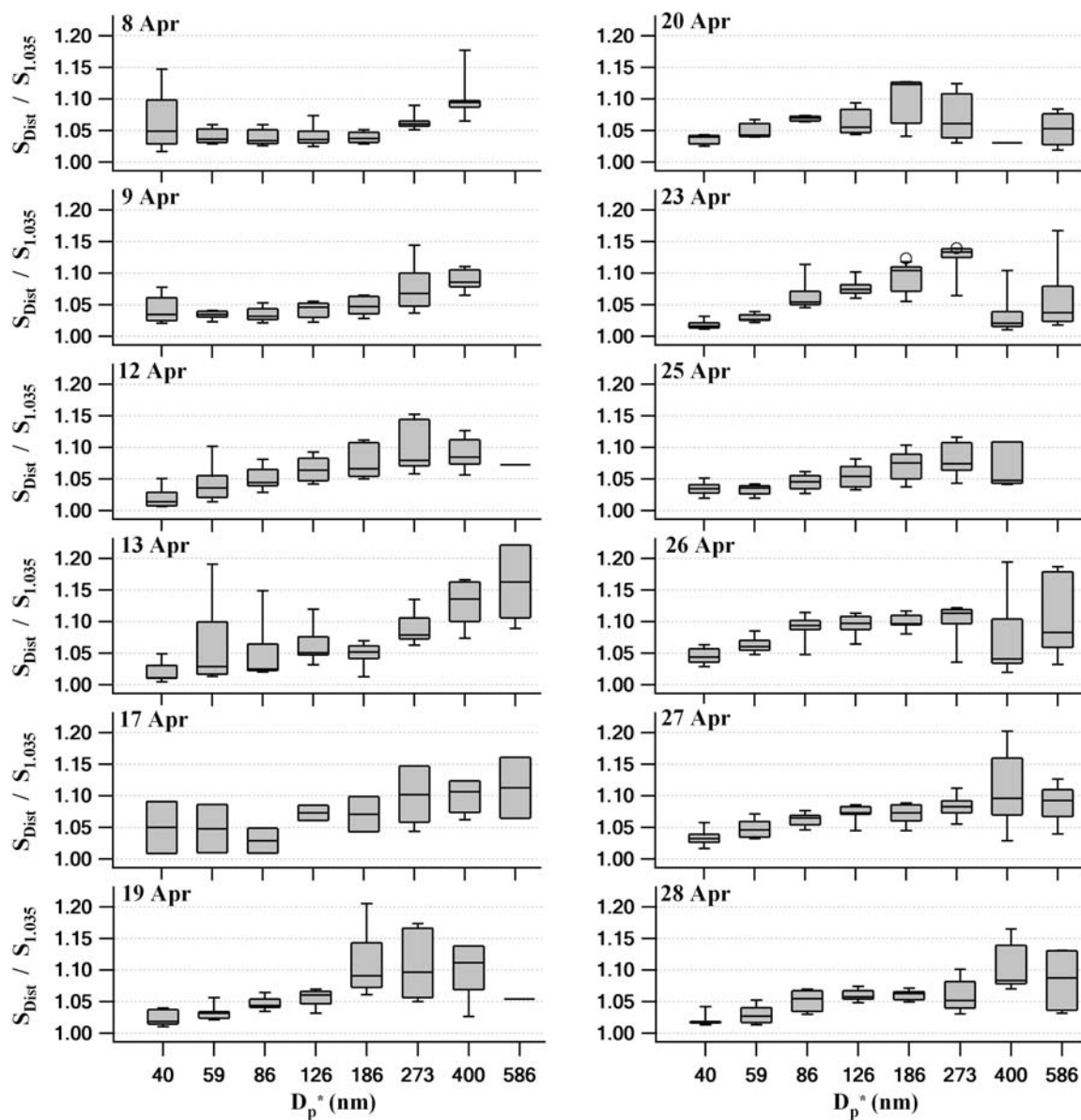


Figure 2.10. Box plots of S' at each diameter for all TDMA measurements analyzed.

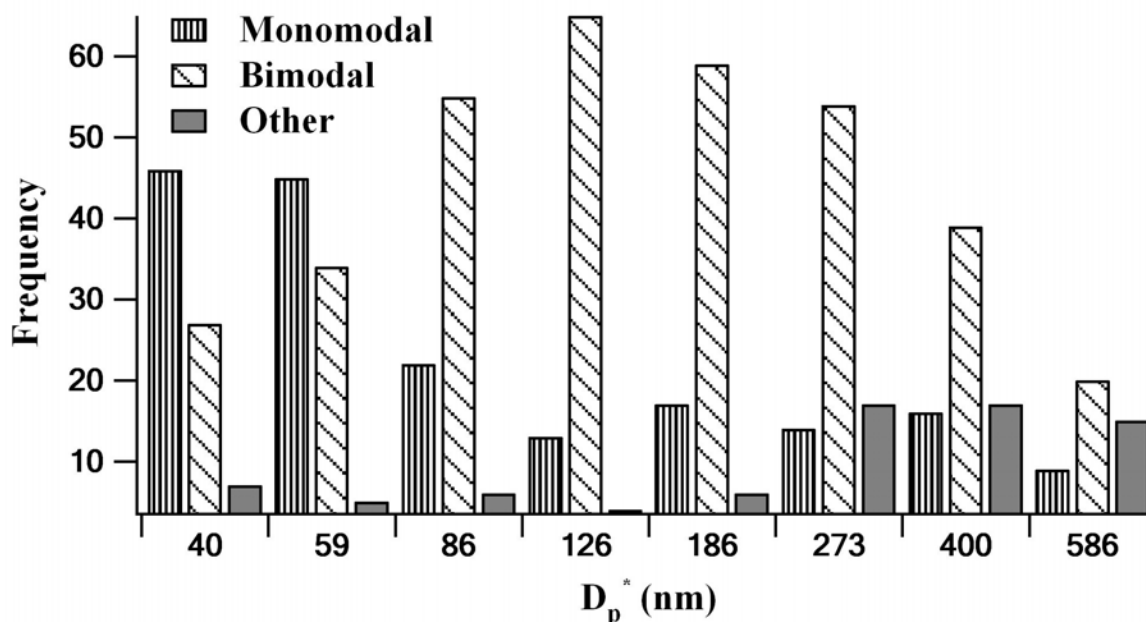


Figure 2.11. Frequency of identification of one, two, or more modes.

2.5.2 Variability in hygroscopic behavior with height

Consistent with measurements made in other regions, distinct aerosol layers were frequently observed during ACE-Asia. The source region, composition, and concentration of the aerosols within each layer often differ from those at other heights. In addition to variation in the properties of pollution aerosols, certain particle types are preferentially found at different heights. Both sea salt and dust aerosols usually have a mass median diameter greater than one micron, although the tails on the smaller particle side of their respective size distributions contributes to the concentration measured in the size range considered in this analysis. Hygroscopic sea salt particles are typically present only close to the surface, while non-hygroscopic dust particles are often found in layers in the free troposphere. Figure 2.12 contains box plots showing the growth factors and standard deviations segregated by measurement height. Consistent with

measurements of the humidity dependence of light scattering by *Gao et al.* [2003], the aerosol in the lowest layers was typically more hygroscopic than that at higher altitude. They explained this dependence by noting that aerosol samples in the well-mixed surface layer or just above it had similar fractions of anthropogenic, biomass, and dust components, but aerosols at high altitude had a larger fraction of dust species. This is supported by the observation here that the 400 nm particles were less hygroscopic than the 273 nm particles only in the uppermost level considered. Similar observations of the height dependence of sulfate and coarse aerosol mass are described in *Seinfeld et al.* [2004].

The rightmost column in Figure 2.12 shows the size and height dependence of the standard deviation of the dominant aerosol mode within the hygroscopic growth factor distributions. It is interesting to note that the standard deviations reached a maximum for intermediate particle sizes for measurements made between 100 and 1000 m, which was frequently the height at which pollution concentrations were greatest. Regardless of height, the dominant mode standard deviation of the 40 nm particles is always lower than any other size, suggesting that the smallest particles are the most compositionally uniform. The normalized standard deviations of the measured distributions as a function of height are shown in Figure 2.13. As expected, there is a strong correlation between the trends observed in this figure and those in the dominant mode standard deviations shown in Figure 2.12. The particle size for which the normalized standard deviations were greatest was typically shifted to slightly greater diameter than was observed for the standard deviation of the dominant mode. The

increased percentage of distributions containing more than one mode with increasing size is the cause of this slight shift. A statistical summary of the TDMA hygroscopic growth measurements as a function of height is presented in Tables 2.1 and 2.2.

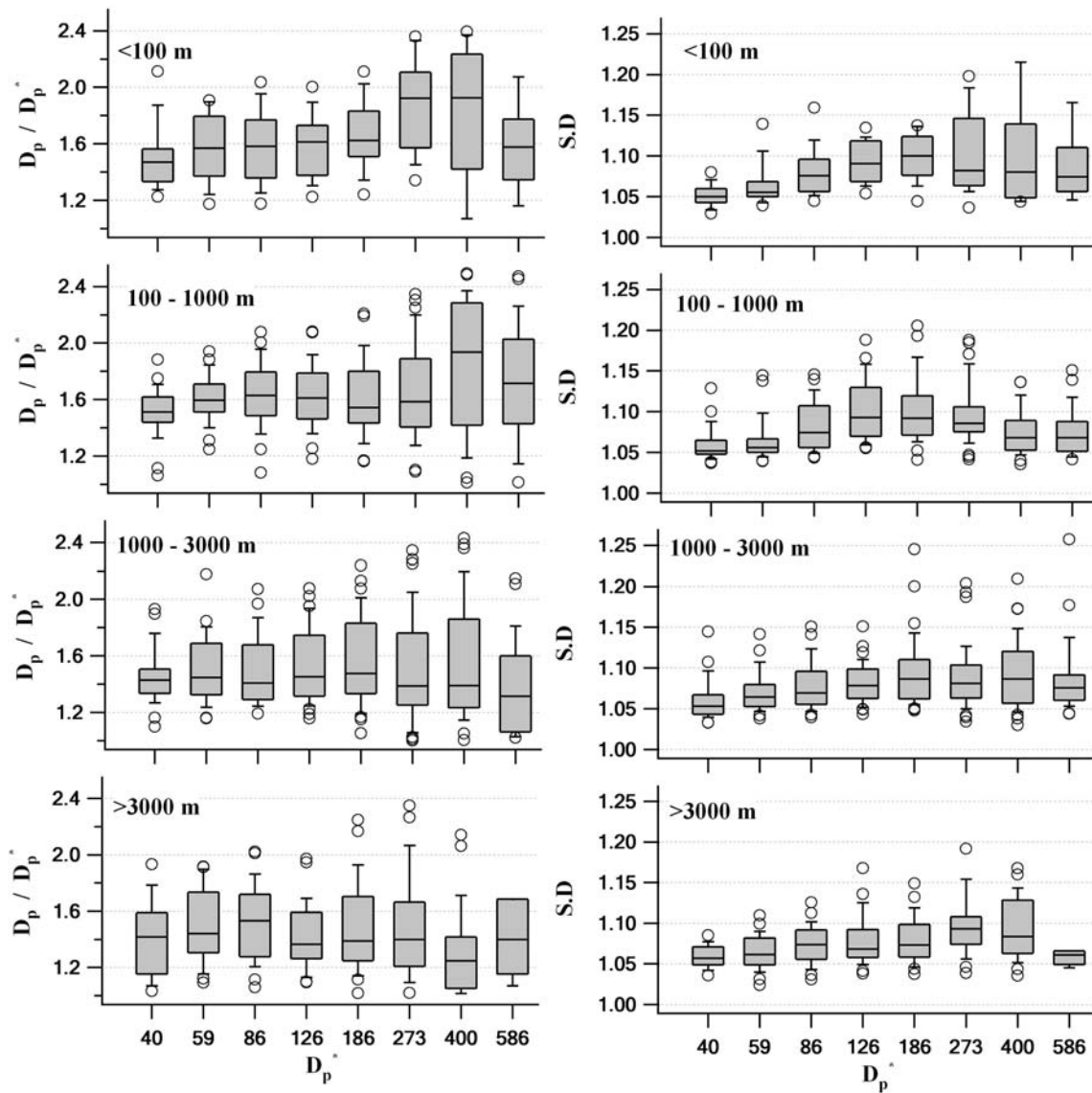


Figure 2.12. Box plots showing the median growth factor and standard deviation of TDMA measurements as a function of height.

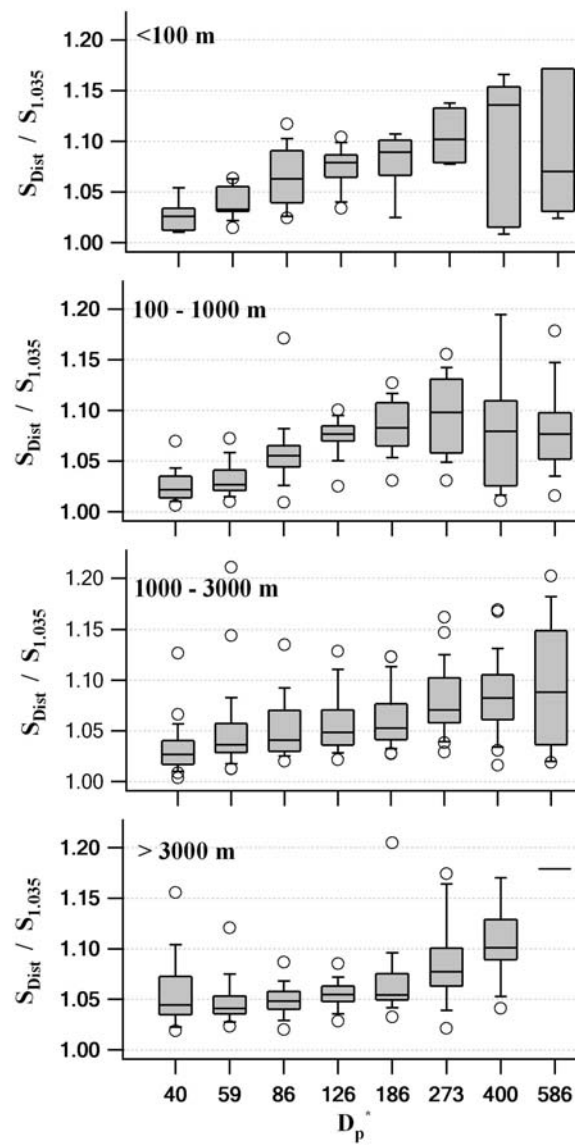


Figure 2.13. Box plots showing the size dependence of S' as a function of sampling height.

Table 2.1. Statistical summary of hygroscopic growth factors and dominant mode standard deviations.

G.F									S.D							
	T1	T2	T3	T4	T5	T6	T7	T8	T1	T2	T3	T4	T5	T6	T7	T8
<100 m																
AVG	1.50	1.57	1.58	1.58	1.67	1.88	1.82	1.58	1.05	1.07	1.08	1.09	1.10	1.11	1.11	1.09
S.D	0.24	0.24	0.26	0.22	0.25	0.33	0.48	0.34	0.01	0.03	0.03	0.03	0.03	0.05	0.07	0.05
MIN	1.23	1.18	1.18	1.23	1.24	1.34	0.98	1.12	1.03	1.04	1.04	1.05	1.04	1.04	1.04	1.04
MAX	2.11	1.91	2.04	2.00	2.11	2.36	2.40	2.25	1.08	1.14	1.16	1.13	1.14	1.20	1.26	1.18
No	14	19	22	20	18	15	13	10	14	19	22	20	18	15	13	10
100-1000 m																
AVG	1.52	1.60	1.63	1.63	1.63	1.65	1.83	1.71	1.06	1.06	1.08	1.10	1.10	1.10	1.07	1.07
S.D	0.16	0.16	0.22	0.22	0.27	0.34	0.48	0.41	0.02	0.02	0.03	0.04	0.04	0.03	0.03	0.03
MIN	1.06	1.25	1.08	1.18	1.16	0.97	1.01	0.99	1.04	1.04	1.04	1.06	1.04	1.04	1.04	1.04
MAX	1.88	1.94	2.08	2.08	2.21	2.35	2.49	2.47	1.13	1.14	1.15	1.19	1.21	1.19	1.14	1.15
No	40	33	43	42	45	57	36	45	40	33	43	42	45	57	36	45
1000-3000 m																
AVG	1.46	1.50	1.49	1.53	1.56	1.51	1.56	1.38	1.06	1.07	1.08	1.08	1.09	1.09	1.09	1.09
S.D	0.19	0.22	0.25	0.26	0.31	0.37	0.41	0.33	0.02	0.02	0.03	0.02	0.04	0.04	0.04	0.04
MIN	1.10	1.16	0.99	1.16	1.05	1.00	1.00	1.00	1.03	1.04	1.04	1.04	1.05	1.03	1.03	1.04
MAX	1.93	2.18	2.07	2.08	2.24	2.34	2.43	2.15	1.14	1.14	1.15	1.15	1.25	1.20	1.21	1.26
No	44	45	47	53	55	65	60	36	44	45	47	53	55	65	60	36
>3000 m																
AVG	1.41	1.51	1.51	1.43	1.49	1.49	1.30	1.42	1.06	1.06	1.07	1.08	1.08	1.10	1.09	1.06
S.D	0.26	0.27	0.26	0.23	0.31	0.38	0.30	0.35	0.01	0.02	0.02	0.03	0.03	0.04	0.04	0.01
MIN	1.03	1.09	1.06	1.09	1.02	1.02	0.95	1.07	1.04	1.02	1.03	1.04	1.04	1.04	1.04	1.05
MAX	1.93	1.92	2.02	1.97	2.25	2.35	2.14	1.78	1.09	1.11	1.11	1.17	1.15	1.27	1.17	1.07
No	27	31	40	41	38	37	31	4	27	31	40	41	38	37	31	4

G.F: Growth factor. S.D: Standard deviation. T1: 40 nm. T2: 59 nm. T3: 86 nm. T4: 126 nm. T5: 186 nm. T6: 273 nm. T7: 400 nm. T8: 586 nm. AVG: Average. MIN: Minimum. MAX: Maximum. No: Number of measurements.

Table 2.2. Statistical summary of the parameter S' .

	S'							
	T1	T2	T3	T4	T5	T6	T7	T8
<100 m								
AVG	1.03	1.04	1.06	1.07	1.08	1.11	1.10	1.10
S.D	0.02	0.02	0.03	0.02	0.03	0.03	0.08	0.10
MIN	1.01	1.01	1.02	1.03	1.01	1.08	1.01	1.02
MAX	1.07	1.06	1.12	1.10	1.11	1.14	1.17	1.24
No	9	11	12	10	9	6	5	4
100 - 1000 m								
AVG	1.03	1.03	1.06	1.07	1.08	1.10	1.08	1.08
S.D	0.02	0.02	0.03	0.02	0.03	0.04	0.07	0.04
MIN	1.01	1.01	1.01	1.03	1.03	1.03	1.01	1.02
MAX	1.07	1.07	1.17	1.10	1.13	1.16	1.23	1.18
No	26	23	22	22	24	27	19	20
1000 - 3000 m								
AVG	1.03	1.05	1.05	1.06	1.06	1.08	1.09	1.10
S.D	0.02	0.04	0.03	0.03	0.03	0.03	0.04	0.06
MIN	1.00	1.01	1.02	1.02	1.03	1.03	1.02	1.02
MAX	1.13	1.21	1.14	1.13	1.12	1.16	1.17	1.20
No	30	30	28	28	30	32	32	18
>3000 m								
AVG	1.06	1.05	1.05	1.05	1.07	1.09	1.11	1.18
S.D	0.04	0.02	0.02	0.01	0.04	0.04	0.05	0.00
MIN	1.02	1.02	1.02	1.03	1.03	1.02	1.04	1.18
MAX	1.16	1.12	1.09	1.09	1.20	1.17	1.23	1.18
No	13	19	21	21	19	19	14	1

2.6 Summary and conclusion

Measurements of size-resolved aerosol hygroscopicity were made using a tandem differential mobility analyzer system on board the Twin Otter aircraft during the ACE-Asia campaign from March 31 to May 1, 2001. Hygroscopic properties of 40, 59, 86, 126, 186, 273, 400, and 586 nm dry particle diameters were measured over time intervals of approximately 45 minutes. Hygroscopicity increased slightly with increasing particle size. Hygroscopic growth factors at 90% RH typically exceeded 1.4, suggesting the soluble fraction of the aerosol was relatively high. The absence of multiple distinct modes in most distributions suggests the aerosol approached an internal mixture. Despite the lack of multiple distinct modes, asymmetry in the measured growth factor distributions of larger particles measured indicates aerosol populations with similar, but not identical, composition were often present. The breadth of modes within growth factor distributions, and that of the entire distribution were used to quantify the compositional homogeneity of the aerosol. Mean standard deviations increased with increasing particle size, although this trend often reversed for the largest particles considered.

Overall, hygroscopicity was observed to increase with proximity to the surface, and with increasing size. One cause of the observed height dependence is the frequent presence of non-hygroscopic dust particles at higher levels that, closer to the surface, were either not observed or had been coated with soluble compounds such as sulfate.

CHAPTER III

IN SITU MEASUREMENTS OF ASIAN DUST AEROSOLS OFF THE CALIFORNIA COAST

Aerosol size distributions and hygroscopic growth were measured using a differential mobility analyzer (DMA) / Tandem DMA (TDMA) system on board a Twin Otter airplane off the coast of Monterey, California during the April, 2003 Asian Dust Above Monterey (ADAM-2003) experiment. The motivation for these measurements, and for the study overall, was to examine the transport of aged Asian dust reaching the coast of California. A distinct difference between the hygroscopic growth of the dust particles and other aerosol types present permitted isolation of a dust-only size distribution. In general, the relative contribution of dust particles to the overall size distribution varied from almost zero at the smallest particle size analyzed (200 nm), to almost 100% at the largest size analyzed (600 nm). Aerosol light scattering properties of the dust particles and other particle types present were predicted using the measured aerosol size distributions and hygroscopic properties. The study-average mass extinction efficiency at 550 nm of the dust aerosol was $1.72 \text{ m}^2/\text{g}$, while that of the non-dust aerosol was $2.37 \text{ m}^2/\text{g}$. The predicted scattering coefficients were also compared with directly measured scattering to test the accuracy of the measurements and the assumptions used to determine optical properties.

3.1 Introduction

A substantial amount of dust originating in productive source regions such as the Gobi and Saharan Deserts can be transported through the atmosphere over distances of thousands of kilometers. This dust can have significant direct and indirect impacts on the radiative balance of the atmosphere [IPCC, 2001]. Transport of Asian desert dust into and across the North Pacific region during spring has been the subject of a number of studies [e.g. Merrill *et al.*, 1989; Xiao *et al.*, 1997; Jaffe *et al.*, 1999; Jacob *et al.*, 1999; Husar *et al.*, 2001; McKendry *et al.*, 2001]. Husar *et al.* [2001] showed that Asian anthropogenic emissions significantly impact the concentrations of a large number of atmospheric species in the air reaching the United States. Jaffe *et al.* [1999] showed that the surface emissions from the Gobi were lifted into the free troposphere over Asia and then transported to North America in ~6 days. The Aerosol Characterization Experiment-Asia (ACE-Asia) provided a large number of observations of slightly aged Asian dust [Huebert *et al.*, 2003]. The arrival of the dust-laden air mass from NE Asia over western North America has been documented using aircraft observations [Price *et al.*, 2003]. That analysis describes a dust layer observed at approximately 4 km asl.

ADAM-2003 was an experiment designed to measure Asian dust that reached the west coast of North America. Its primary objective was to characterize the radiative and physical properties of aged Asian aerosols [ADAM-2003 Science plan, 2003]. ADAM-2003 took place from April 3-26, 2003 based out of the Monterey, California. The first ADAM research flight was conducted on 18 April 2003 and the seventh and final flight

was on 26 April. Observed dust loadings during the study period were typical for early spring.

3.2 Aircraft operations

Both forecast models and satellite observations were used to identify the optimal flight times and flight tracks. Typical flight patterns would include an initial vertical profile over the study site to locate and characterize any dust layers present using fast response nephelometers and optical particle counters. After completing the profile, the aircraft would typically fly level legs below, in, and above each of the identified dust layers. Flight tracks from three of the flight days are shown in Figure 3.1. On 20 April, the aircraft remained in the vicinity of Monterey, CA. To satisfy one of the objectives of the flight, several legs were flown over the Mobile Atmospheric Aerosol and Radiation Characterization Observatory (MAARCO). The following day, the Twin Otter climbed to 3.5km and ferried to off the coast of Santa Barbara to intercept a forecast dust plume. During the flight on 22 April, the aircraft sampled along much of the central coast of California between Monterey and San Francisco. Table 3.1 provides a summary of the flight level information for the Twin Otter during ADAM.

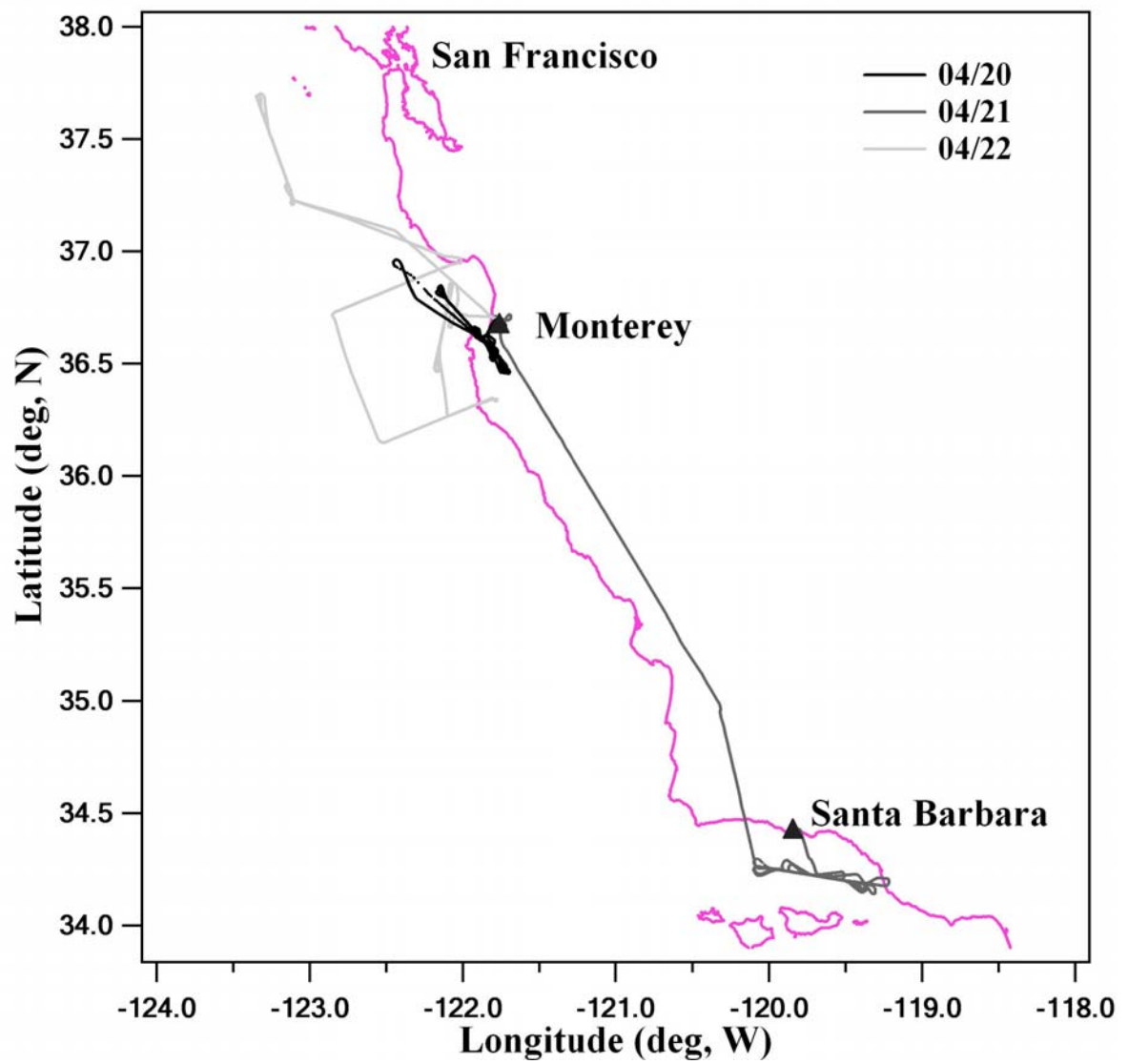


Figure 3.1. Flight tracks of the Twin Otter for flights conducted on 20, 21, and 22 April 2003.

Table 3.1. Summary of flight level information for the Twin Otter during ADAM.

Date		Data Collection Period, UTC	Altitude, m
04/20	L1	21:10:39 – 21:45:05	3710
04/21A	L1	18:42:19 – 18:57:50	2830
04/21A	L2	19:21:04 – 19:41:43	2520
04/22	L1	22:03:18 – 22:26:32	2660
04/22	L2	22:38:34 – 22:57:28	3250
04/22	L3	23:01:48 – 00:22:40	2950

Figure 3.2 shows vertical profiles of the scattering coefficient at a wavelength of 550 nm measured using a nephelometer during five flights on four study days. The shaded layers represent the approximate altitude ranges in which significant dust concentrations were observed. Most layers were observed at altitudes between 2.2 and 4.6 km. Since several discrete layers often existed, multiple horizontal flight legs (horizontal gray lines) were chosen to investigate the aerosol characteristics within the layers. There are three days for which measurements were made during horizontal legs inside the dust layers. The analysis here will focus on the data collected on those days. Specifically, the measurements analyzed were collected on 20, 21, and 22 April at roughly 3.7 km, 2.8 km, and 3.0 km, respectively.

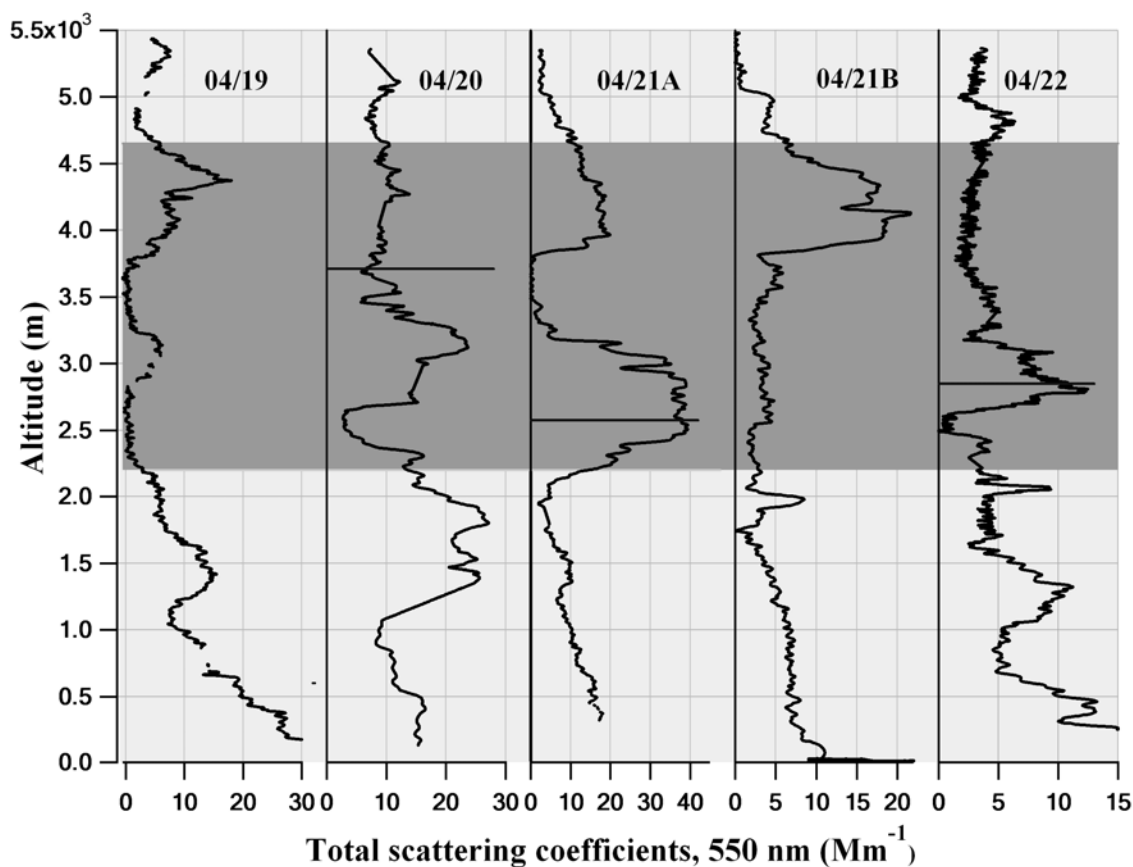


Figure 3.2. All vertical profiles of the scattering coefficient (550 nm) measured with a nephelometer. The altitude range over which dust was observed is shaded and the flight legs aimed at characterizing those layers are shown as horizontal lines.

Backward trajectories terminating at the sampling heights and locations for three flight days were computed using NOAA HYSPLIT model [Draxler and Rolph, 2003]. These trajectories are shown in Figures 3.3 – 3.5. Although the accuracy of such long trajectories is questionable, each of those shown does indicate that the air may have originated over the Gobi Desert region several days prior to reaching California. These trajectories also emphasize the proximity of the major industrial regions in Asia to the predicted path taken by the dust. These anthropogenic emissions may alter the properties of the dust particles by coating the surfaces with soluble components. This

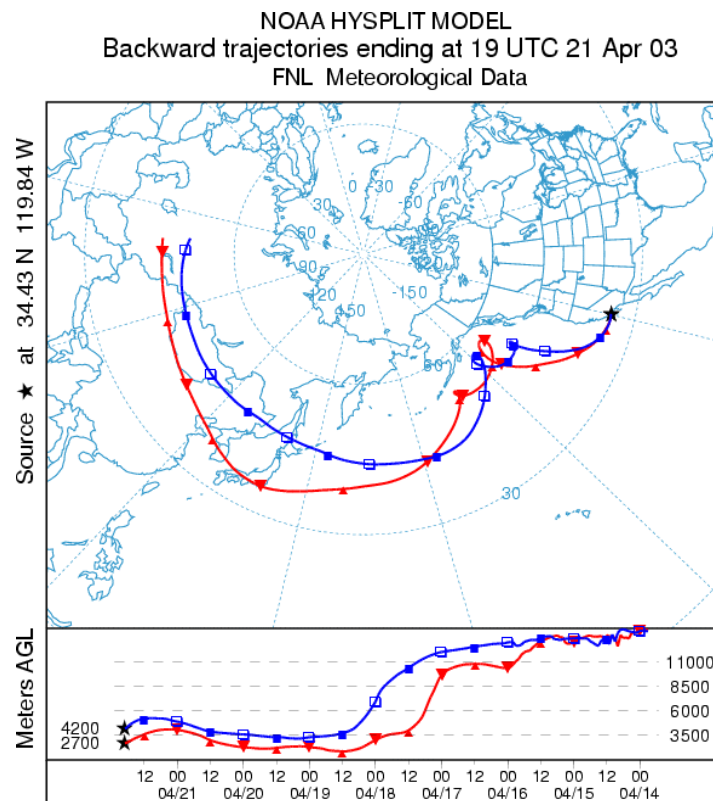


Figure 3.4. Eight-day backward trajectories computed using the NOAA HYSPLIT model. The trajectories terminate at the positions and altitudes of the aircraft during constant level flight legs on 21 April, 2003.

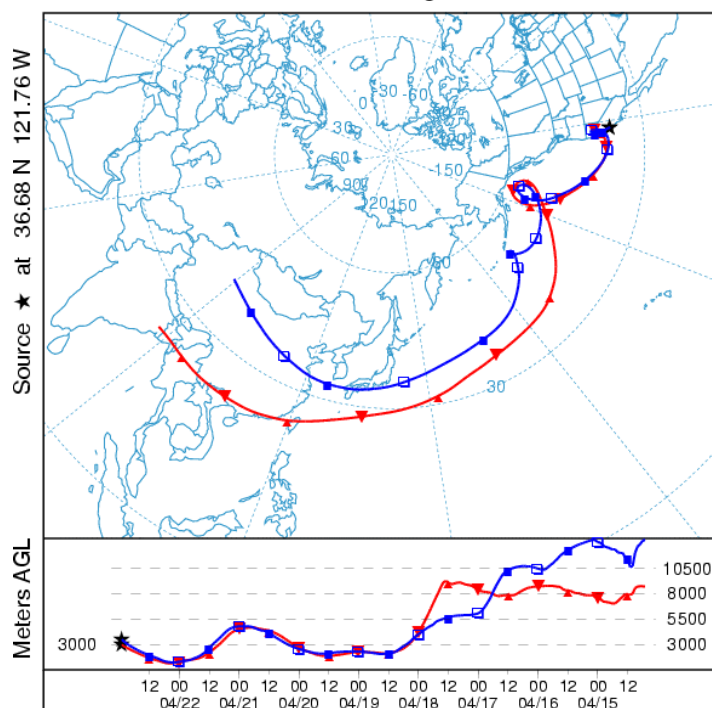


Figure 3.5. Eight-day backward trajectories computed using the NOAA HYSPLIT model. The trajectories terminate at the positions and altitudes of the aircraft during constant level flight legs on 22 April, 2003.

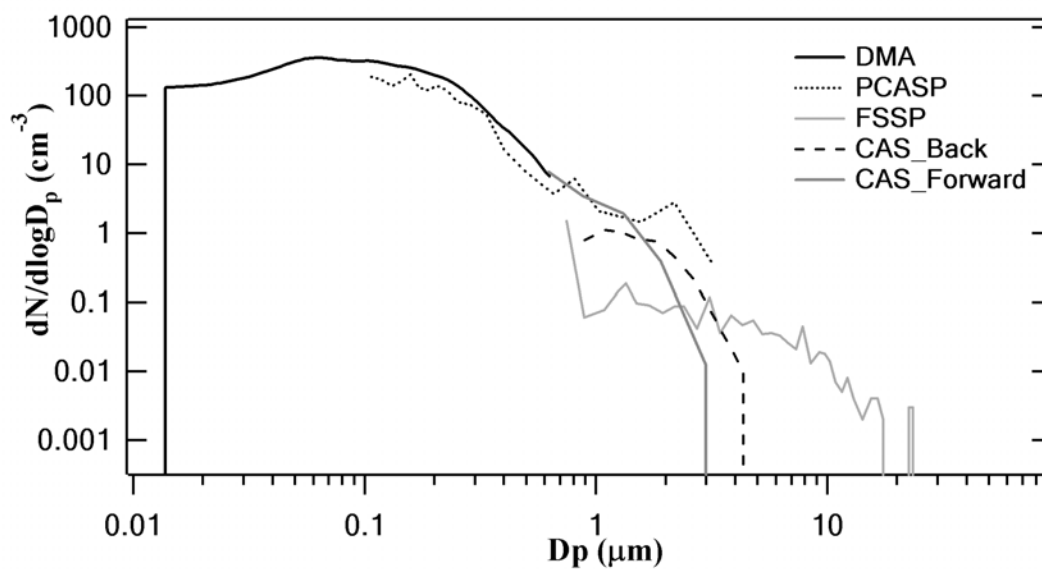
3.3.1 Instruments

Several instruments were operated on board the Twin Otter during ADAM-2003. Aerosol and cloud droplet size distributions were measured using a combination of three optical particle counters (OPCs), a differential mobility analyzer (DMA), and an aerodynamic particle sizer (APS, TSI Inc., Minnesota). The optical particle counters included a passive cavity aerosol spectrometer probe (PCASP-100X, Particle Measurement Systems, Inc, DMT Electronics) that characterized particles between 0.1

and 3 μm , a forward scattering spectrometer probe (FSSP-100, Particle Measurement Systems, Inc, DMT Electronics) that measured aerosol size from 0.75 to 18 μm , and a cloud and aerosol spectrometer that characterized particle size between about 0.3 and 50 μm through simultaneous measurements of forward and backward scattering intensity (CAS_Forward and CAS_Backward, DMT, Inc.). Size-resolved hygroscopic growth was measured using a tandem differential mobility analyzer. The optical properties of the aerosol were measured directly using a nephelometer, a sun tracking sunphotometer, and a number of radiometers. Examples of the size and volume distributions measured by all instruments except the APS on 22 April 2003 are presented in Figures 3.6 and 3.7. Over the entire study period, concentrations measured by the FSSP were consistently about 30% lower than those measured by the PCASP in the overlapping size range. The size distributions measured by the DMA and CAS_Forward appeared to approach the same value in the gap between the two distributions. Although the observed consistency may not necessarily guarantee accuracy, the size distributions used in the analysis that follows were constructed by combining the DMA and CAS_Forward data. The instruments operated on board the Twin Otter during ADAM-2003 are listed in Table 3.2.

Table 3.2. Instrumentation operated on board the Twin Otter during ADAM-2003.

Instrument	Manufacturer	Measurement
PCASP-100X	PMS, Inc, DMT Electronics	Aerosol size distribution
FSSP-100	PMS, Inc, DMT Electronics	Aerosol size distribution
CAS	DMT, Inc.	Particle size distribution
DMA	Aerosol Dynamics, Inc.	Particle size distribution
TDMA	Aerosol Dynamics, Inc.	Hygroscopic growth
APS	TSI Inc., Minnesota	Particle size distribution
Nephelometer-3 color (Model 3563)	TSI Inc., Minnesota	Scattering / Backscattering coefficient

**Figure 3.6.** Example of airborne size distribution measurements on 22 April 2003.

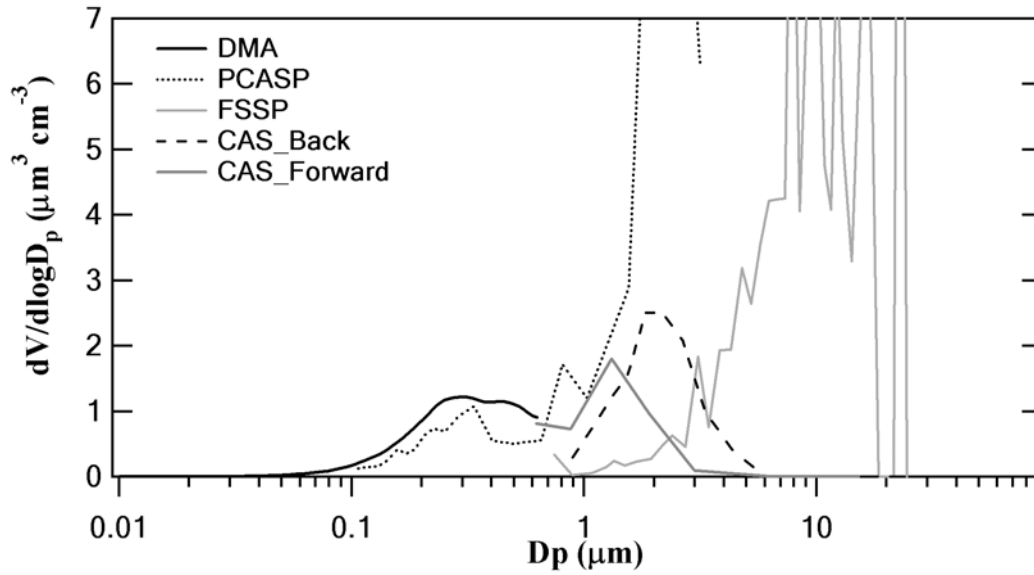


Figure 3.7. Example of airborne volume distribution measurements on 22 April 2003.

3.3.2 Lognormal fitting

Lognormal fits were used to describe the measured hygroscopic growth factor distributions and the integrated dust and non-dust size distributions described below. Once the hygroscopic growth factor distributions were fitted, size-resolved segregation into the dust and other aerosol categories was usually straightforward due to the distinct hygroscopic properties of the two particle types. The lognormal distribution often accurately represents aerosol size distributions and is regularly used in atmospheric applications [Seinfeld and Pandis, 1998]. The lognormal distribution is given by

$$\frac{dN}{d \log D_p} = \frac{N}{\sqrt{2\pi} \cdot \log(\sigma_g)} \exp \left[-\frac{(\log D_p - \log D_{pg})^2}{2 \cdot (\log \sigma_g)^2} \right], \quad (3.1)$$

where N is the total aerosol number concentration, D_p is the aerosol diameter, D_{pg} is the geometric mean diameter, and σ_g is the geometric standard deviation. The fractional

contribution of dust at 200, 400, and 600 nm was determined from the fitted hygroscopic growth factor distributions. The product of this fractional contribution and the overall size distribution gives the size distribution of the dust. The fractional contribution was extrapolated or interpolated for each bin of the measured size distribution. This extrapolation is not believed to introduce significant error since the fractional contribution typically approached zero at 200 nm and 1.0 at 600 nm.

3.4 Results and discussions

3.4.1 Hygroscopicity

Measured hygroscopicity is typically quantified by the growth factor (GF), which is simply the ratio of the diameter of a particle following exposure to high RH (D_p) to its initial, or dry, diameter at low RH, D_p^* . A description of the TDMA system used to characterize size-resolved hygroscopicity is provided in *Gasparini et al.* [2004]. A short discussion of the application of these measurements to dust characterization is provided here. Freshly generated dust particles exhibit little hygroscopic growth, whereas other common aerosol types found in marine regions such as sulfates grow in response to increased relative humidity (RH). A simplistic depiction of the growth factor distributions expected for a range of common aerosol types is shown in Figure 3.8. Almost all hygroscopic growth factor distributions for the 400 and 600 nm particles, and some of those for the 200 nm particles possessed a mode centered at a growth factor near 1.0. This mode was assumed to consist only of dust particles. Most of the distributions also possessed a mode centered at a growth factor consistent with an aerosol composed

primarily of sulfate. A third mode was also identified in some of the distributions that had a median growth factor intermediate of the dust and sulfate modes. Although the exact composition of these particles is unknown, it was assumed that they were not composed of dust. Examples of growth factor distributions for the three sizes analyzed during this study are shown in Figure 3.9. The shaded regions represent the lognormals used to fit each of the distributions. The fractional contribution of each of the modes is used to partition the aerosol size distribution into a dust-only and non-dust distribution. Averaged over the entire study, the median growth factors of the 2 or 3 modes were 1.27 and 1.47 at 200 nm, 1.04, 1.31 and 1.53 at 400 nm, and 1.06 and 1.44 at 600 nm.

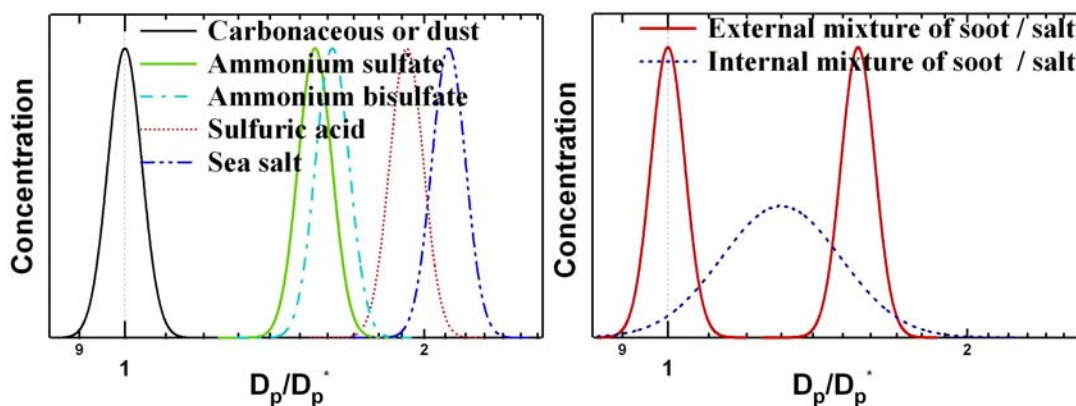


Figure 3.8. Simplistic representation of the behavior of distinct aerosol types as measured by a TDMA.

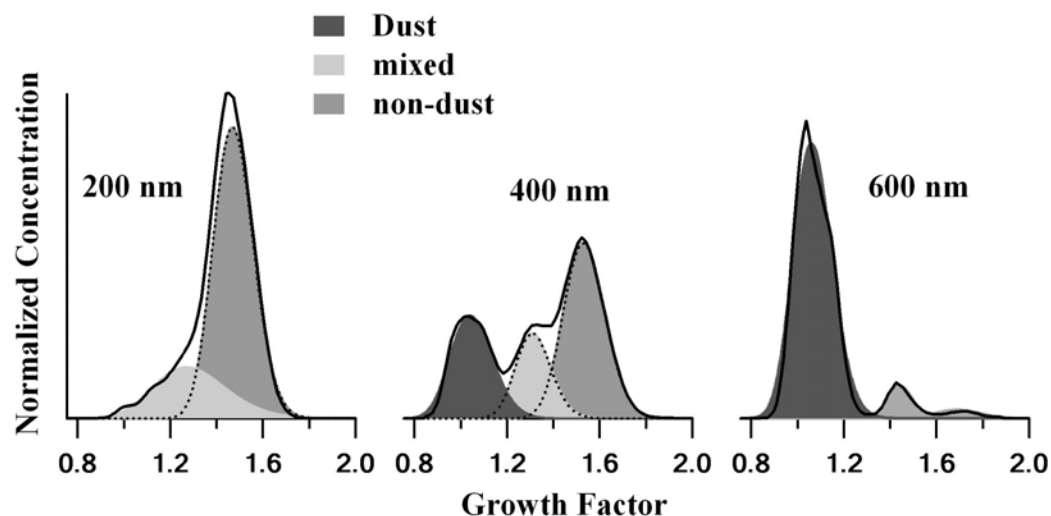


Figure 3.9. An example of lognormal fitting of the aerosol particle hygroscopic growth factor distributions measured on 22 April 2003. Each lognormal is shaded based on the inferred composition of the aerosol within the mode it represents.

3.4.2 Integration of size distributions and lognormal fittings

For each of the averaging periods, we created a single size distribution by combining the measurements made using the DMA and the CAS_Foward. The DMA measured particles having diameters between 15 nm and 650 nm, while the CAS_Foward covered particles between 850 nm to 13 μm . The size-resolved concentration for particles between the two size ranges was linearly interpolated. The product of this overall size distribution and the size-resolved dust fraction determined from the hygroscopicity measurements describes the dust-only size distribution. The difference between the total and dust-only size distribution is referred to as the non-dust distribution. Dust-only volume concentration distributions created from each of the measurements were fit using lognormals in a manner similar to that described above.

The following expression relates the parameters describing each of these lognormals to the corresponding size-resolved volume concentration.

$$\frac{dV}{d \log D_p} = \frac{\pi D_p^3 N}{6\sqrt{2\pi} \cdot \log(\sigma_g)} \exp \left[-\frac{(\log D_p - \log D_{pg})^2}{2 \cdot (\log \sigma_g)^2} \right]. \quad (3.2)$$

An example showing measured size distributions and the lognormals used to represent the combined distribution is presented in Figure 3.10. Table 3.3 summarizes the lognormal fits for the dust size distributions measured during each of the flights.

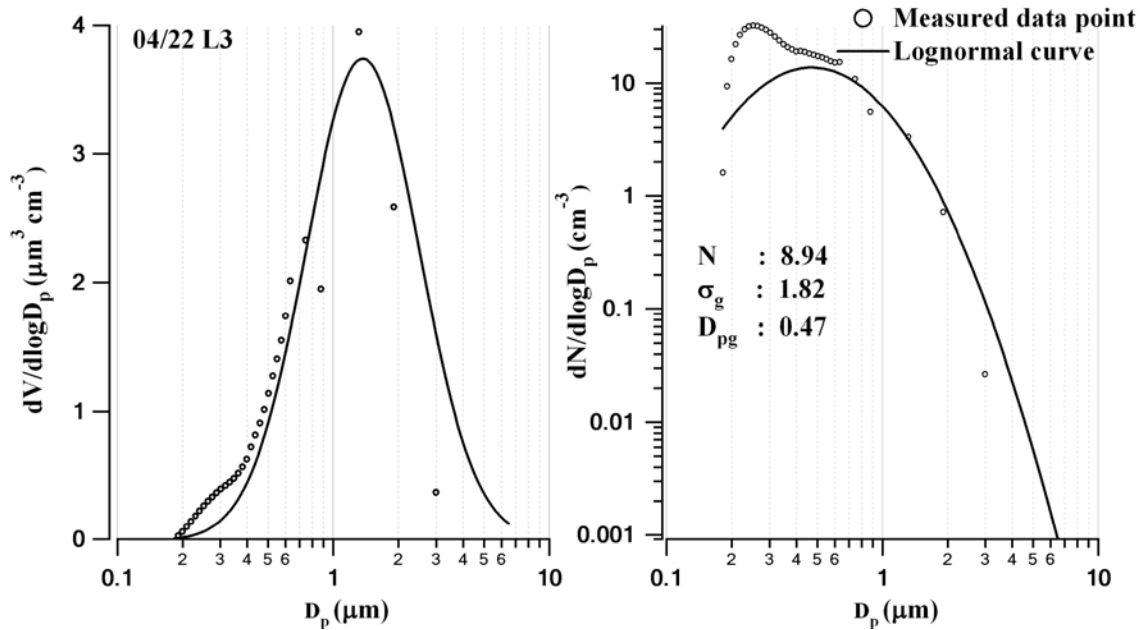


Figure 3.10. An example of a dust aerosol volume size distribution (left) and number size distribution (right) measured on 22 April 2003 (L3). Circles are measured data and solid lines are lognormal fits.

Table 3.3. Parameters prescribing dust lognormals.

Parameters				
Date		$N(cm^{-3})$	σ_g	$D_{pg}(\mu m)$
04/20	L1	5.72	1.729	0.610
04/21A	L1	45.80	2.037	0.282
04/21A	L2	15.40	1.820	0.449
04/22	L1	9.3	1.824	0.472
04/22	L2	3.22	1.702	0.599
04/22	L3	8.94	1.820	0.470
Average		14.73	1.822	0.480

3.4.3 Optical properties

The extinction and scattering coefficient of an aerosol is related to its size distribution and size-resolved composition through

$$\sigma_{ext} = \sum_{i=1}^2 \int_{D_{p1}}^{D_{p2}} \frac{\pi}{4} D_p^2 Q_{ext}(m, \alpha, i) \frac{dN_i}{d \log D_p} d \log D_p, \quad (3.3)$$

where i represents the dust and non-dust components, D_p is the particle geometric mean diameter over which the integral is performed, D_{p1} and D_{p2} are the minimum and maximum geometric mean diameters, respectively, $Q_{ext}(m, \alpha, i)$ is the particle extinction efficiency, m is the complex refractive index, $\alpha = \pi D_p / \lambda$ is the size parameter, with wavelength λ , and $dN/d \log D_p$ is the size distribution function of species i measured with the DMA and CAS_Forward. The scattering coefficient is calculated in the same way by replacing $Q_{ext}(m, \alpha, i)$ with $Q_{scat}(m, \alpha, i)$. An analogous expression exists for the backscattering coefficient, σ_{bsp} , with the index for the efficiency being $Q_{bsp}(m, \alpha, i)$.

The TSI nephelometer measures the total scattering and hemispheric backscattering coefficient at 3-wavelengths for scattering angles between 7° and 170°, and between 90° and 170°, respectively. *Anderson et al.* [1996] reported the truncation of near forward and near backward scattered light for the TSI 3563. The resulting angular sensitivity is used to determine the expected scattering intensity as measured by a nephelometer,

$$\sigma_{sca, neph} = \sum_{i=1}^2 \int_{D_{p1}}^{D_{p2}} \frac{\pi}{4} D_p^2 Q_{sim}(m, \alpha, i, f(\Theta)) \frac{dN_i}{d \log D_p} d \log D_p, \quad (3.4)$$

where Q_{sim} is the expected scattering efficiency for a nephelometer with angular sensitivity, $f(\Theta)$ [*Anderson et al.*, 1996]. The hemispheric backscattering coefficient, $\sigma_{bsp, neph}$, was calculated in the same way. The calculated scattering and hemispheric backscattering coefficients based on the measured size distributions were compared with the direct measurements made with the TSI nephelometer for 450, 550, and 700 nm wavelengths. Assumed refractive indices of $n = 1.473 - 0.001i$ and $n = 1.53 - 0.001i$ for non-dust and dust, respectively were used in the calculations. The non-dust refractive index selected is that of ammonium bisulfate, which is approximately half way between ammonium sulfate (1.53) and sulfuric acid (1.42). Although no composition measurements were available to support this assumption, the impact on overall optical properties is relatively small.

Mass distributions for the non-dust and dust aerosol were also calculated by integrating each of the volume distributions and multiplying by assumed densities of 1.78 and 2.5 g/cm³, respectively. Mineral dust density has been shown to vary with source region. For example, a density of 2.7 g/cm³ was found to be appropriate for dust

particles from Africa [Reid *et al.*, 2003], while a lower density of 2.0 g/cm^3 was derived for dust observed during the PRIDE campaign [Maring *et al.*, 2003]. The extinction and mass distributions presented below are shown as stacked plots to clearly identify the contributions of the dust and non-dust aerosol.

3.4.4 Case studies

3.4.4.1 20 April

As described above, most flights began with a vertical profile to identify the altitude ranges over which dust was present. The data collected during this initial vertical profile are shown in Figure 3.11b. Unfortunately, the flight levels selected based on this profile were slightly above the layer at approximately 3200 m that had the highest dust concentration. As a result, the dust concentrations observed were somewhat lower than during other flights. As shown in Figure 3.11A, the measured scattering coefficient was relatively constant throughout much of the flight. The average scattering coefficient at 550 nm of 8.7 Mm^{-1} was substantially less than the 23 to 181 Mm^{-1} observed closer to the source region during ACE-Asia [Carrico *et al.*, 2003]. Figure 3.11c shows the growth factor distributions for 200, 400, and 600 nm measured during the nearly constant altitude flight legs. The dark shaded mode in these distributions is believed to be made up of dust particles, while the lighter shaded modes are made up of other aerosol types. The increasing fractional contribution of the dust aerosol with increasing size is consistent with the expectation that the overall dust size distribution has a supermicron mass median diameter.

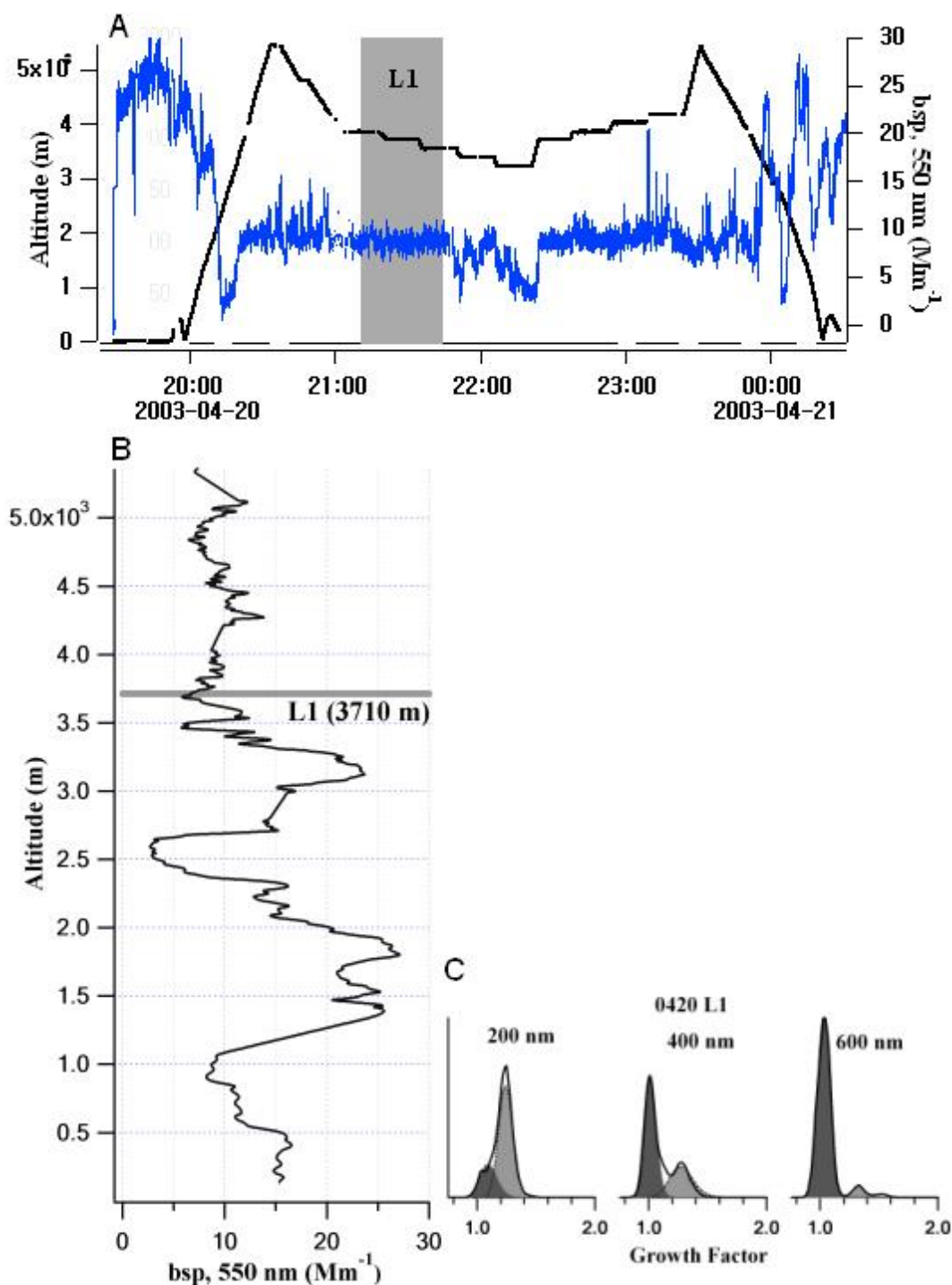


Figure 3.11. (A) Flight altitude and corresponding scattering coefficient at 550 nm for the flight on 20 April. The shaded box represents the segment used in this analysis. (B) Vertical profile of the scattering coefficient (550 nm) measured with the nephelometer (C) Growth factor distributions for 200, 400, and 600 nm particles. The dust distribution is shaded dark gray.

The size-dependent fractional contribution of dust particles is shown in the top graph in Figure 3.12. For this flight, the dust fractions obtained from the lognormal fits of the growth factor distributions were 0.291, 0.717, and 0.953 for 200, 400, and 600 nm diameter particles, respectively. As with the other cases to be described below, the 600 nm particles were categorized as almost pure dust. Therefore, extrapolation of the trend shown in Figure 3.12 for particles larger than 600 nm is not believed to introduce significant error. Although large sea salt particles are present in the marine atmosphere, their concentration in the free troposphere at the altitudes probed during this study is thought to be significantly lower than that of dust. Even in layers such as this that were chosen due to the high concentration of dust, the number size distribution shown in Figure 3.12 indicates that other aerosol types were present at substantially higher number concentration than the dust. In contrast, the mass distribution of the aerosol is dominated by the coarse dust mode as is also shown in Figure 3.12. The overall mass fraction of the dust, defined as $\frac{m_d}{m_d + m_{nd}}$, where m_d is the total mass concentration of dust and m_{nd} is the total mass concentration of the remaining aerosol, varied in this study between 68 % to 93 %.

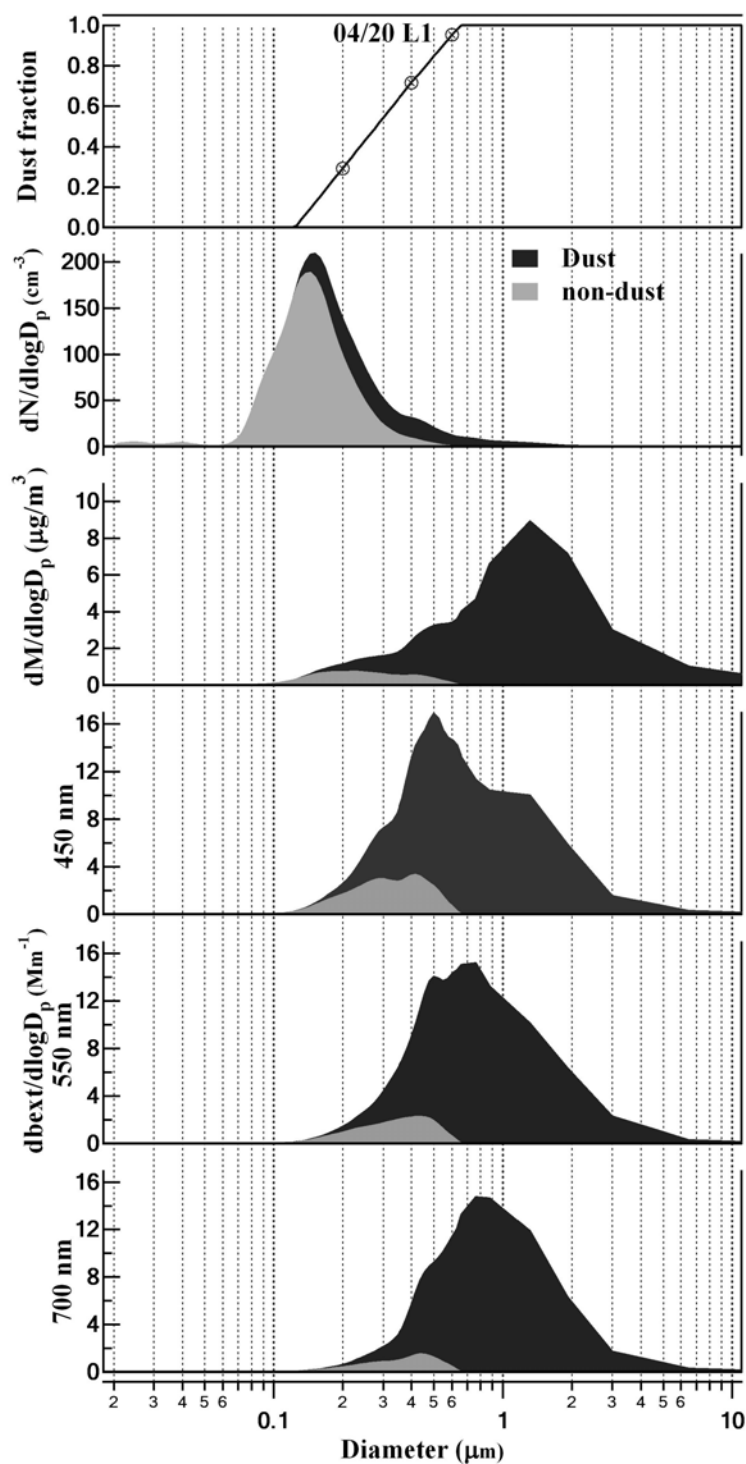


Figure 3.12. Size-dependent dust fraction and number, mass, and extinction coefficient distributions for 450, 550, and 700 nm determined for the aerosol sampled on 20 April. The contribution of the dust aerosol is shaded black and that of the remaining aerosol is shaded gray.

The partitioned size distribution and the refractive indices identified above were used to create the extinction distributions for 450, 550, and 700 nm shown in Figure 3.12. The peak in these distributions lies between the extremes of the number and mass distributions. The decreased significance of the coarse mode aerosol is the result of the decreased mass extinction efficiency of these particles that are within or approaching the geometric scattering range for the wavelengths considered here [Bergin *et al.*, 2001]. The modal diameters of the extinction distributions for 450, 550, and 700 nm were 0.5, 0.7, and 0.8 μm , respectively. Analogous to the ratio described for the aerosol mass concentration, the extinction fraction of the dust is defined as $\frac{E_d}{E_d + E_{nd}}$, where E_d is the extinction caused by the dust aerosol and E_{nd} is the extinction caused by the remaining aerosol. For this flight, dust contributed 86.3 %, 90.3 %, and 94.1% to the total extinction coefficients for blue, green, and red light, respectively.

3.4.4.2 21 April

A pronounced dust layer was observed at roughly 2500 m asl on 21 April. Unlike the flight on 20 April, the level flight legs chosen based on the initial vertical profile were near the altitude of maximum dust concentration. Data collected during the two flight legs identified in Figure 3.13a were analyzed. The average scattering coefficients within these two layers were 24.8 and 22.0 Mm^{-1} , respectively. These were the highest values observed during level flight during any of the ADAM-2003 missions. The hygroscopic growth factor distribution for 200 nm particles did not possess a distinct mode centered at a growth factor of about 1.0 as was observed during the flight on 20 April. While it is possible that the less hygroscopic mode is composed of dust that has been coated with soluble compounds, it was assumed in this analysis that the dust fraction at 200 nm was zero. The increased number concentration on this day may have obscured the more dilute dust aerosol in the growth factor distribution.

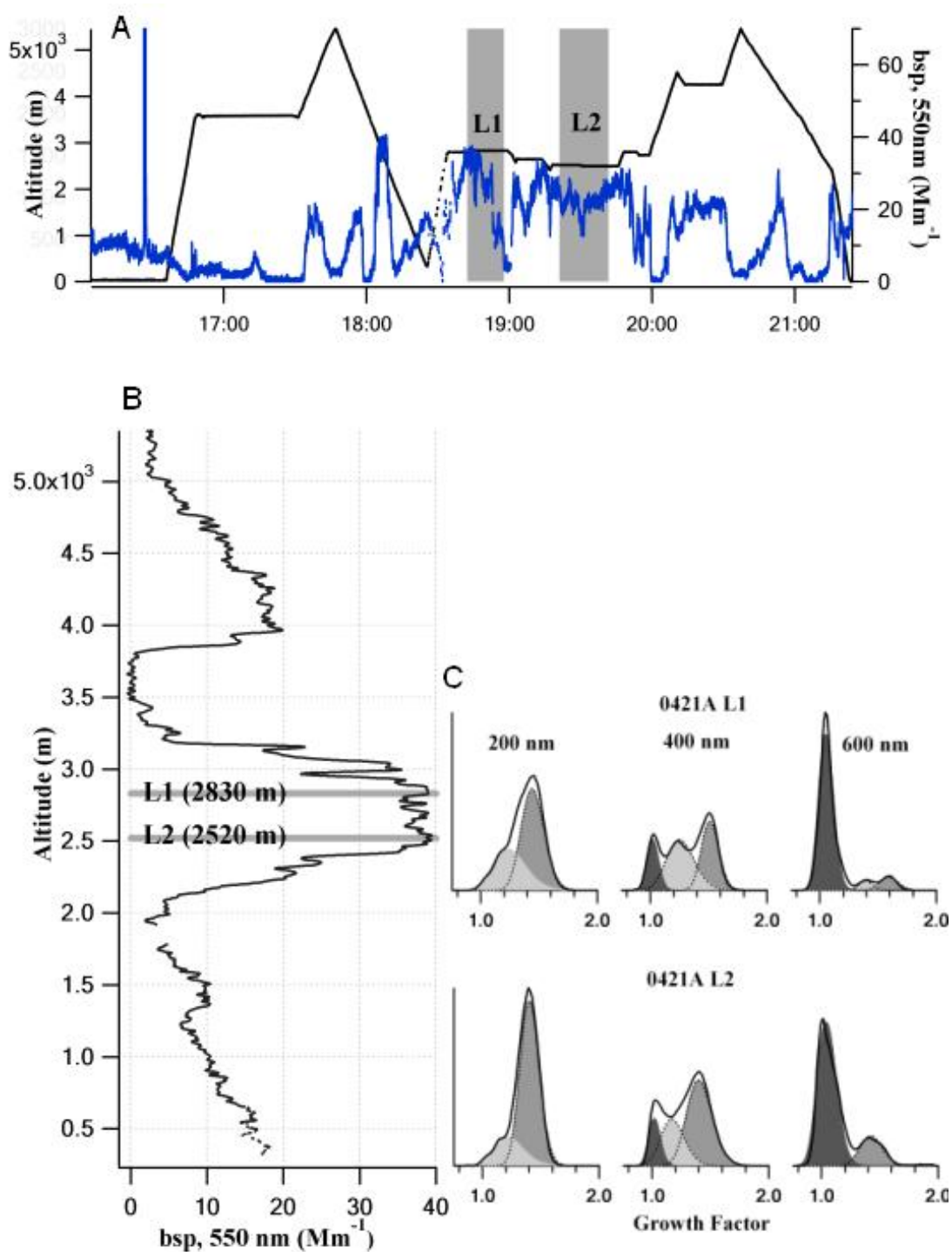


Figure 3.13. (A) Flight altitude and corresponding scattering coefficient at 550 nm for the flight on 21 April. The shaded boxes labeled L1 and L2 represents the segments used in this analysis. (B) Vertical profile of the scattering coefficient (550 nm) measured with the nephelometer (C) Growth factor distributions for 200, 400, and 600 nm particles. The dust distribution is shaded dark gray.

Separate size distributions for the dust and non-dust aerosol were created for the two flight legs identified in Figure 3.13. These distributions and the size-dependent dust fractions used to create them are shown in Figures 3.14 and 3.15. As discussed above, the absence of a clear dust mode in the growth factor distributions of 200 nm particles led to the interpretation that the dust concentration at that size was zero. Similar to the data collected on 20 April, the growth factor distributions for 600 nm particles indicate that the fractional contribution of dust approaches 1.0 in the submicron size range. The number size distributions shown in Figures 3.14 and 3.15 suggest an even smaller contribution from dust particles than that observed on 20 April. Dust also contributes less to the mass distributions than it did on 20 April, although it still dominates the overall mass concentration. The mass size distribution of the dust aerosol appears to have a shape similar to that on 20 April, while the increased contribution by other aerosol types causes the overall mass distribution to appear somewhat bimodal. The increased concentration of other aerosol types also reduced the fractional contribution of the dust aerosol to the overall extinction coefficients. The mode diameters of the extinction distributions shifted towards smaller size relative to those on 20 April. Specifically, the average mode diameters of the extinction distributions measured during the two flight legs were approximately 0.4, 0.5, and 0.7 μm for blue, green, and red light, respectively. The average fractional contribution of dust to the overall extinction coefficients on this day were 50.4%, 60.8%, and 72.5%, respectively.

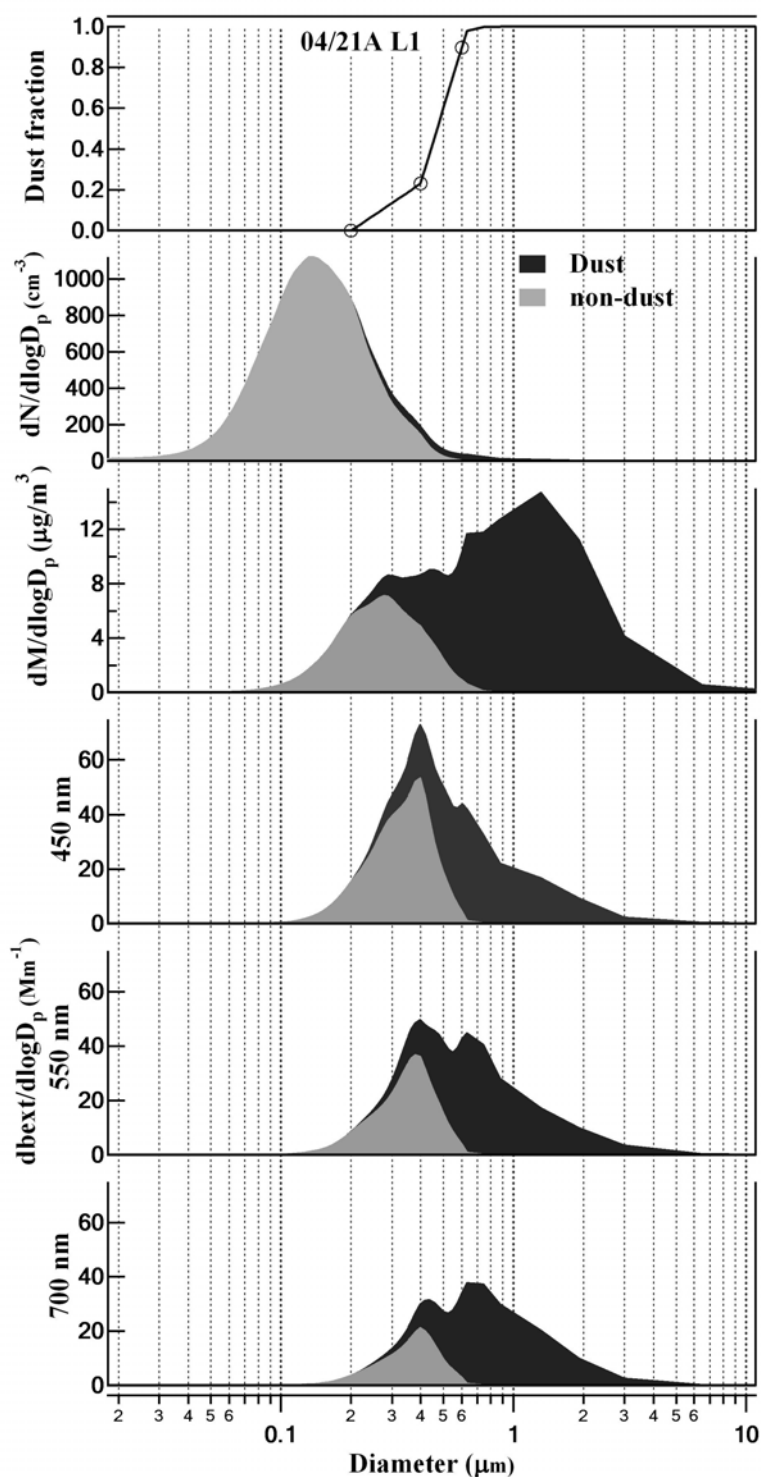


Figure 3.14. Size-dependent dust fraction and number, mass, and extinction coefficient distributions for 450, 550, and 700 nm determined for the aerosol sampled in leg L1 on 21 April. The contribution of the dust aerosol is shaded black and that of the remaining aerosol is shaded gray.

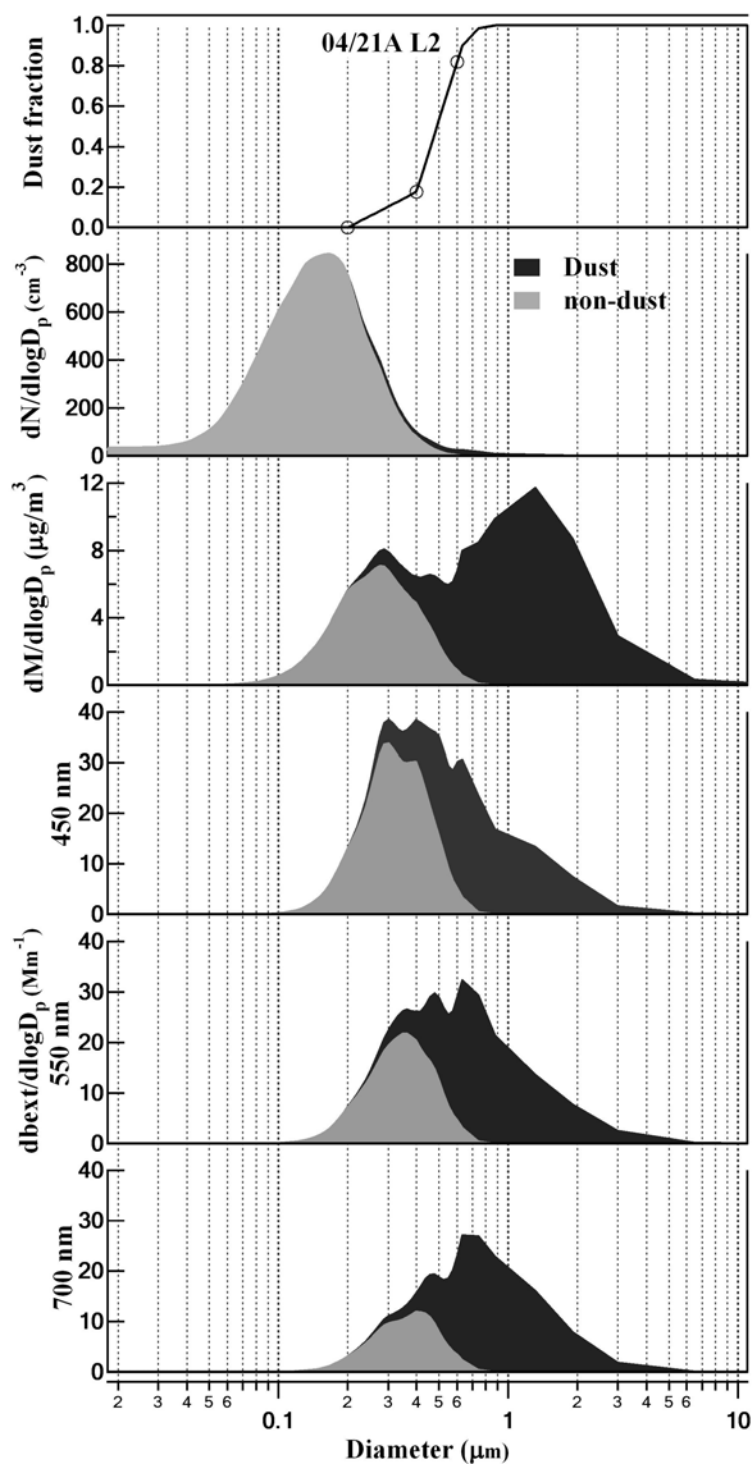


Figure 3.15. Size-dependent dust fraction and number, mass, and extinction coefficient distributions for 450, 550, and 700 nm determined for the aerosol sampled in leg L2 on 21 April. The contribution of the dust aerosol is shaded black and that of the remaining aerosol is shaded gray.

3.4.4.3 22 April

A dust layer at about 3000 m asl was identified during the initial vertical profile on 22 April. The flight levels chosen to characterize the lower, middle, and upper portions of the layer were at altitudes of approximately 2660 m, 2950 m, and 3250 m. The positions of these levels in the vertical profile are shown in Figure 3.16b, while the measured scattering coefficient during each of the horizontal flight sections is shown in Figure 3.16a. The source of the spike in scattering coefficient observed during the third level is unknown. The time response of the DMA / TDMA system is not sufficient to characterize the properties of the aerosol during the brief period, and no other instruments on board provide details regarding aerosol composition. The average total scattering coefficients measured during the L1, L2, and L3 legs are 11.7, 7.5, and 10.2 Mm^{-1} , respectively. As was true for the measurements on 21 April, a distinct dust mode is not observed in the 200 nm growth factor distribution. Therefore, the dust concentration at that size was assumed to be zero.

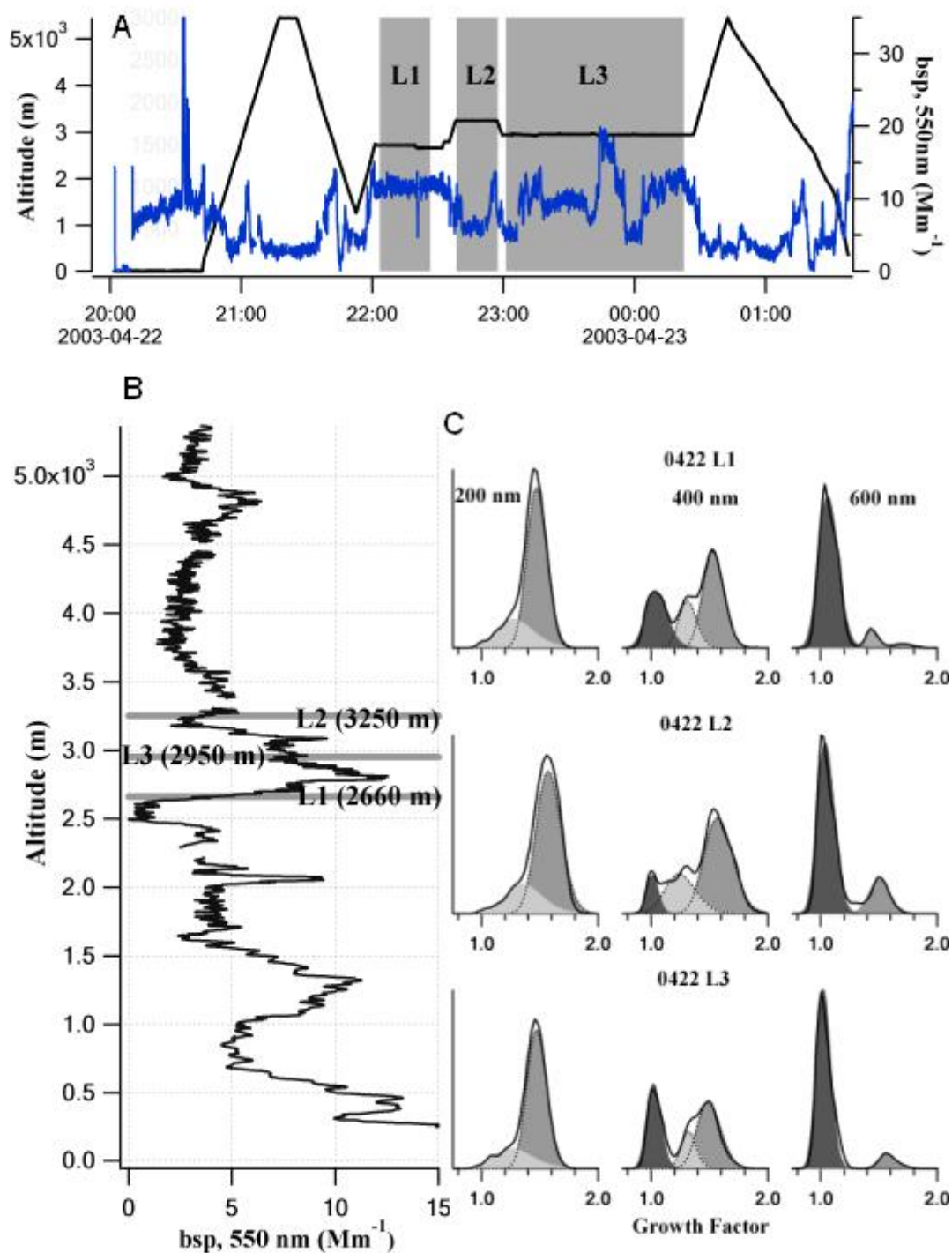


Figure 3.16. (A) Flight altitude and corresponding scattering coefficient at 550 nm for the flight on 22 April. The shaded boxes labeled L1, L2, and L3 represents the segments used in this analysis. (B) Vertical profile of the scattering coefficient (550 nm) measured with the nephelometer (C) Growth factor distributions for 200, 400, and 600 nm particles. The dust distribution is shaded dark gray.

The partitioned number, mass, and extinction size distributions for each of the three averaging intervals identified in Figure 3.16 are plotted in Figures 3.17 – 3.19. Whereas both flight legs on 21 April were within the dust layer, the difference in scattering coefficient observed in the three layers considered on 22 April suggests the dust and non-dust distributions may also differ. In fact, while the amplitudes of the dust size distributions did vary, the shapes were roughly the same. This suggests only the concentration, and not the properties, varied with height in the altitude range probed. However, the relative contribution of the dust aerosol decreased with decreasing scattering coefficient, suggesting the concentration of the other aerosol types present varied less than that of the dust. The fractional contributions of the dust to the total mass concentration measured in layers L1 and L3 within the concentrated layer were both 81%, while that in layer L2 above the dust was only 70%. A similar height dependence was observed for the dust contribution to the total extinction coefficient at 550 nm, which varied from about 78% in the dust layer to 62% above the dust layer.

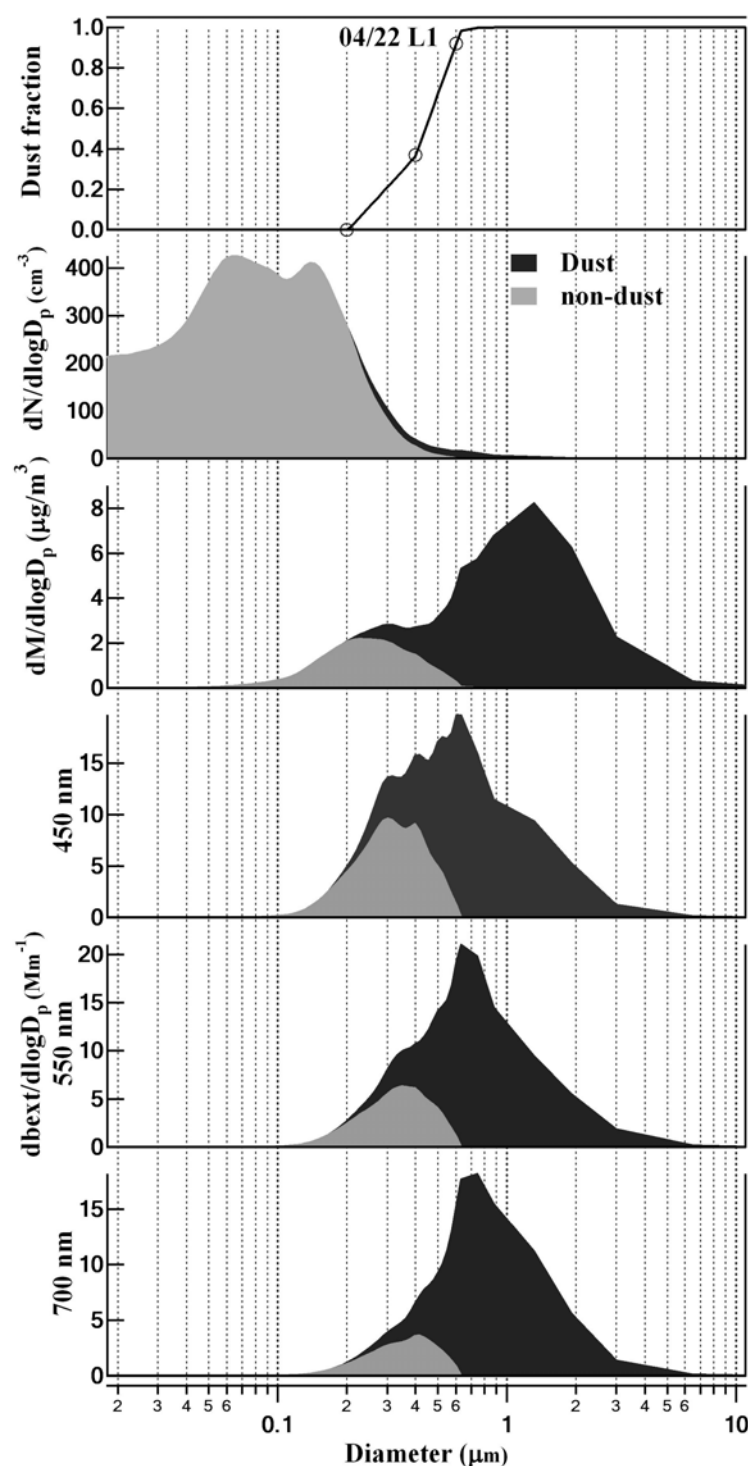


Figure 3.17. Size-dependent dust fraction and number, mass, and extinction coefficient distributions for 450, 550, and 700 nm determined for the aerosol sampled in leg L1 on 22 April. The contribution of the dust aerosol is shaded black and that of the remaining aerosol is shaded gray.

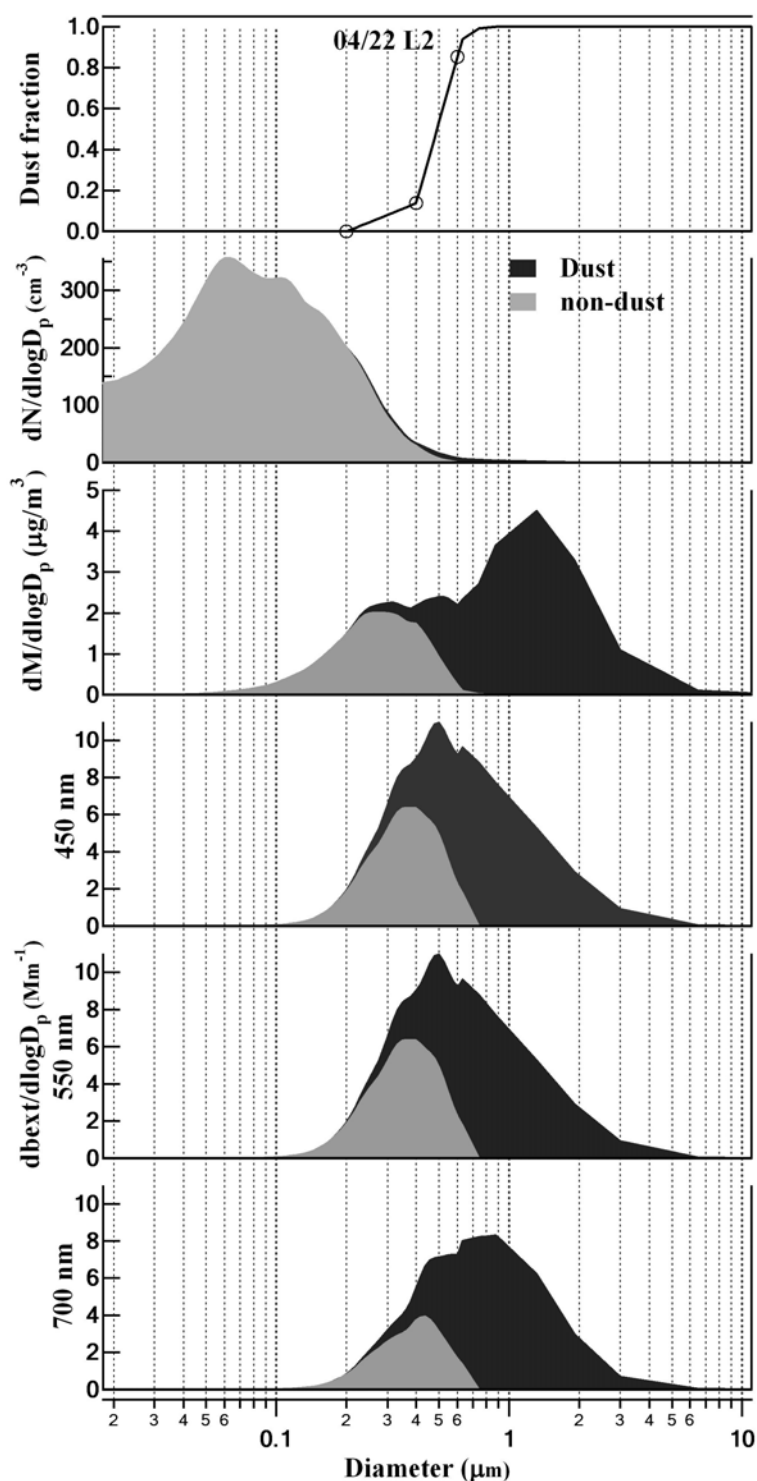


Figure 3.18. Size-dependent dust fraction and number, mass, and extinction coefficient distributions for 450, 550, and 700 nm determined for the aerosol sampled in leg L2 on 22 April. The contribution of the dust aerosol is shaded black and that of the remaining aerosol is shaded gray.

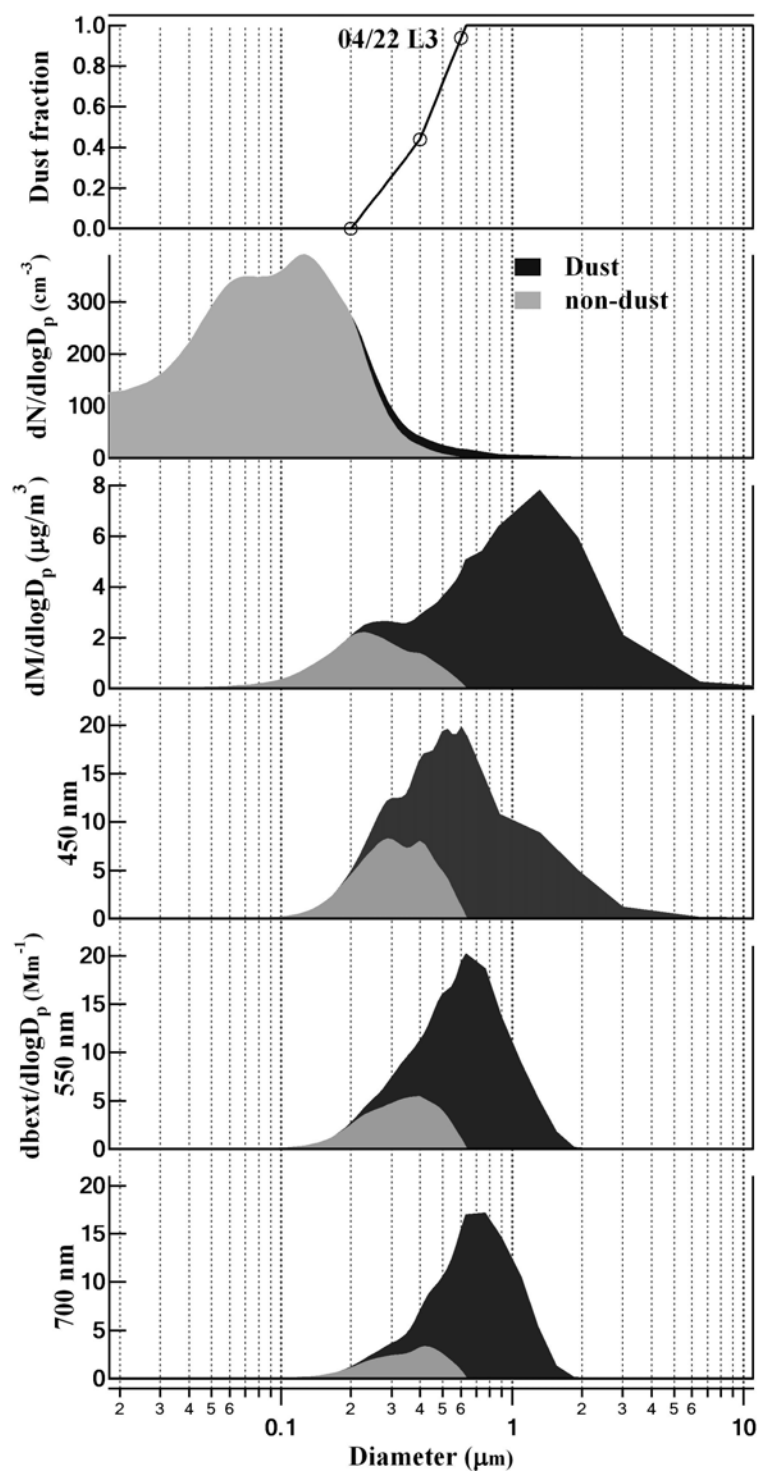


Figure 3.19. Size-dependent dust fraction and number, mass, and extinction coefficient distributions for 450, 550, and 700 nm determined for the aerosol sampled in leg L3 on 22 April. The contribution of the dust aerosol is shaded black and that of the remaining aerosol is shaded gray.

3.4.5 Comparison of predicted and measured scattering coefficients

Although optical closure was not a primary objective of this study, comparison of the scattering coefficients measured directly with the TSI nephelometer with those predicted based on the measured size distributions and hygroscopicity-based partitioning tests the accuracy of the measurements, and the assumptions and approximations used in the optical calculations. Comparisons with the sunphotometer derived extinction coefficient are not included here since those measurements were made during vertical profiles when the DMA and TDMA distributions lacked the needed time resolution. Each of the individual comparisons between measured and predicted total scattering and hemispheric backscattering coefficient are shown in Figures 3.20 and 3.21, respectively. Measured scattering coefficients at 550 nm ranged from about 7 to 25 Mm^{-1} . These values are somewhat lower than the scattering coefficients of between 15 and 40 Mm^{-1} measured off the coast of Washington State during significant Asian dust events [Jaffe *et al.*, 1999]. A correlation coefficient, R^2 , of 0.948 was found between measured and calculated total scattering coefficients, while a value of 0.955 was found for the backscattering coefficients. A best fit slope of less than 1 was found for both the total and hemispheric backscattering relationships, indicating that the predictions underestimated the directly measured values. Among the possible sources of this discrepancy are particle losses in the sizing probe inlets, sizing or concentration errors in the DMA or CAS_forward data, or errors introduced by assumptions made in the calculations. Treating dust particles as homogeneous spheres is obviously unrealistic, and may lead to inaccuracy in the calculations, as might assuming all non-dust particles

have the same composition. Despite the differences between the measured and predicted quantities, the relatively strong correlation between them suggests the dataset is robust and that the quantities determined using this dataset are expected to be accurate.

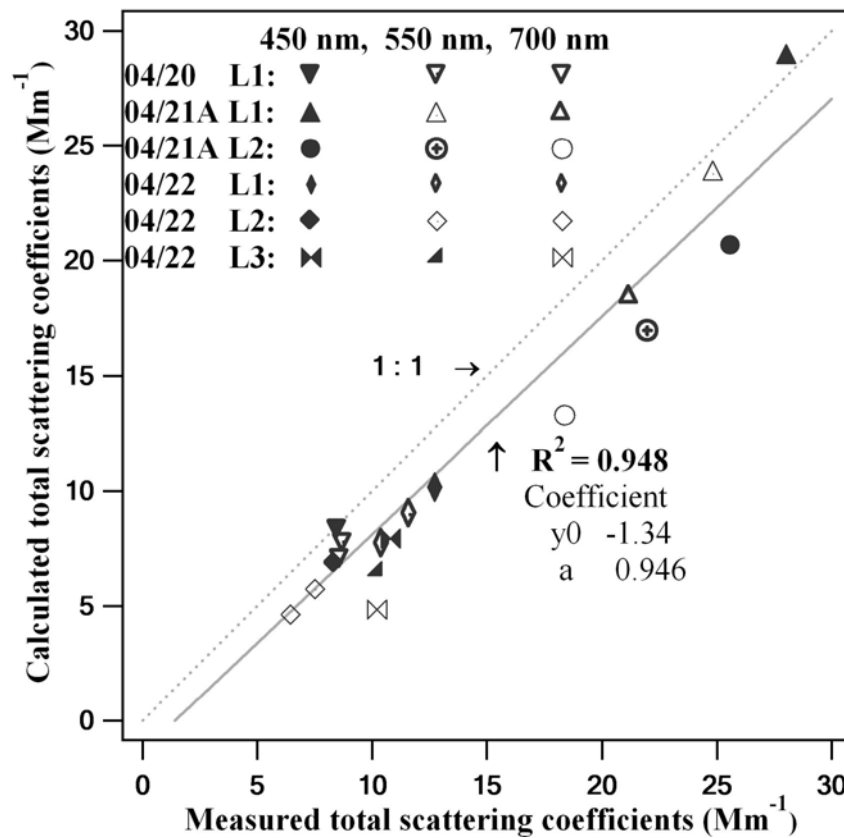


Figure 3.20. Closure comparisons between directly measured and derived total scattering coefficient for 450, 550, and 700 nm wavelengths.

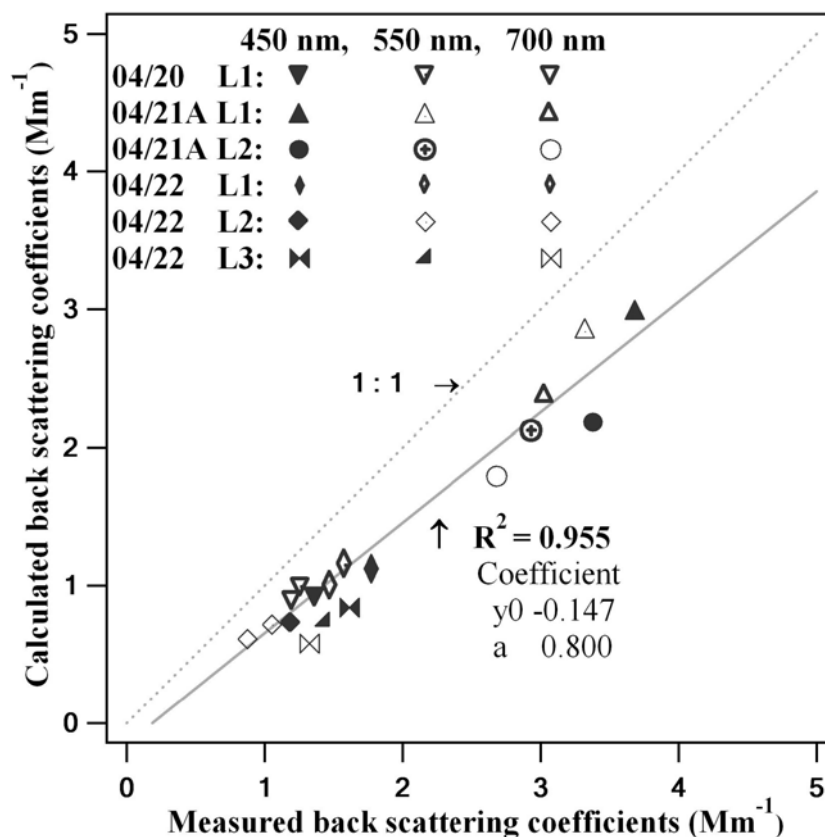


Figure 3.21. Closure comparisons between directly measured and derived hemispheric backscattering coefficient for 450, 550, and 700 nm wavelengths.

3.4.6 Mass extinction efficiencies

The mass extinction efficiency of dust or any other aerosol type provides a link between mass concentration that is typically tracked in regional and global models, and optical behavior, which is more commonly measured. Mass extinction efficiencies are generally greatest for submicron pollution aerosols and lowest for optically-inactive particles smaller than $\sim 0.1 \mu\text{m}$, and for coarse mode particles for which extinction increases roughly with the square of the particle diameter, whereas the mass increases with its cube. The focus of the ADAM-2003 project, and the focus of this analysis is on the dust aerosol. Therefore, mass extinction efficiencies for dust were calculated

separately from those for the remaining aerosol. Gravitational settling of the largest dust particles during transit across the Pacific is expected to increase the mass extinction efficiency as the residual size distribution is shifted towards smaller, more optically-efficient particles. The dust and non-dust mass concentrations determined for each of the six flight levels analyzed are summarized in Table 3.4. The range in these values from 4.73 to 9.12 $\mu\text{g}/\text{m}^3$ bounds the reported concentration of 5 $\mu\text{g}/\text{m}^3$ for Asian dust reaching Oregon during periods of enhanced transport between 1989 and 1999 [VanCuren, 2003]. Throughout this study, the fractional contribution of dust to the overall mass extinction coefficient ranged from 0.68 to 0.93. Of course, the flights were conducted in locations and at altitudes thought to have the highest dust concentrations. Nevertheless, these data indicate that dust transported thousands of kilometers represents a significant fraction of the total aerosol loading. VanCuren [2003] reported a fractional contribution of 0.72 in Oregon averaged over the enhanced transport season. The flight-level averaged extinction coefficients for 450, 550, and 700 nm wavelengths that represent the numerator in the mass extinction efficiency relationships are provided in Table 3.5.

Table 3.4. Estimated mass concentration ($\mu\text{g}/\text{m}^3$) for dust and non-dust fractions. Values in parentheses represent the fractional contribution of the dust to the total concentration.

Date		Dust	Non-Dust
04/20	L1	5.61 (.93)	0.40
04/21A	L1	9.12 (.69)	4.10
04/21A	L2	6.71 (.68)	3.18
04/22	L1	4.73 (.81)	1.15
04/22	L2	2.43 (.70)	1.03
04/22	L3	4.58 (.81)	1.05

Table 3.5. Estimated extinction coefficients (Mm^{-1}) for dust and non-dust fractions. Values in parentheses represent the fractional contribution of dust to the total extinction coefficients.

Dust				Non-Dust		
Date	450 nm	550 nm	700 nm	450 nm	550 nm	700 nm
04/20 L1	8.88 (.863)	8.46 (.903)	7.77 (.941)	1.41	0.91	0.49
04/21A L1	17.55 (.519)	17.08 (.619)	15.34 (.730)	16.27	10.52	5.66
04/21A L2	11.83 (.489)	11.73 (.597)	10.91 (.719)	12.34	7.92	4.26
04/22 L1	8.17 (.671)	8.09 (.760)	7.55 (.847)	4.01	2.55	1.36
04/22 L2	4.11 (.511)	4.10 (.616)	3.88 (.737)	3.94	2.56	1.39
04/22 L3	8.35 (.695)	8.14 (.778)	7.45 (.858)	3.66	2.32	1.24

Mass extinction efficiencies of the two aerosol types are calculated by dividing the extinction coefficients by the corresponding mass concentration. As shown in Figure 3.22 and listed in Table 3.6, the study-average mass extinction efficiencies ranged from $1.92 \text{ m}^2/\text{g}$ (450 nm) to $1.38 \text{ m}^2/\text{g}$ (700 nm) for dust, and from $3.96 \text{ m}^2/\text{g}$ to $1.17 \text{ m}^2/\text{g}$ for the non-dust aerosol. *Reid et al.* [2003] noted that the accuracy of mass extinction efficiencies for dust are sensitive to uncertainties in particle density. *Maring et al.* [2003] found that the mass extinction efficiency of a Saharan dust aerosol increased to $0.7 \sim 0.8 \text{ m}^2/\text{g}$ at 550 nm after being transported across the Atlantic. The study-average

mass extinction efficiency at 550 nm of $1.72 \text{ m}^2/\text{g}$ calculated using these data may be higher than that reported by *Maring et al.* [2003] due to differences in the size distribution of the dust soon after it is generated or due to enhanced loss of the larger particles during transit. Interestingly, the mass extinction efficiency of the dust aerosol actually exceeds that of the non-dust particles at 700 nm. This reversal is caused when the smaller non-dust particles shift into the optically-inactive range as the size parameter decreases.

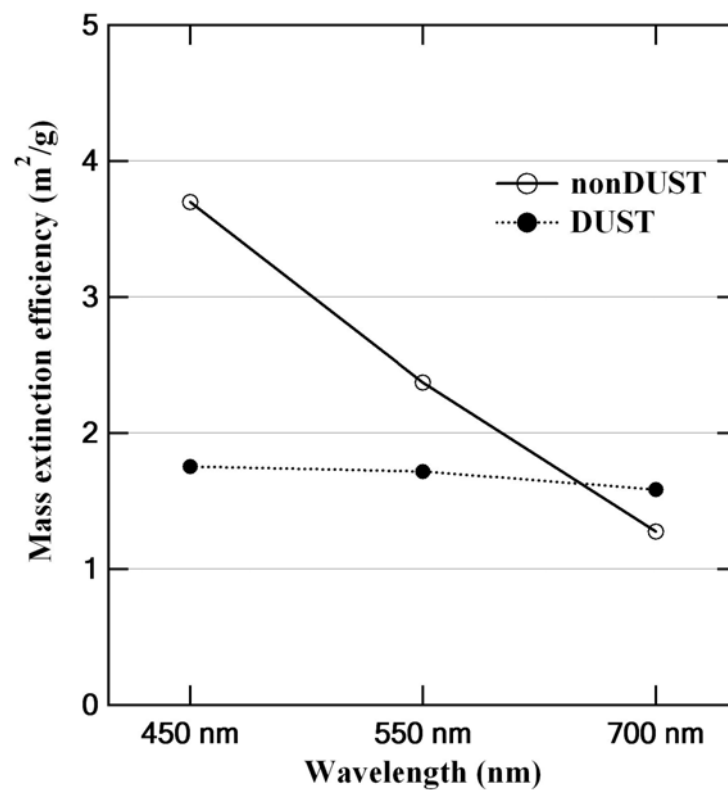


Figure 3.22. Averaged mass extinction efficiencies for dust and non-dust aerosols.

Table 3.6. Mass extinction efficiencies for dust and non-dust aerosols.

		Dust			Non-Dust		
Date		450 nm	550 nm	700 nm	450 nm	550 nm	700 nm
04/20	L1	1.58	1.51	1.38	3.53	2.27	1.23
04/21A	L1	1.92	1.87	1.68	3.96	2.56	1.38
04/21A	L2	1.76	1.75	1.63	3.88	2.49	1.34
04/22	L1	1.73	1.71	1.60	3.50	2.22	1.19
04/22	L2	1.69	1.69	1.60	3.84	2.49	1.35
04/22	L3	1.82	1.78	1.63	3.47	2.20	1.17
Average		1.75	1.72	1.59	3.70	2.37	1.28

3.5 Summary and conclusions

Aerosol physical and optical properties were measured with a DMA, a CAS, a TDMA, and a nephelometer on board a Twin Otter aircraft during the ADAM-2003 experiment. This study was designed to investigate the transport of Asian dust and to characterize the optical, physical, and hygroscopic properties of that aged dust upon reaching the California coast. During several of the flights, distinct layers of dust that had been preserved during the transit across the Pacific were observed. These layers were typically present between 2 and 4 km asl.

By coupling the measured size distributions with a size-dependent fractional categorization based on the hygroscopic growth measurements, independent size distributions for the dust and other aerosol types were created. The fractional contribution of dust to the overall concentration increased significantly between 200 nm and 600 nm diameter. Extrapolation of the size-dependent fractional contribution of dust beyond the size range covered by the TDMA suggests that, within the elevated layers probed during the study, almost all particles larger than about 700 nm were dust. Even

in the concentrated dust layers, the number concentration of other particle types far exceeded that of the dust. In contrast, both the overall mass concentration and light extinction coefficient were dominated by the larger dust particles. Light scattering coefficients predicted based on the measured size distributions compared well with those directly measured with a nephelometer. Although optical closure was not a primary objective of the ADAM-2003 study, the good agreement provides confidence in the derived quantities. The calculated mass extinction efficiency of the dust aerosol was somewhat higher than that observed during other studies suggesting that the size distribution had shifted towards smaller size as gravitational settling removed the largest dust particles.

CHAPTER IV

DERIVED CCN SPECTRA OF AN AGED BIOMASS BURNING AEROSOL

During May of 2003, smoke from fires on the Yucatan Peninsula was transported across the Gulf of Mexico and into Texas where it caused a significant enhancement in measured aerosol concentrations. The 24-hour average PM_{2.5} concentration measured in Austin on May 10 was 50.1 $\mu\text{g}/\text{m}^3$, which was more than twice that of the highest daily-average concentration measured during any other month in 2003. During this event, a differential mobility analyzer (DMA) / tandem differential mobility analyzer (TDMA) system was used to characterize the size distribution and size-resolved hygroscopicity and volatility of the aerosol. The hygroscopicity data were used to separate the sparingly hygroscopic biomass burning particles from other aerosol types. By coupling the size-resolved fraction of particles attributed to the fires with the overall size distribution, it was possible to construct a biomass burning aerosol-only size distribution. This distribution, and the aerosol properties derived from the TDMA data, were used to examine the impact of the smoke on cloud condensation nuclei (CCN) spectra. The derived CCN spectra were used to predict the impact of the smoke on cloud droplet number concentration, and the impact of additional aerosol types on the activation efficiency of the biomass burning aerosol.

4.1 Introduction

Biomass burning contributes significantly to aerosol concentrations in many regions of the world. The global emission of organic and black carbon aerosols from biomass burning has been estimated to range from 10 to 30 and 6 to 9 Tg/yr, respectively [Penner *et al.*, 1993; Cooke and Wilson, 1996; Lioussse *et al.*, 1996; Cooke *et al.*, 1999]. Much of the recent research on biomass burning aerosols has been focused on their direct radiative impact through scattering and absorption of sunlight. Although there remains considerable uncertainty regarding the magnitude of this impact, it is believed that the single scattering albedo of most biomass burning aerosols is sufficiently high to lead to a net cooling [Haywood and Boucher, 2000; Christopher *et al.*, 2000; Li *et al.*, 2000; Ramanathan *et al.*, 2001].

The integrated radiative impact of any aerosol is dependent not only on its optical properties, but also on its lifetime. Because most particles generated during biomass burning have diameters less than a few tenths of a micron, they are not efficiently removed through sedimentation. Therefore, their removal rate is strongly influenced by the efficiency with which they activate in cloud. Additionally, the cloud nucleating properties of biomass burning particles controls the influence of the aerosol on cloud albedo [Nenes *et al.*, 2001; Peng *et al.*, 2002; Menon *et al.*, 2002] and cloud lifetime [Rotstayn, 1999; Haywood and Boucher, 2000; Lohmann and Lesins, 2002]. Despite a significant effort to better characterize the activation properties of carbonaceous aerosols, there still remains considerable uncertainty [Hameri *et al.*, 2001; Roberts *et al.*, 2002; Raymond and Pandis, 2002]. Although there is uncertainty regarding the activation

properties of biomass burning particles, there is observational evidence that these aerosols can alter cloud properties [*Rosenfeld, 1999; Murray et al., 2000; Roberts et al., 2003; Andreae et al., 2004*]

Further complicating the assessment of the influence of smoke aerosol on cloud properties is the paucity of data describing the degree to which it is altered during transport. The properties of freshly emitted biomass burning particles may differ substantially from those following exposure to oxidants and condensable gases over periods ranging from hours to weeks. Unfortunately, as the biomass burning aerosol becomes more dilute relative to other natural and anthropogenic particle types, it becomes difficult to isolate its properties from those of the entire aerosol population. Simply measuring the CCN concentration in a region impacted by smoke may provide ambiguous results when the concentrations of other particle types are non-negligible.

Biomass burning in and adjacent to the Yucatan Peninsula each spring frequently contributes to elevated particulate matter concentrations in the United States. The magnitude of the impact varies with draught conditions in the burning region, and with meteorological conditions during the burning events. A severe episode in the spring of 1998 has been the focus of a number of studies aimed at characterizing the composition [*Fraser and Lakshmanan, 2000*] and optical properties [*Kreidenweis et al., 2001*] of the smoke, and the impact of the smoke on lightning characteristics [*Murray et al., 2000*]. This paper describes data collected during an episode in 2003 that, despite being shorter in duration than that in 1998, resulted in a substantial increase in particulate matter concentrations throughout much of Texas and bordering states.

4.2 2003 smoke episode

Smoke from fires in agricultural regions on and near the Yucatan Peninsula during May of 2003 was transported across the Gulf of Mexico and into Texas, where it caused a significant enhancement in aerosol loadings. Figure 4.1 shows the distribution of peak PM 2.5 concentration (mass concentration of all particulate matter having a diameter less than 2.5 μm) on May 10. The site at which the measurements described here were made (College Station) along with additional sites at which particulate matter measurements were made during the smoke episode are identified in the figure. The data used to generate this plot were recorded by the Texas Commission on Environmental Quality (TCEQ). The center of the smoke plume passed through central Texas, resulting in the observed maxima in PM2.5 concentrations.

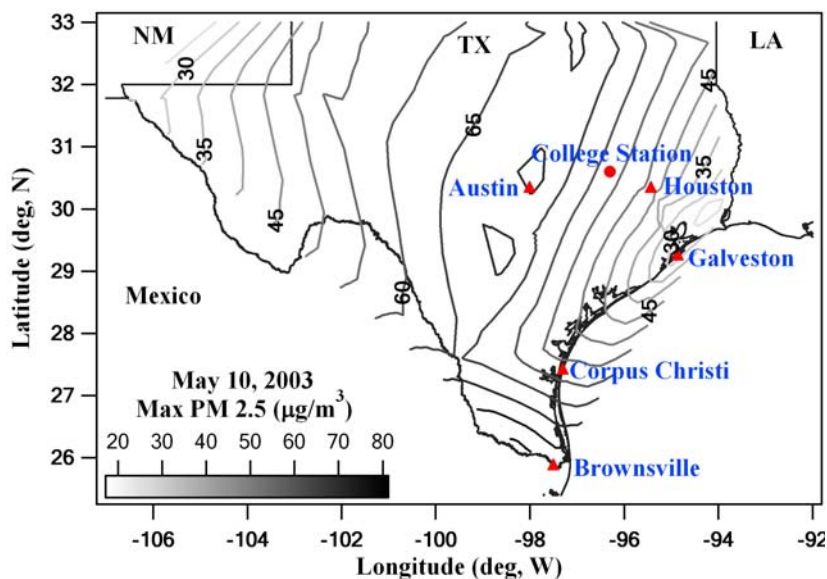


Figure 4.1. Measurement locations and maximum PM 2.5 concentrations on May 10, 2003 (circle: Texas A&M University, triangles: TCEQ sites).

Figure 4.2 shows a timeline of PM 2.5 mass concentration at several TCEQ sites from May 1 to 15. The maximum hourly PM2.5 concentration measured in several cities in Texas between 6 and 11 May was about $70 \sim 80 \mu\text{g}/\text{m}^3$. Elevated concentrations were observed throughout the State from the southernmost tip in Brownsville, north through Corpus Christi, Galveston, and Austin. Both satellite images and calculated backtrajectories confirm that the source of the concentrated aerosol was the Yucatan Peninsula. The episode terminated rapidly with the passage of a cold front on May 11. Throughout much of the period during which particulate matter concentration was elevated, our group measured the properties and size distribution of this aged aerosol in College Station, Texas. The specific time interval over which these measurements were made is identified in Figure 4.2. Although PM2.5 is not measured in or nearby College Station, the influence of the smoke is reflected in the reduced visibility recorded at Easterwood Airport in College Station shown in Figure 4.3. The abrupt improvement in visibility on May 11 corresponds to the frontal passage.

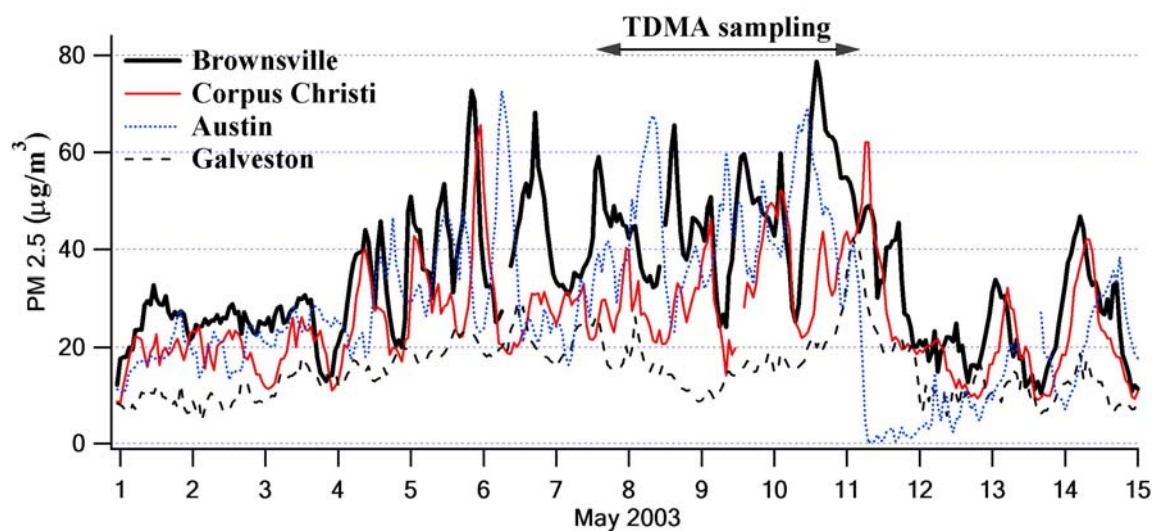


Figure 4.2. Hourly PM 2.5 concentrations at four TCEQ cities during the measurement period.

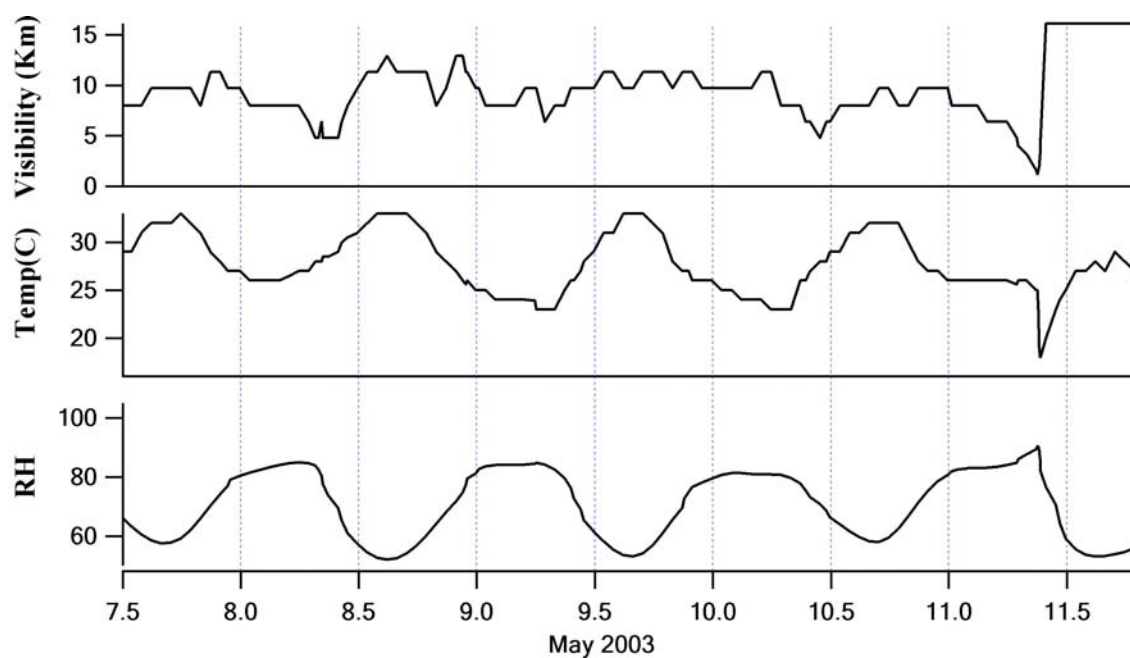


Figure 4.3. Time series of visibility, temperature, and relative humidity recorded at Eastwood airport in College Station, Texas. Along the x-axis, 8.0 corresponds to midnight on May 8, and 8.5 corresponds to noon on May 8.

Although measurements of PM_{2.5} concentration do not offer insight into the contribution of the biomass burning aerosol, the enhancement in PM_{2.5} in 2003 relative to that recorded during the same period in 2002 reflects the impact of the smoke. Figure 4.4 shows the PM_{2.5} concentration recorded in Houston and Galveston during the study period. The light grey shaded regions represent the average PM_{2.5} concentrations measured at each site during the same period in 2002. Similar enhancements were observed at almost all sampling locations in the eastern half of Texas. The impact of the smoke is also apparent in the box plots shown in Figure 4.5. In these plots, the edges of the boxes represent the 25th and 75th percentiles, the whiskers represent the 10th and 90th percentiles, and the dots represent the 95th percentile.

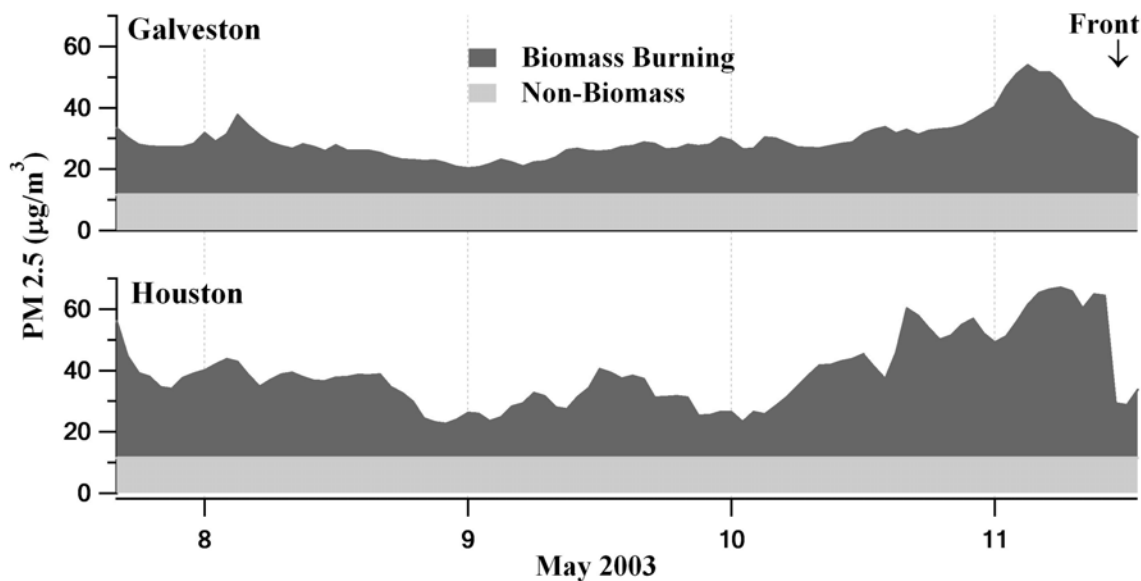


Figure 4.4. PM_{2.5} concentrations recorded in Houston and Galveston during the smoke episode in May, 2003. The light shaded area in each graph represents the average PM_{2.5} concentration measured at each of the sites during the same time period in May of 2002.

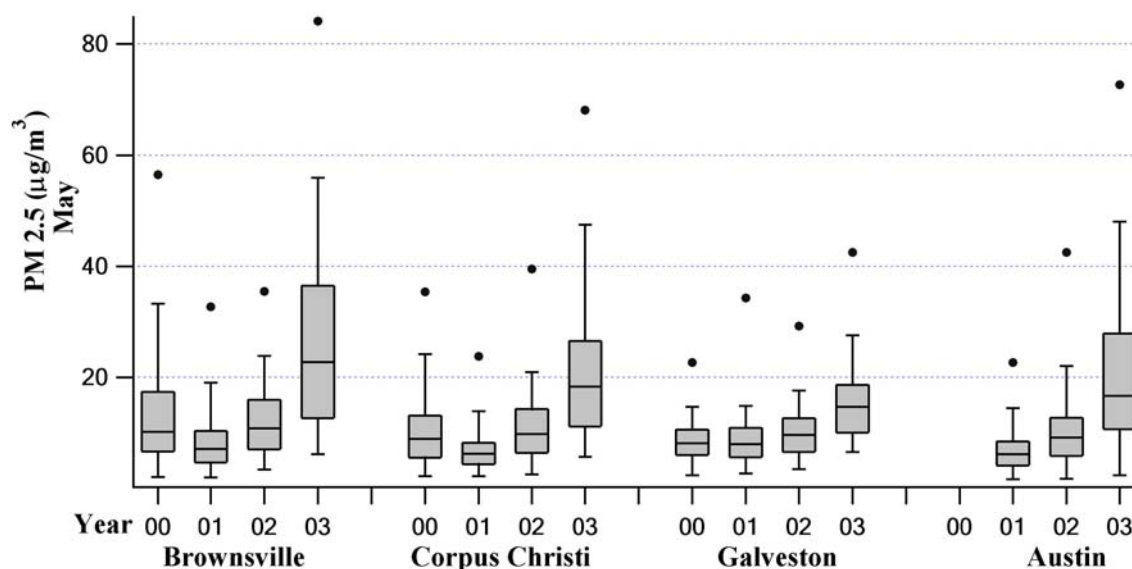


Figure 4.5. Box plots of hourly PM 2.5 mass concentrations recorded at four cities in Texas in the month of May between 2000 and 2003.

4.3 In situ measurements

4.3.1 DMA/TDMA

A differential mobility analyzer / tandem differential mobility analyzer (DMA / TDMA) system was used to characterize aerosol size distributions and size-resolved hygroscopic growth. Although not a direct measure of cloud nucleating ability, aerosol hygroscopicity can be used to constrain in-cloud behavior. Measured hygroscopicity is typically quantified by the growth factor (GF), which is simply the ratio of the diameter of a particle following exposure to high RH (D_p) to its initial, or dry, diameter at low RH, D_p^* . Swietlicki *et al.* [1999, 2000] categorized hygroscopicity into commonly observed

growth factor ranges of about 1.0 for non- hygroscopic particles, 1.11 ~ 1.15 for less hygroscopic particles, 1.38 ~ 1.69 for more hygroscopic particles, and 2.08 ~ 2.21 for sea salt particles. Measured hygroscopic growth is often used to roughly separate the hygroscopic inorganic component from the less hygroscopic organic component. *Dick et al.* [2000] studied the influence of organic carbon on particle hygroscopic growth during the Southeastern Aerosol and Visibility Study. They reported that the water content associated with organics is considerably less than that associated with sulfate compounds for high RH conditions. The DMA / TDMA system used in this study is described in *Gasparini et al.* [2004]. Throughout this study, the DMA was used to characterize the size distribution of particles having diameters between 0.01 and 0.75 μm , while the TDMA was used to measure the size-resolved hygroscopicity of particles with dry diameters of 25, 50, 100, 200, 300, 450, and 600 nm. For fixed-RH TDMA measurements, the RH between the two DMAs was controlled to 85% using a multi-tube Nafion bundle. A calibration routine in which the aerosol separated by the first DMA was not perturbed prior to classification by the second DMA was automatically completed every night shortly after midnight. Any shift in growth factor from the expected peak at 1.0 was used to correct data collected the following day.

4.3.2 RH scans

To complement the measurements of hygroscopic growth at fixed RH, the instrument was intermittently operated as a humidity scanning TDMA (HS-TDMA). In this mode of operation, the relative humidity is continuously scanned between about

85% and 30%, and then back up to 85% again, while the growth factor distributions of particles having dry diameters of 50, 100, and 200 nm are continuously measured.

During the increasing RH portion of the measurement, the aerosol is pre-humidified to greater than 85% RH to ensure that all hygroscopic species are hydrated prior to exposure to the final, variable, RH. Combined, the increasing and decreasing RH measurements describe the growth behavior of the aerosol on the upper and lower legs of any hygroscopic growth hysteresis loop. A single RH scan for one particle size requires between 45 minutes and an hour.

4.3.3 Humidified temperature scans

The size-resolved volatility of 50, 100, and 200 nm particles was also examined by varying the temperature to which particles were exposed between the two DMAs. Although the instrument used to measure aerosol volatility was the same as that used to characterize hygroscopicity, it will be referred to here as a Humidified Temperature-scanning TDMA (HT-TDMA). The temperature at which partial or complete volatilization of specific classes of particles occurs provides insight into their composition. In this mode of operation, following classification of a dried aerosol by the upstream DMA, the size-resolved particles are introduced into a heated tube in which the temperature is varied from 300 °C to ~40 °C. The aerosol heater has been designed to provide sufficient residence time at high temperature to ensure adequate volatilization of larger particles. The particles that do not fully volatilize are then exposed to a controlled relative humidity of about 85%, and the resulting distribution is measured by the

downstream DMA that scans across particle size. The volatility properties of the hygroscopic and non-hygroscopic populations of particles determined in this way can be used to infer their composition. As with the RH-scans, each temperature scan requires about 45 minutes to an hour to complete.

4.3.4 Time resolution of measurements vs. temporal variability of the aerosol

As operated during this study, a single measurement sequence consisted of a size distribution measurement, fixed-RH hygroscopic growth measurements at each of the seven sizes identified above, and both RH and temperature scans for particles having dry diameters of 50, 100, and 200 nm. A single measurement required approximately 7-8 hours to complete. Whereas this time resolution would be inadequate to characterize rapidly evolving aerosols in an urban area, the concentration and properties of the smoke aerosol varied slowly over the four-day sampling period. Therefore, although the different measurements were not made simultaneously, the error introduced by combining them into a single description of the aerosol is thought to be relatively small.

4.4 Analysis procedure

4.4.1 Distribution parameterizations

Aerosol size distributions and hygroscopic growth factors were fitted using between one and four lognormal distributions. The lognormal distribution often provides a good fit to particle distributions and is regularly used in atmospheric

applications [Seinfeld and Pandis, 1998]. The distribution is prescribed by the following relationship

$$\frac{dN_i}{d \log D_p} = \frac{N_i}{\sqrt{2\pi} \cdot \log(\sigma_{g,i})} \exp \left[-\frac{(\log D_p - \log D_{pg,i})^2}{2 \cdot (\log \sigma_{g,i})^2} \right], \quad (4.1)$$

where N_i is the total number concentration, $D_{pg,i}$ is the geometric mean diameter, and $\sigma_{g,i}$ is the geometric standard deviation for mode i . This fitting procedure permitted identification of distinct particle types that were present throughout the study.

4.4.2 Hygroscopicity-based partitioning

Despite the variability observed in measured hygroscopic growth factor distributions, several distinct modes were observed in almost all recorded distributions. Each of these modes consists of a population of particles having similar characteristics. Relying both on the measured hygroscopicity and on expectations based on trajectories, satellite images, and past measurements in this region, the five particles types observed were classified into the following five categories: sulfate, sulfate/organic mixture, biomass burning, local organic, and hydrophobic. Not all five particle types were observed in all distributions. The hydrophobic class is believed to be comprised of primary soot and organic carbon containing particles. These hydrophobic particles were only detected in the TDMA measurements of the smaller particles considered. The origin of these particles is unknown. The local organic particles were considered separately from the biomass burning particles even though the two populations had similar hygroscopic properties. The groups were separated primarily to produce more

physically plausible size distributions than would be possible were they combined. The relative concentration within each of the modes was used to partition the size-resolved aerosol into the five classes identified above, while the median growth factor in each of the modes was used to predict cloud activation efficiency. Figure 4.6 shows an example of hygroscopic growth factor distributions measured during the sequence centered at 02:20 CDT on May 10, 2003. As was true for most of the measurements made during this period, growth factor distributions shown in this figure were typically bimodal. The concentrated less hygroscopic mode consists of biomass burning particles, whereas the more hygroscopic mode consists of sulfate-containing particles. Although it is partially obscured by adjacent modes, a mode having intermediate hygroscopicity (sulfate / organic mixture) was also present in almost all distributions. This intermediate mode is shown in the lognormal fits of the 100 and 600 nm particle distributions shown in Figure 4.7. The number fraction, geometric mean, and standard deviation of the lognormal distributions used to describe the growth factor distributions are provided in Table 4.1.

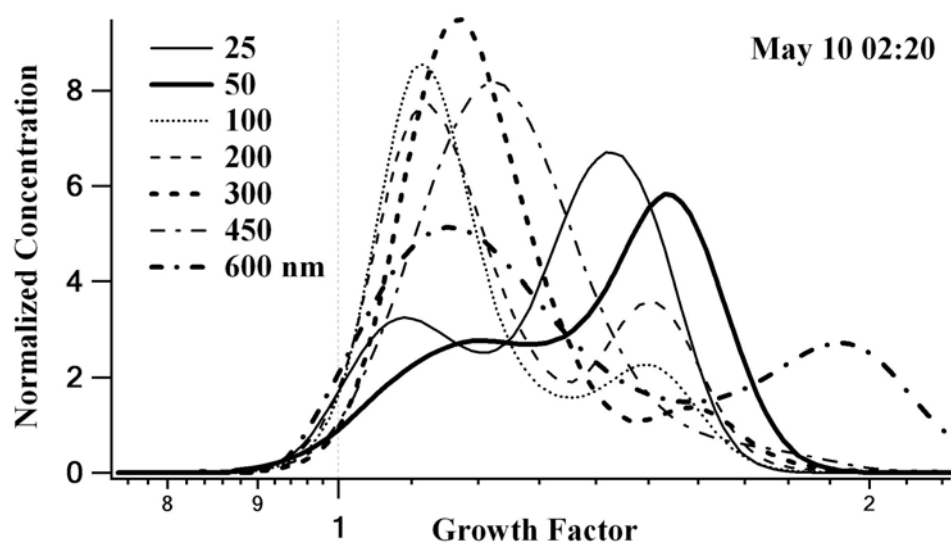


Figure 4.6. Fixed-RH hygroscopic growth factor distributions measured at 02:20 CDT on 10 May 2003.

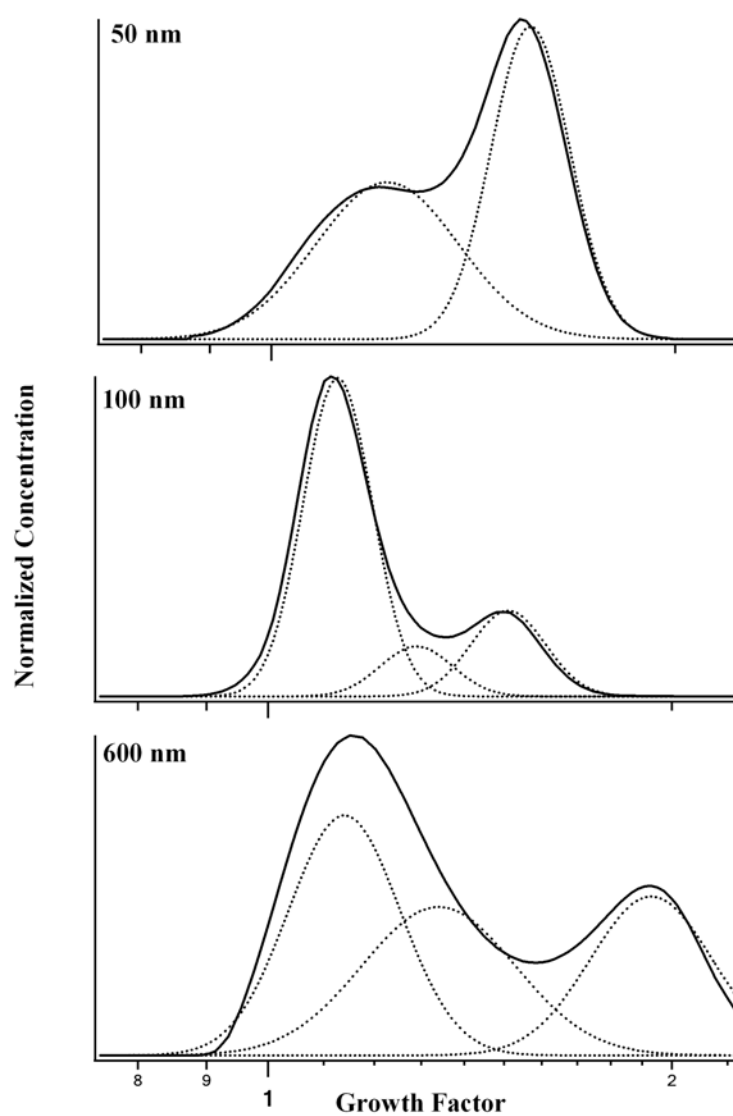


Figure 4.7. Example lognormal curve fits to growth factor distributions for 50, 100 and 600 nm particles on 10 May 2003. The dotted lines represent the lognormal fits, while the solid lines represent the measured distributions.

Table 4.1. The number fraction N , geometric mean diameter D_{pg} , and geometric standard deviation σ_g for the lognormals used to fit the growth factor distributions measured on May 10 at 02:20.

Diameter/ Modes	N			D_{pg}			σ_g		
	1	2	3	1	2	3	1	2	3
25 nm	0.303	0.406	0.291	1.096	1.378	1.484	1.077	1.082	1.066
50 nm	0.265	0.244	0.492	1.136	1.338	1.561	1.099	1.101	1.071
100 nm	0.683	0.122	0.195	1.120	1.279	1.507	1.061	1.064	1.066
200 nm	0.604	0.114	0.282	1.124	1.273	1.511	1.068	1.057	1.067
300 nm	0.782	0.113	0.105	1.171	1.336	1.595	1.073	1.059	1.069
450 nm	0.882	0.082	0.036	1.225	1.451	1.753	1.104	1.107	1.085
600 nm	0.389	0.325	0.286	1.132	1.330	1.921	1.095	1.140	1.107

The size-resolved fractional categorization described above was combined with the concurrently measured aerosol size distribution to create independent size distributions for each of the particle types considered. Figure 4.8 shows the total aerosol number concentrations obtained during the biomass burning episode. The thick solid line represents the number size distribution measured during the same 02:20 CDT, May 10, 2003 sequence described above. Since hygroscopic growth factor distributions were only measured for a limited number of particle sizes, the size-resolved fractional categorization was linearly interpolated or extrapolated to each of the bins within the measured total size distributions. Figure 4.9 shows the size-resolved fractional categorization and resulting particle-type size distributions for the example distributions considered. The sum of the four single particle type size distributions shown in Figure 4.9 is equal to the overall size distribution shown in Figure 4.8. The concentration of hydrophobic particles in these distributions was negligible. To simplify introduction of

the particle properties into the cloud model described below, each of the single particle type size distributions was fitted using one or two lognormals.

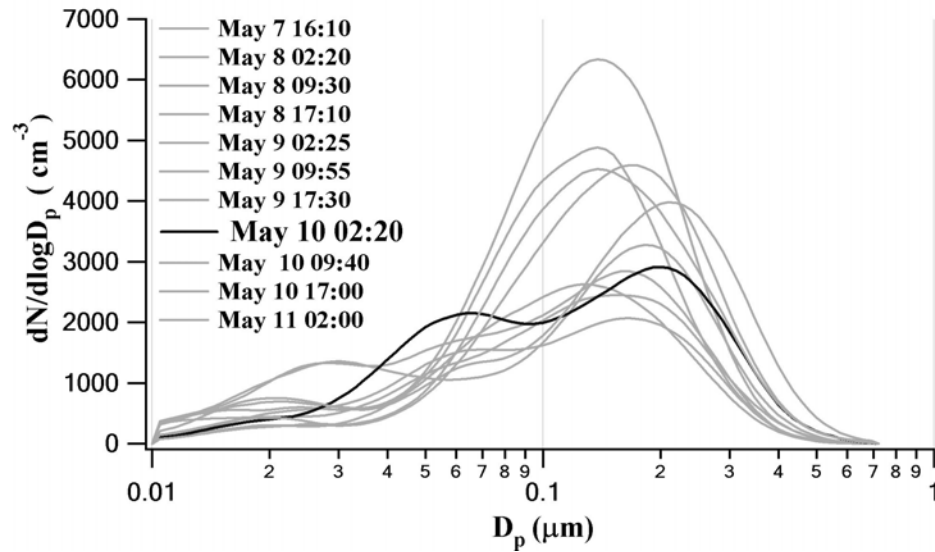


Figure 4.8. All aerosol size distributions measured during the smoke episode. The solid line represents the measurement made at 02:20 on 10 May 2003.

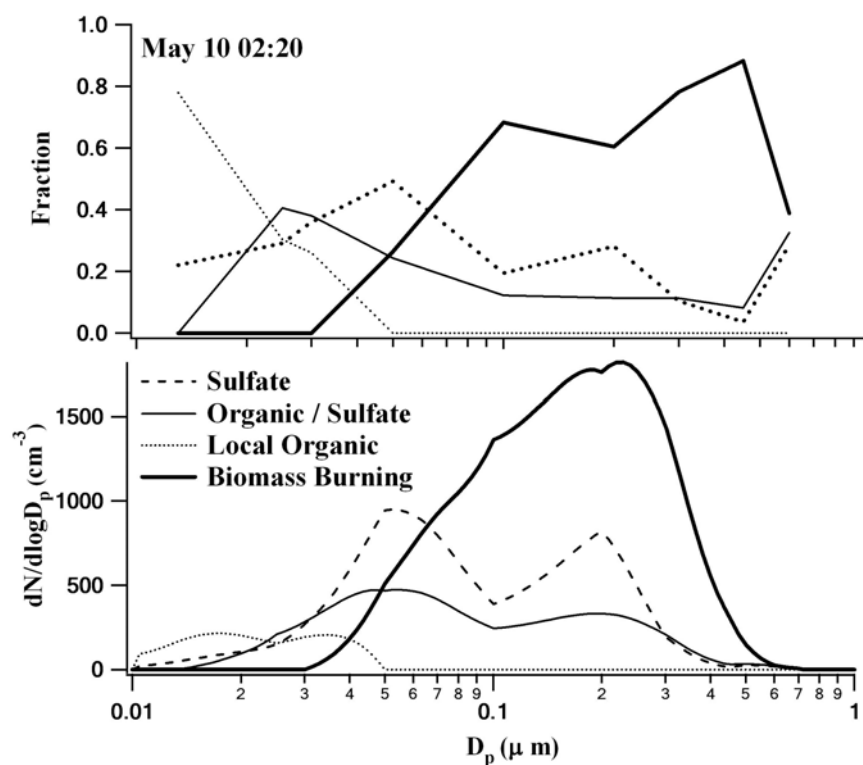


Figure 4.9. Size-resolved fractional categorization of the aerosol (top) and single particle-type size distributions (bottom) for the aerosol measured during the sequence centered at 02:20 CDT on May 10, 2003.

4.4.3 Extrapolation of growth factor to S_c (critical supersaturation)

Inference of aerosol critical supersaturation from size-resolved hygroscopicity measurements requires assumptions and approximations that are unnecessary for interpretation of direct CCN measurements. However, a direct measurement of CCN concentration provides no detail of the contribution of different particle types. The technique used here to isolate the properties and size distribution of the biomass burning aerosol permits examination of these aged particles even in the presence of a number of other particle types. The median hygroscopic growth factor of the biomass burning aerosol mode was used to determine the relative abundance of soluble and insoluble

mass within the particles. For these calculations, the soluble fraction was assumed to be composed of ammonium bisulfate. This compound was selected based on the RH-dependent growth of the aerosol measured during the RH-scans. The size and soluble content of the aerosol are uniquely related to the critical supersaturation through Köhler Theory. The most critical assumption made in these calculations is that the amount of solute in solution at low RH is equivalent to that as the particle approaches activation. Although the RH scan data support this assumption, it is possible that additional mass dissolves as the RH approaches and exceeds 100%. For each bin in the size distribution, the critical supersaturation inferred from the hygroscopicity measurements was combined with the size-resolved concentration to calculate the corresponding value of the critical supersaturation distribution, $dN/d\log S_c$. *Covert et al.* [1998] employed a similar approach to predict critical supersaturation distributions based on size distributions and hygroscopic growth measured in Tasmania during the first Aerosol Characterization Experiment (ACE-1).

4.5 Results and discussion

4.5.1 Partitioned fractions

Figure 4.10 shows contour plots of the number ($dN/d\log D_p$) and corresponding volume size distributions ($dV/d\log D_p$) for the entire measurement period. This figure shows that the aged aerosol number distributions have a mode between 0.15 to 0.25 μm , while the volume distribution peaks between 0.3 and 0.4 μm . These number and volume size distributions of this aged biomass burning aerosol are

similar to those described by *Haywood et al.* [2003] and *Hand et al.* [2002]. The number concentration peaked between 9 and 10 May, while a shift in the size distribution towards greater particle size resulted in a peak in the volume concentration later in the study period, between 10 and 11 May.

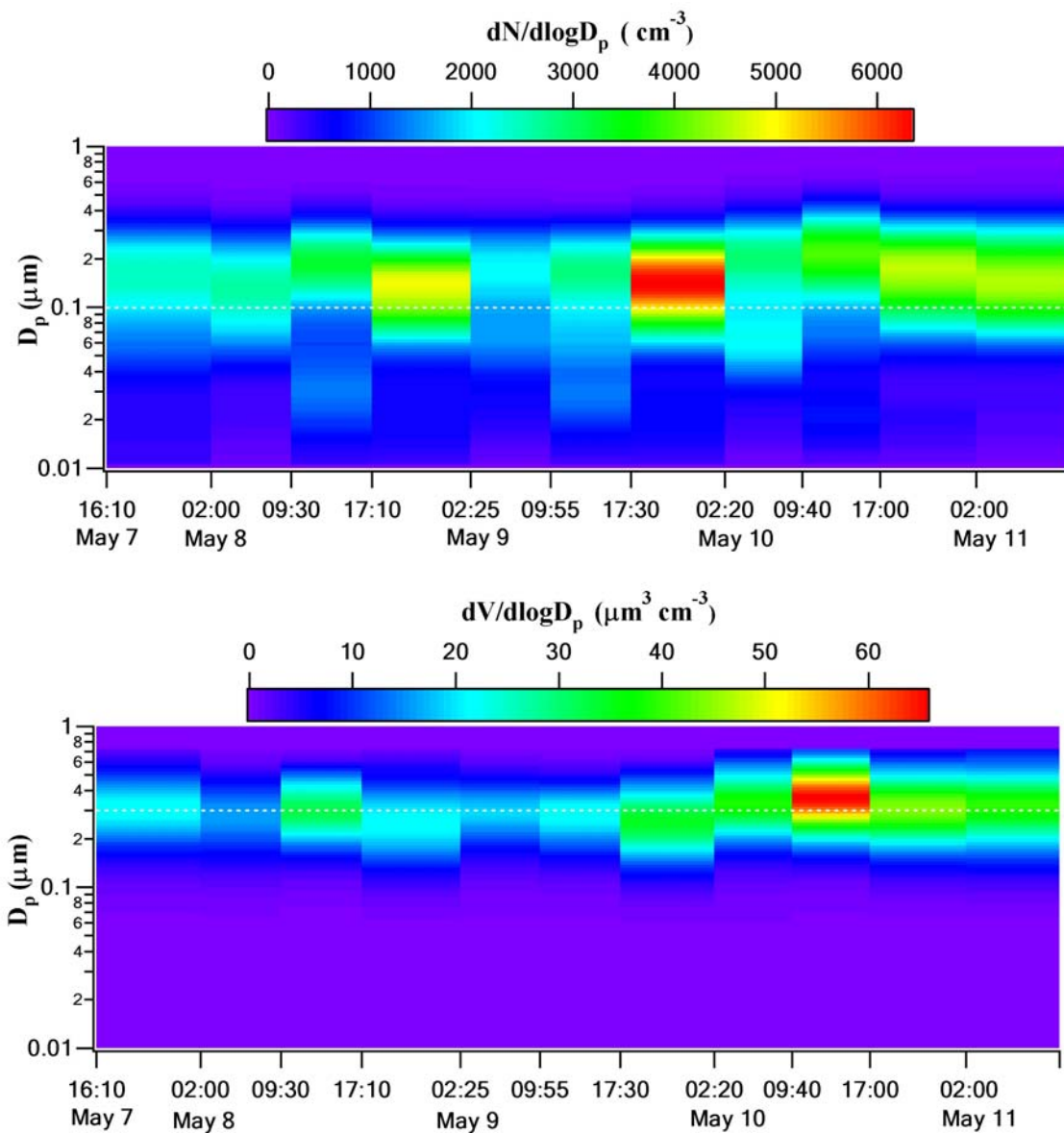


Figure 4.10. Number and volume distributions of the aerosol measured during the biomass burning aerosol event.

The hygroscopic growth contour plots shown in Figure 4.11 were created from the fixed-RH TDMA measurements at the seven dry diameters identified above. Three distinct hygroscopic growth modes were often observed in the growth factor distributions of the smaller particles characterized. The absence of more than two peaks in the growth factor distributions of the larger particles does not necessarily indicate that fewer particle types were present at larger particle size. Often, the overlap between the more concentrated biomass burning and sulfate modes obscured additional modes that were easily identified during the lognormal fitting process. The sparingly hygroscopic biomass burning particles represent the most concentrated particle type for diameters of 100 nm and greater. Total aerosol concentrations of the smallest (25 nm) and largest (600 nm) particles were substantially lower than those for the intermediate sizes. The reduced count rate during measurement of these tails of the size distribution often resulted in broadened distributions and increased noise.

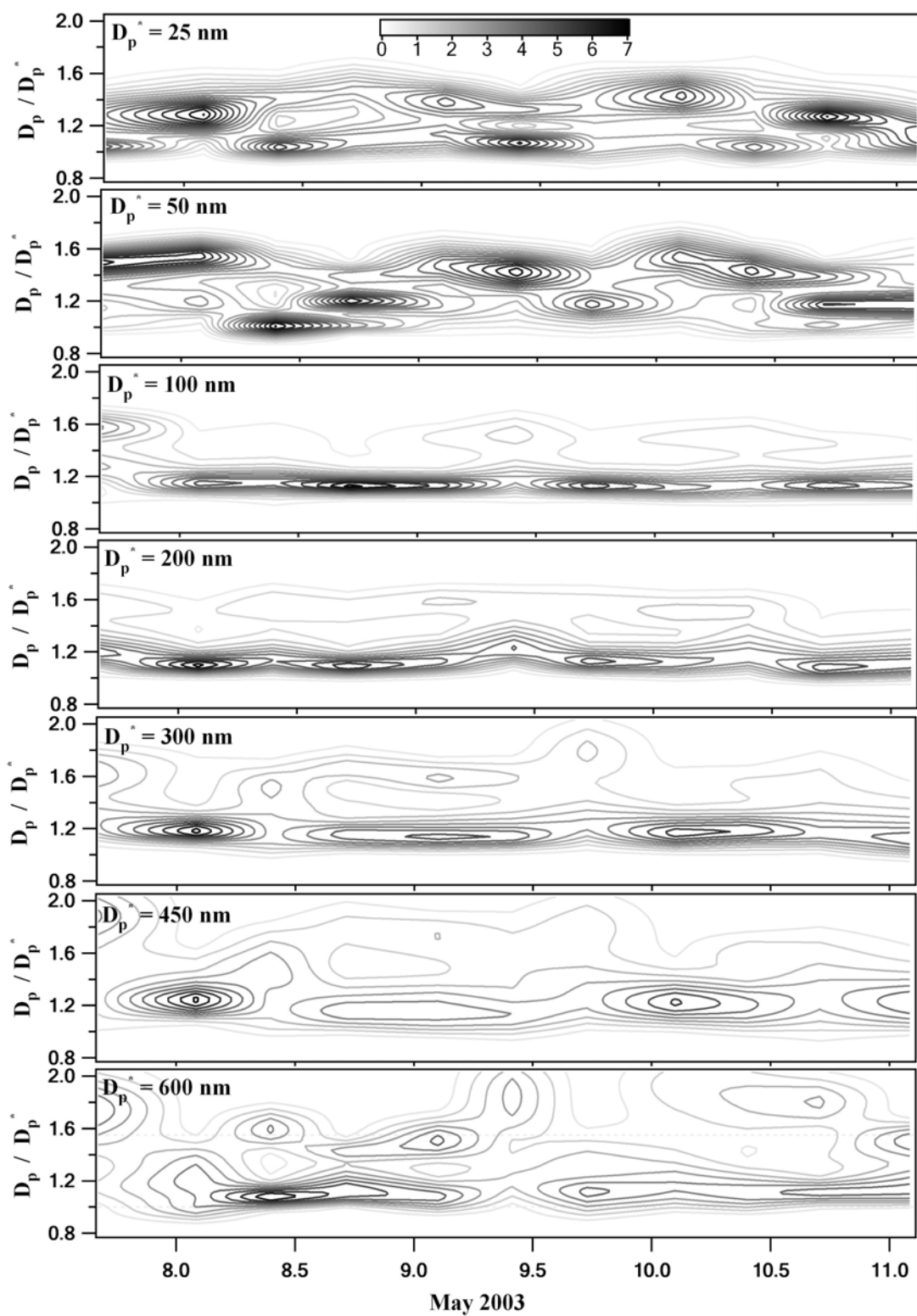


Figure 4.11. Measured hygroscopic growth factor distributions for particles with diameters between 25 and 600 nm.

Although not used directly in the computing the critical supersaturation distributions, the HS-TDMA and HT-TDMA measurements were the basis for the assumptions regarding the composition and behavior of each of the five particle types. Figures 4.12 to 4.14 show humidity scanning TDMA (HS-TDMA) measurements for dry aerosol diameters of 50, 100, and 200 nm. The position of each of the markers reflects the median hygroscopic growth measured, while the marker size reflects the relative concentration when more than one mode was observed. Separation between the hollow and solid markers would indicate that deliquescent particles were present. The absence of any clear separation suggests that most sulfate present in the aerosol is present either as ammonium bisulfate or sulfuric acid. In each of these graphs, the series of markers that terminate at a growth factor of about 1.1-1.2 at the maximum RH represent the biomass burning aerosol. The increased number of modes present at high RH reflects the increased ease with which adjacent modes can be discerned and not an increase in the number of particle types.

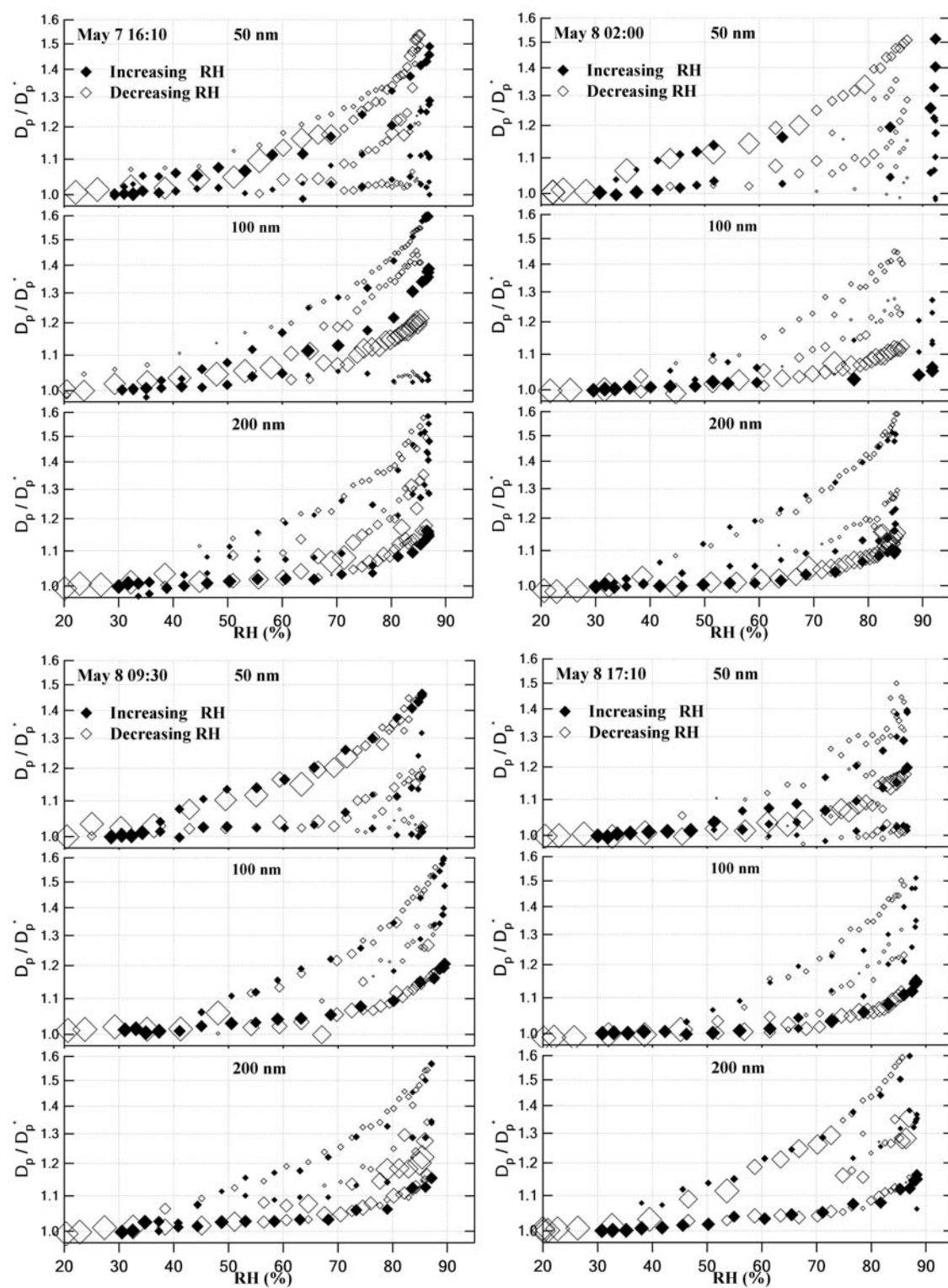


Figure 4.12. Plots of RH scan data from May 7 to 8, 2003 for 50, 100, 200 nm.

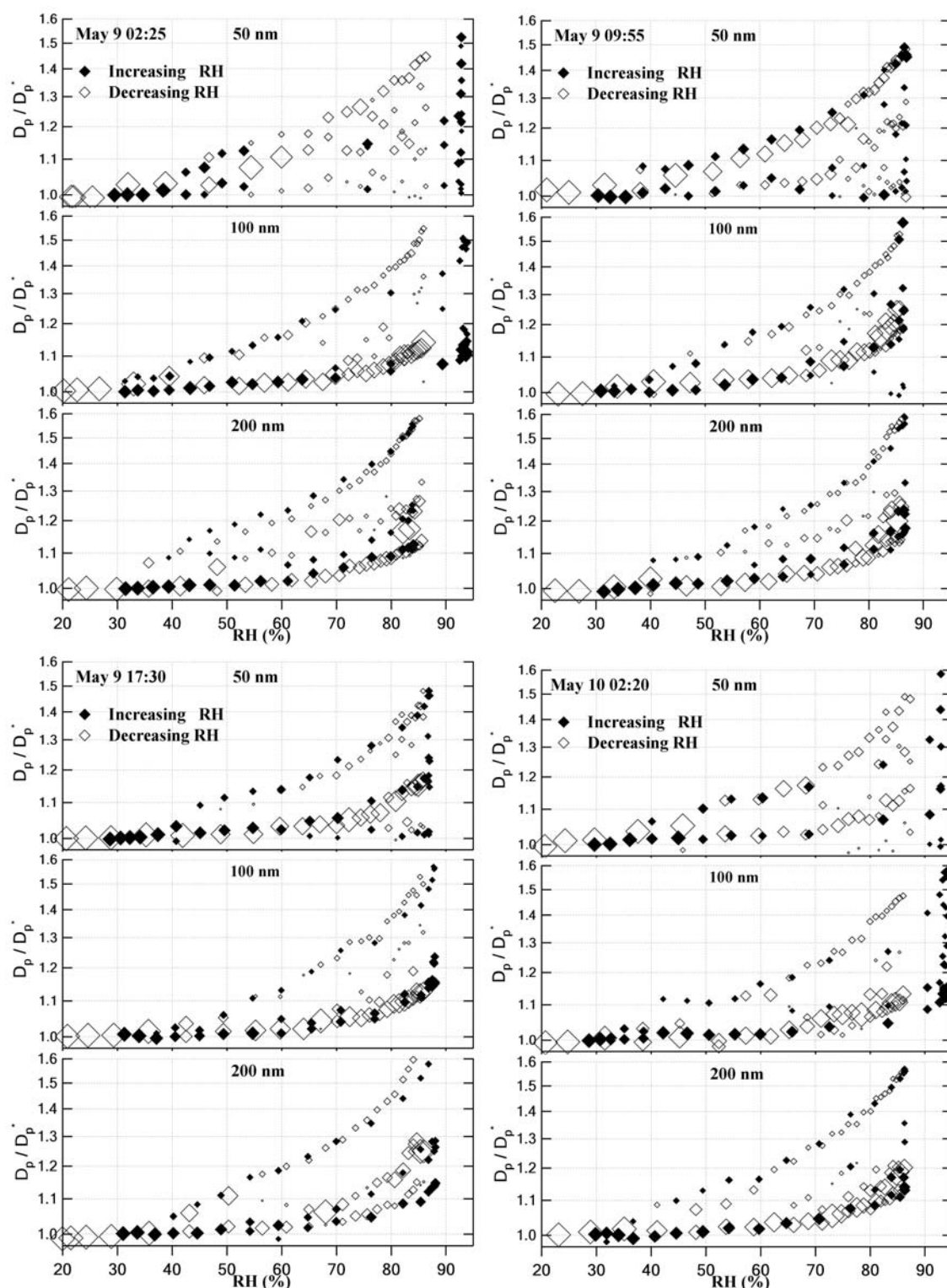


Figure 4.13. Plots of RH scan data from May 8 to 9, 2003 for 50, 100, 200 nm.

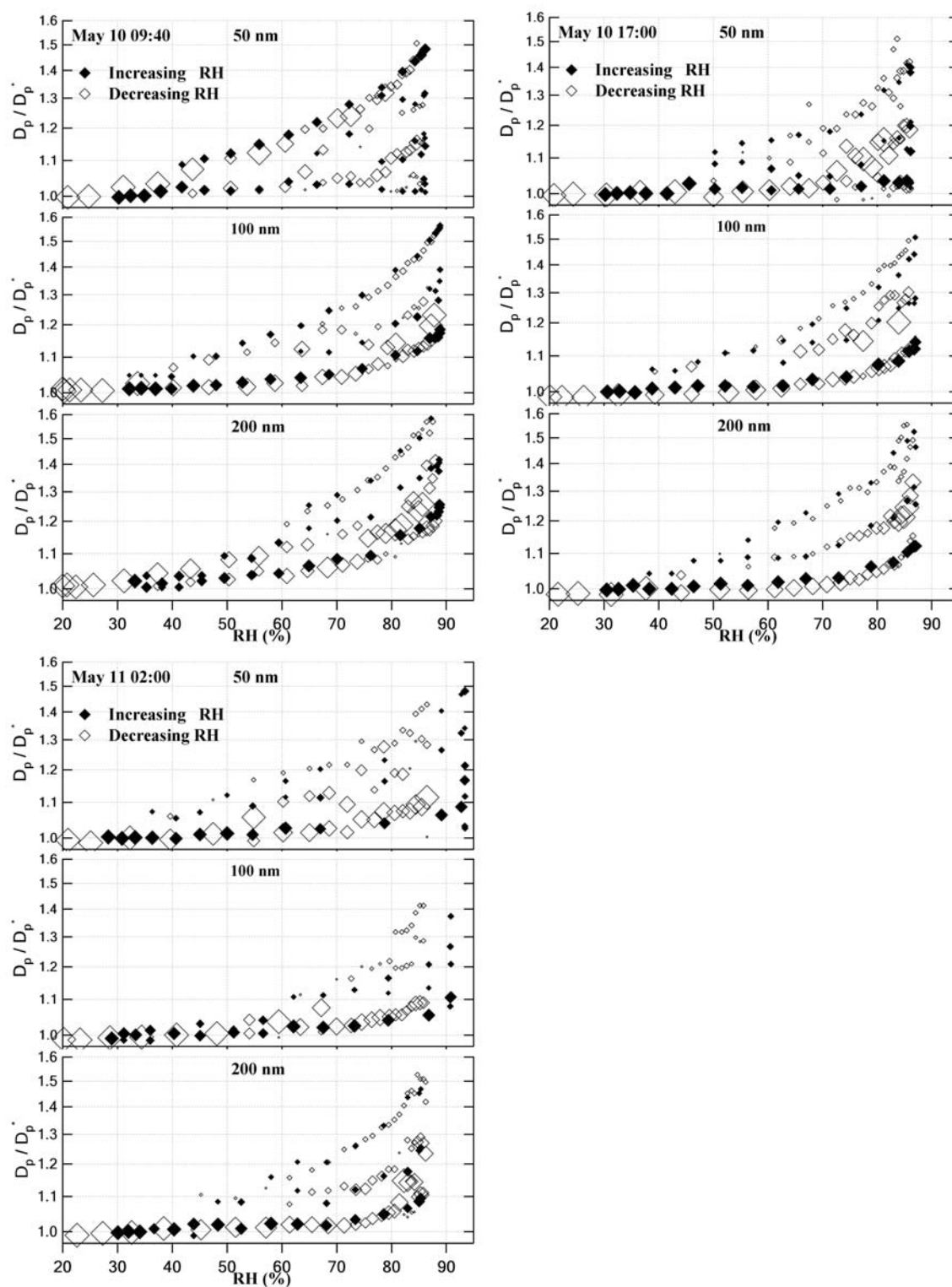


Figure 4.14. Plots of RH scan data from May 10 to 11, 2003 for 50, 100, 200 nm.

The HT-TDMA measurements of 50, 100, and 200 nm particles are shown in Figure 4.15. The similarity in hygroscopicity of a number of common inorganic aerosol types precludes direct identification of the aerosol composition from H-TDMA or even HS-TDMA measurements. The relationship between volatilization temperature and aerosol composition can be used to further constrain the aerosol composition to improve upon the accuracy of the final activation efficiency calculations. In contrast to inorganic particles that may contain one or two distinct compounds, organic aerosol consist of a wide range of species, each of which volatilizes at a slightly different temperature. The resulting HT-TDMA curve shows a gradual decrease in size with increasing temperature. Both ammonium sulfate and ammonium bisulfate volatilize over a relatively narrow temperature range near 200 °C. The substantial loss in particle volume at this volatility temperature will be reflected in a sharp change in particle size in the HT-TDMA data. Both organic dominated and inorganic dominated particle types are present in the HT-TDMA data shown in Figure 4.15, 4.16 and 4.17.

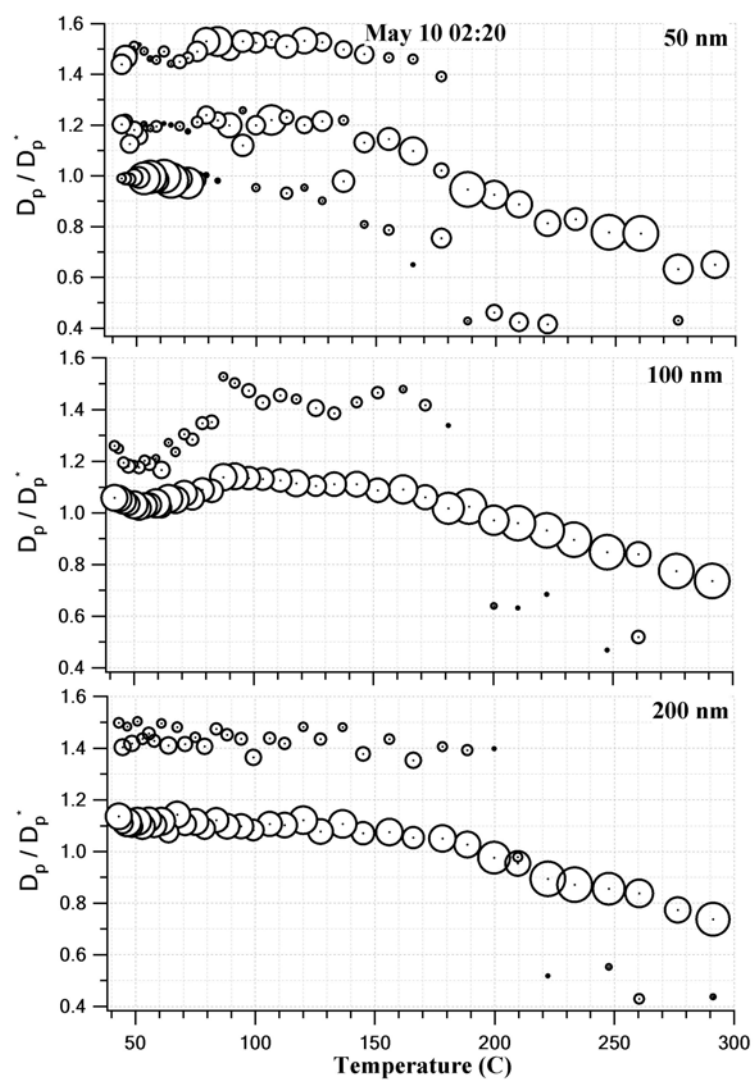


Figure 4.15. Plots of volatility scan data from 02:20 10 May 2003 for 50, 100, and 200 nm.

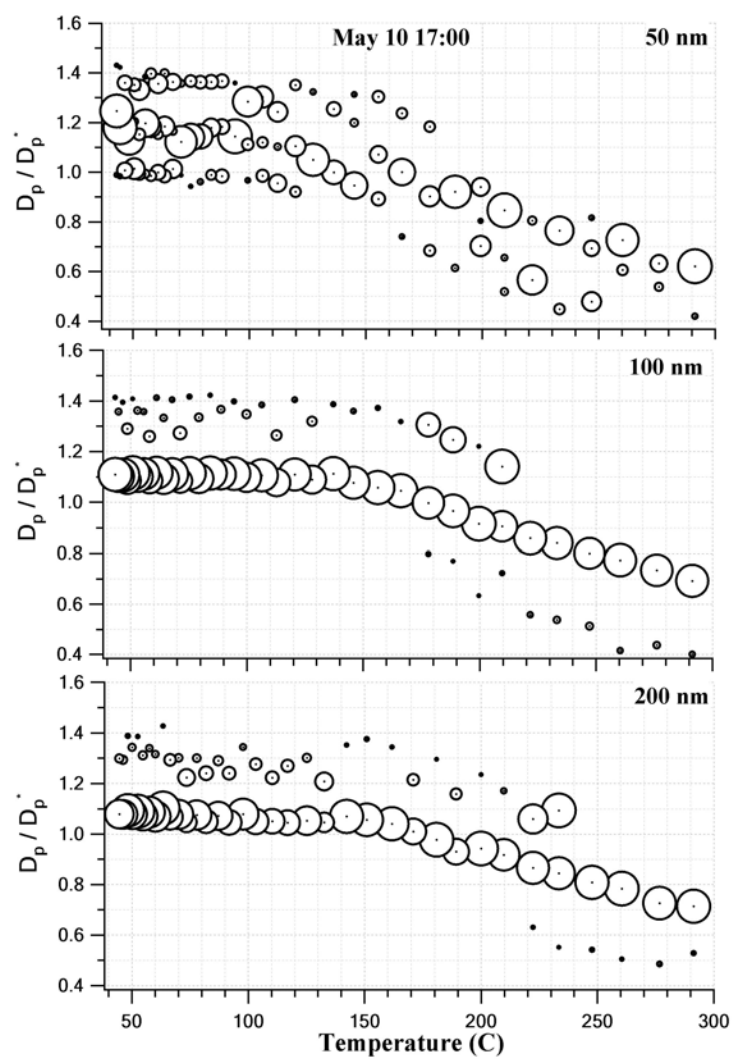


Figure 4.16. Plots of volatility scan data from 17:00 10 May 2003 for 50, 100, and 200 nm.

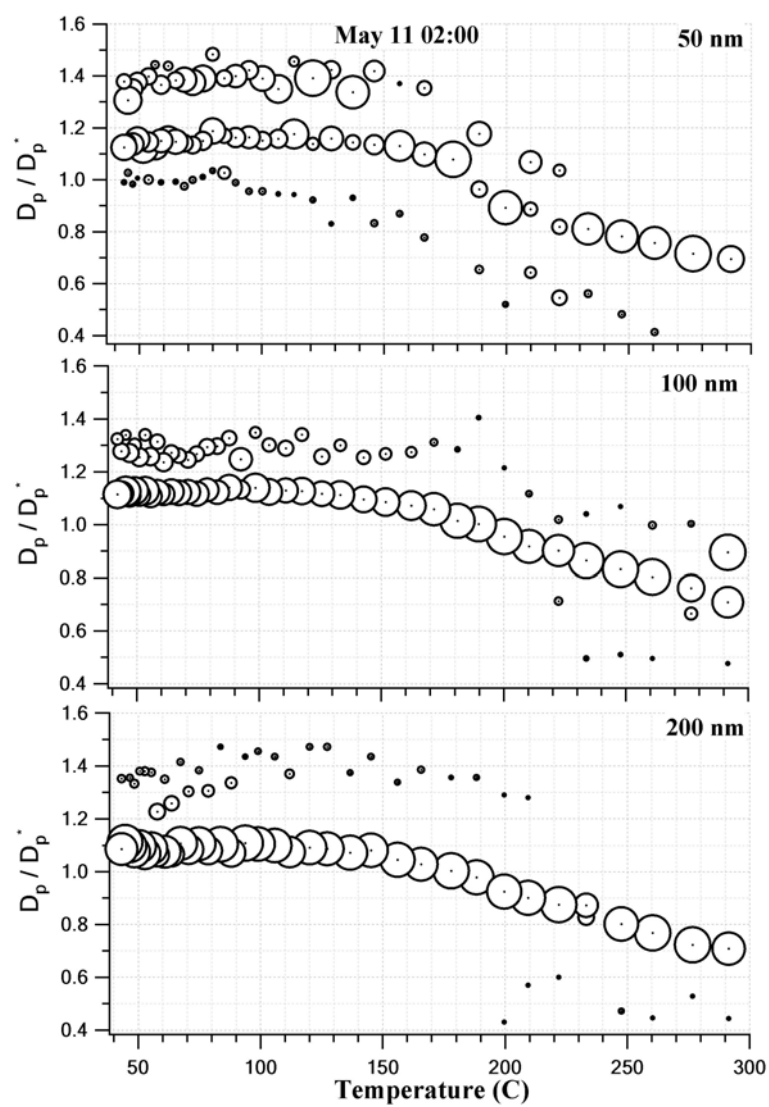


Figure 4.17. Plots of volatility scan data from 02:00 11 May 2003 for 50, 100, and 200 nm.

4.5.2 Partitioned size distribution

Size distributions for each of the five particle types identified in the hygroscopic growth measurements were determined for each of the measurement sequences completed during the sampling period. Contour plots showing the evolution of these distributions during the smoke episode are shown in Figure 4.18. Throughout the sampling period, the concentration of the biomass burning aerosol was significantly higher than that of any of the other particle types identified. The number concentration of the biomass burning aerosol ranged from 660 to 2130 cm^{-3} , with an average of 1300 cm^{-3} . The lack of a strong link between the concentration of the “local organic” particle type and the biomass burning class supports the conclusion that the two populations had different sources. In contrast, the concentration of the mixed organic / sulfate particle class seems to be correlated with that of the biomass burning aerosol. Although the origin of the mixed composition aerosol is unknown, its hygroscopic properties could be explained through either coagulation of biomass burning particles with sulfate particles or cloud processing of biomass burning particles. Neither of these possibilities can be verified or refuted with the available data. Table 4.2 contains the lognormal parameters for the size distributions determined for each of the particle types. Also included in the table is the soluble fraction for each of the particle types, which is calculated assuming the soluble component is ammonium bisulfate. This soluble fraction is used to determine the relationship between particle size and critical supersaturation, and is also used in the cloud model described below.

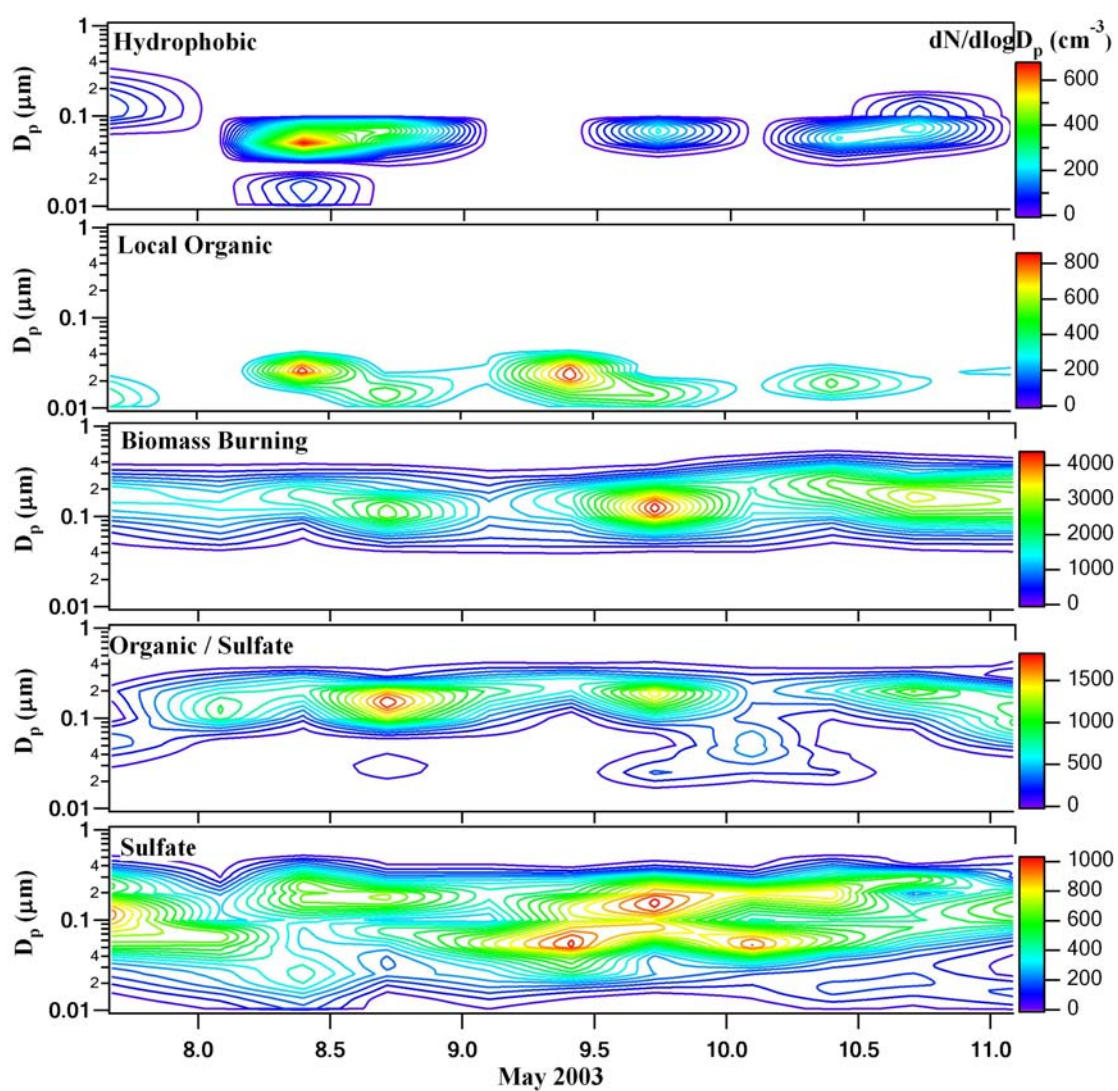


Figure 4.18. Partitioned size distributions during the measurement period.

Table 4.2. Aerosol size distribution parameters for the five aerosol types identified in the hygroscopic growth factor distributions.

Time/ Mode		Hydrophobic			Local Organic			Biomass Burning				Organic / Sulfate				Sulfate			
		N	D_{pg}	σ_g	N	D_{pg}	σ_g	N	D_{pg}	σ_g	S.F	N	D_{pg}	σ_g	S.F	N	D_{pg}	σ_g	S.F
May 7 16:10	1	59.3	0.14	1.56	124.6	0.01	1.34	652.7	0.14	1.64	0.27	39.1	0.03	1.49	0.61	701.5	0.10	2.07	1.00
	2				68.4	0.03	1.38	167.0	0.21	1.29		102.9	0.06	1.33		29.6	0.29	1.16	
8 02:00	1	4.4	0.06	1.29	30.6	0.02	1.36	154.6	0.07	1.38		232.6	0.11	1.34		235.1	0.04	1.92	
	2	0.6	0.53	1.11	1.5	0.04	1.15	745.9	0.14	1.64	0.29	220.8	0.19	1.40	0.43	157.2	0.07	1.35	0.94
	3															87.67	0.17	1.36	
8 09:30	1	37.6	0.01	1.30	291.9	0.03	1.40	887.7	0.16	1.53	0.12	196.7	0.15	1.46	0.35	319.2	0.03	2.01	0.82
	2	194.4	0.05	1.33								123.6	0.24	1.29		393.0	0.20	1.67	
8 17:10	1	116.6	0.06	1.31	82.5	0.01	1.24	1327.8	0.11	1.55		50.8	0.03	1.32		90.0	0.03	1.48	
	2				128.5	0.02	1.51	74.1	0.28	1.19	0.13	772.0	0.14	1.46	0.37	113.0	0.07	1.28	0.84
	3															273.4	0.18	1.42	
9 02:25	1				173.1	0.03	1.75	79.4	0.06	1.31		71.7	0.10	1.34		121.8	0.02	1.55	
	2							586.7	0.13	1.68	0.11	320.8	0.20	1.43	0.28	248.1	0.06	1.39	0.86
	3															190.2	0.19	1.50	
9 09:55	1				407.3	0.02	1.55	462.2	0.09	1.58		240.3	0.23	1.38		162.4	0.03	1.38	
	2							527.2	0.17	1.40	0.21				0.46	256.2	0.06	1.35	0.93
	3															416.3	0.13	1.68	
9 17:30	1	64.4	0.06	1.28	174.7	0.01	1.36	2133.9	0.13	1.57		96.1	0.03	1.35		75.1	0.03	1.34	
	2				19.8	0.03	1.20				0.20	569.6	0.17	1.45	0.42	252.0	0.07	1.40	0.94
	3															462.3	0.17	1.53	
10 02:20	1				83.5	0.02	1.42	828.2	0.12	1.73	0.20	269.3	0.05	1.67	0.58	409.3	0.06	1.51	0.99
	2				183.5	0.04	1.20	439.4	0.25	1.39		140.7	0.20	1.49		252.8	0.19	1.35	
10 09:40	1	69.5	0.06	1.33	206.8	0.02	1.50	1054.7	0.16	1.65		71.8	0.03	1.39		69.0	0.02	1.48	
	2							462.3	0.27	1.36	0.15	196.3	0.20	1.40	0.44	211.9	0.06	1.37	0.90
	3															406.5	0.19	1.57	
10 17:00	1	81.9	0.07	1.38	115.5	0.02	1.46	1869.7	0.15	1.68		398.6	0.18	1.43		52.8	0.02	1.38	
	2	12.2	0.14	1.17	7.8	0.04	1.14				0.21				0.46	307.5	0.10	1.77	0.89
	3															101.1	0.28	1.18	
11 02:00	1				84.1	0.03	1.34	1639.2	0.14	1.66		587.4	0.11	1.71		51.0	0.02	1.34	
	2							212.8	0.26	1.24	0.20				0.38	347.8	0.13	1.63	0.76
	3															12.1	0.42	1.19	

$N(cm^{-3})$: Aerosol number concentration. $D_{pg}(\mu m)$: Geometric mean diameter.

σ_g : Geometric standard deviation. S.F: mean Soluble mass Fraction.

4.5.3 CCN distributions

There is observational evidence that smoke aerosol from biomass burning increases CCN concentrations during the dry season in the Amazon Basin [*Roberts et al.*, 2003]. *Mayol-Bracero et al.* [2002] showed that biomass burning is a source of water-soluble organic components, and can contribute to CCN concentration. We assess the impact of the aged biomass burning aerosol and the other particle types observed on CCN spectra. Peak supersaturations in cloud typically range from between about 0.1 and 1.0%. The analysis here considers an even wider range between 0.01 and 10%. CCN spectra are typically presented as either differential or cumulative distributions. Differential distributions more closely reflect the aerosol size distribution and provide greater insight into the size-dependent composition, while cumulative distributions provide a convenient means for relating peak supersaturation in cloud with the corresponding cloud droplet concentration. Both types of data presentation are included in Figures 4.19 to 4.21 for each of the 11 measurement sets analyzed. The hygroscopic and soluble sulfate particles dominate the concentration at low critical supersaturation, while the biomass burning aerosol typically dominates at high critical supersaturation. Despite the fact that the biomass burning particles were relatively non-hygroscopic, almost all would activate in clouds having peak supersaturations of 1%. The overall CCN concentrations at 0.15%, 0.5%, and 1.0% throughout the smoke episode are shown in Figure 4.22. Average CCN concentrations were 869, 1918, and 2206 (cm^{-3}) at 0.15, 0.5, and 1.0% critical supersaturation, respectively. These concentrations are similar to those measured by *Roberts et al.* [2003] during the dry season in the Amazon Basin when smoke aerosol dramatically increased CCN concentrations.

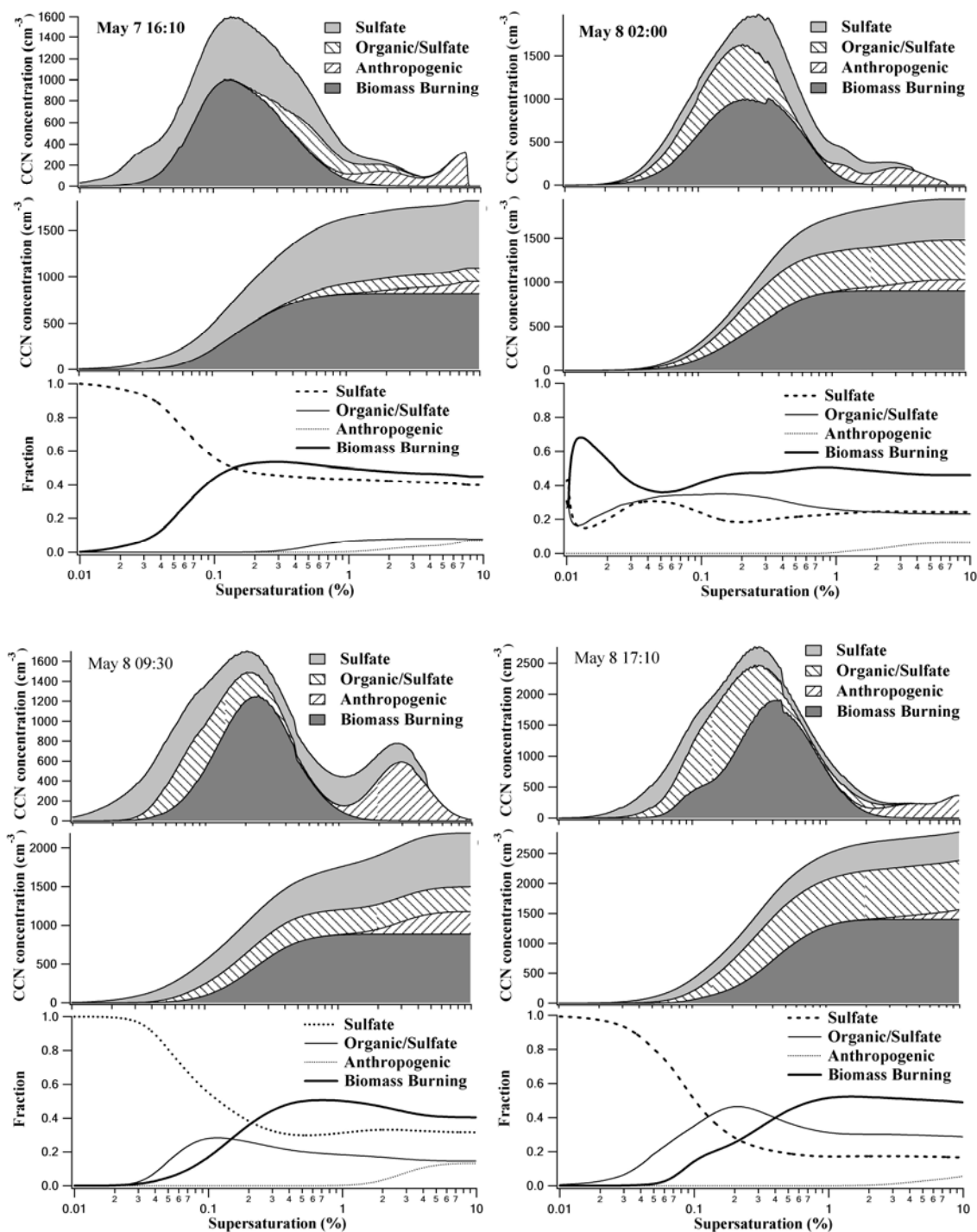


Figure 4.19. Differential (top) and cumulative (middle) CCN spectra for each of the measurement sequences completed between 7 and 8 May 2003. The bottom graphs show the fractional contribution of each of the aerosol types to the cumulative CCN concentration.

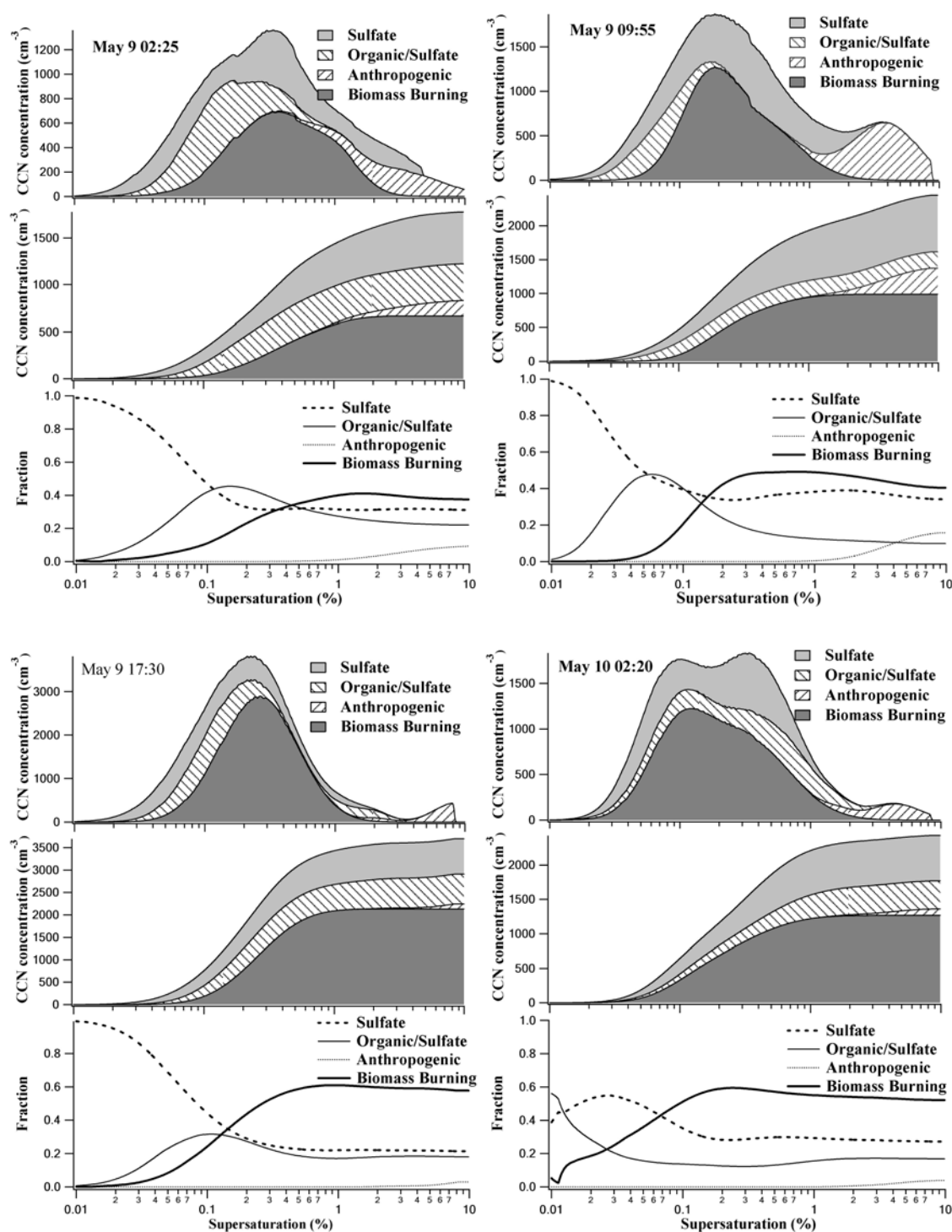


Figure 4.20. Differential (top) and cumulative (middle) CCN spectra for each of the measurement sequences completed between 9 and 10 May 2003. The bottom graphs show the fractional contribution of each of the aerosol types to the cumulative CCN concentration.

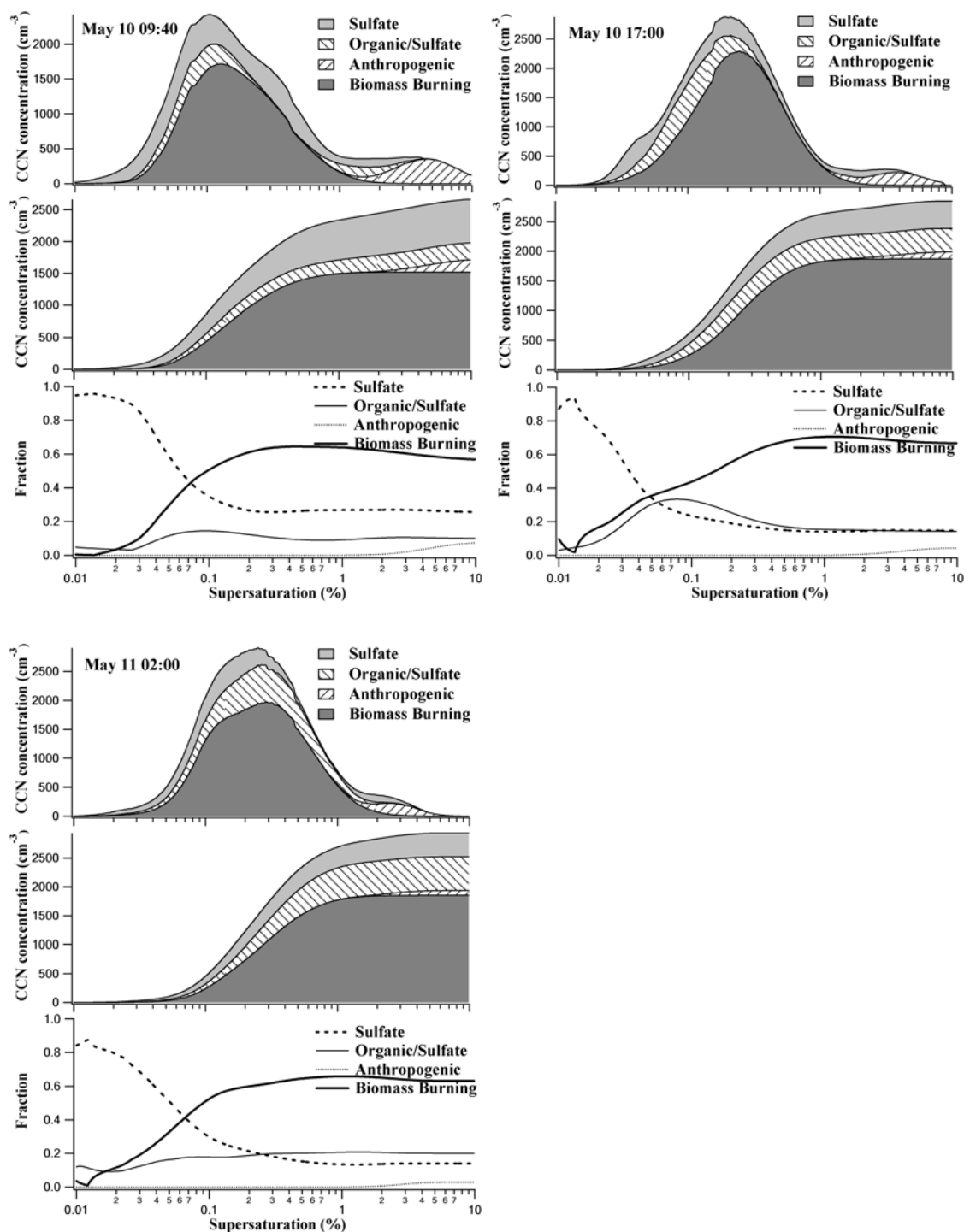


Figure 4.21. Differential (top) and cumulative (middle) CCN spectra for each of the measurement sequences completed between 10 and 11 May 2003. The bottom graphs show the fractional contribution of each of the aerosol types to the cumulative CCN concentration.

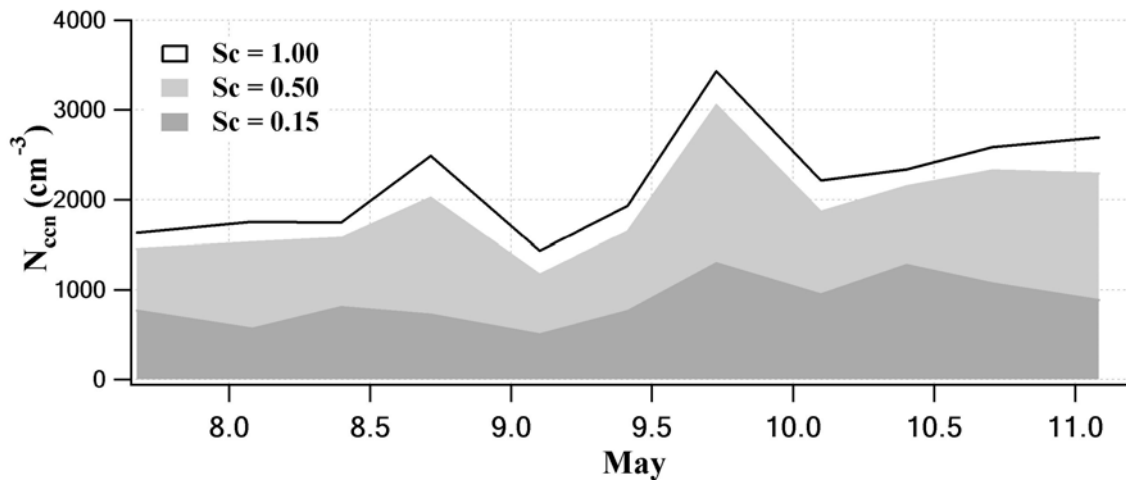


Figure 4.22. Total CCN concentrations $N(ccm^{-3})$ at different critical supersaturation.

Figure 4.23 and Table 4.3 show the CCN concentrations $N_{CCN}(cm^{-3})$ at 0.15, 0.5, 1 and 10 % critical supersaturation for biomass burning (B.B) and non-biomass burning (Non-B.B) contributions during the measurements. As shown in Figure 4.24, the fractional contribution of the biomass burning aerosol increases slightly with increasing critical supersaturation. The minimum fractional contribution at low critical supersaturation occurs during a time when the size distribution of the biomass burning aerosol shifted towards smaller diameter. The fractional contribution at high critical supersaturation is simply a reflection of the total number concentrations of each of the particle types since almost all particles will activate.

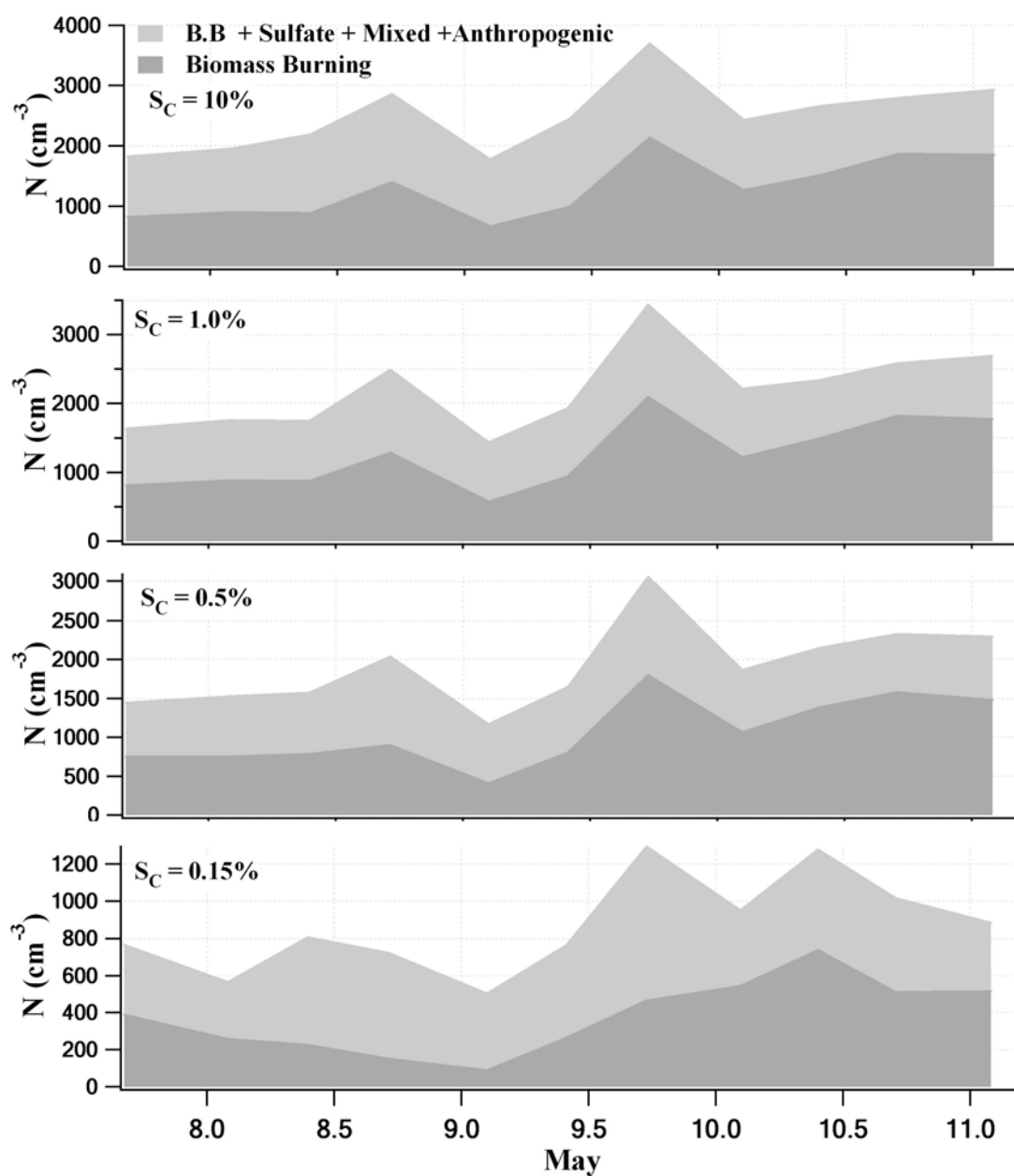


Figure 4.23. Time-dependent inferred total and biomass burning-only CCN concentration.

Table 4.3. CCN concentrations $N_{CCN} (cm^{-3})$ at different critical supersaturation. Values in parentheses represent the fractional contribution of the biomass burning aerosol to the total CCN concentration.

Time	$S_c = 0.15 \%$		$S_c = 0.5 \%$		$S_c = 1 \%$		$S_c = 10 \%$	
	B.B	Non-B.B	B.B	Non-B.B	B.B	Non-B.B	B.B	Non-B.B
May 7 16:10	390(.51)	377	755(.52)	692	812(.50)	823	820(.45)	1003
8 02:00	258(.46)	307	753(.49)	774	885(.50)	873	901(.46)	1056
8 09:30	226(.28)	580	786(.50)	787	876(.50)	872	888(.40)	1305
8 17:30	152(.21)	570	904(.44)	1134	1285(.52)	1206	1402(.49)	1459
9 02:25	90(.18)	414	412(.35)	758	575(.40)	861	666(.37)	1111
9 09:55	265(.35)	500	807(.49)	843	946(.49)	988	989(.40)	1460
9 17:30	466(.36)	831	1800(.59)	1259	2092(.61)	1342	2134(.58)	1563
10 02:20	544(.57)	408	1068(.57)	802	1219(.55)	996	1268(.52)	1164
10 09:40	738(.58)	541	1386(.64)	765	1495(.64)	843	1517(.57)	1148
10 17:00	511(.50)	507	1580(.68)	748	1824(.71)	761	1870(.67)	929
11 02:00	515(.58)	371	1482(.65)	813	1774(.66)	920	1852(.63)	1082
Average	378(.42)	491	1067(.54)	852	1253(.55)	953	1300(.50)	1207

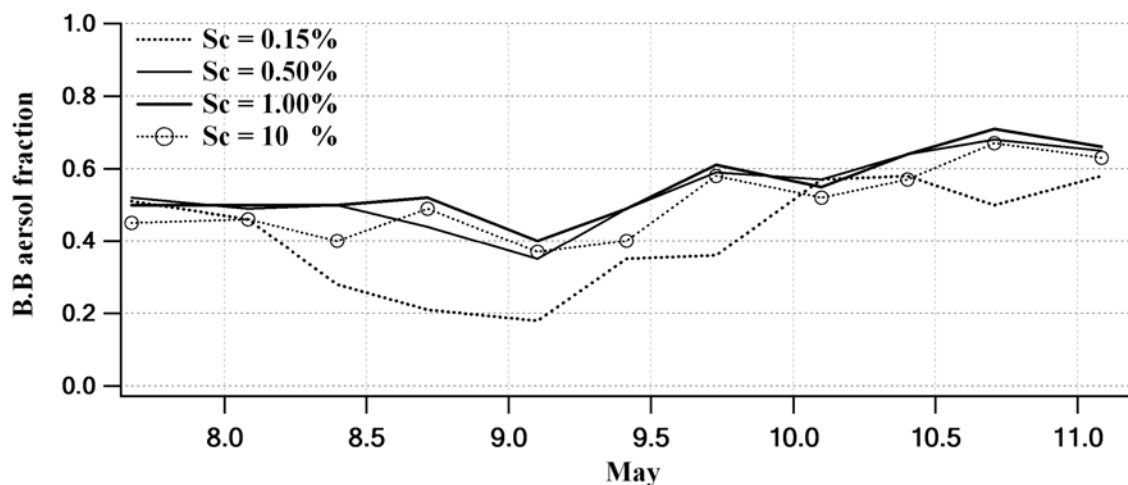


Figure 4.24. Biomass burning fractional contribution to the total CCN concentration as a function of critical supersaturation.

4.5.4 Parameterizations

Most regional or global models are designed to predict compositionally-resolved aerosol mass concentrations. Relating these mass concentrations to CCN concentrations

for evaluation of the influence of different emissions sources on cloud properties is challenging. To assist modeling efforts aimed at relating emissions from biomass burning to resulting CCN concentrations, the data described above were averaged to produce simple parameterizations relating CCN concentration to quantities more easily measured or modeled. Specifically, the critical supersaturation dependent CCN concentrations were normalized by the total number concentration, the total mass concentration, and the total scattering coefficient at 550 nm. For these calculations, the aerosol was assumed to have a density of 1.5 g/cm^3 , which is approximately half way between that observed by *Reid and Hobbs* [1998] and *Ross et al.* [1998] of 1.35 and 1.8 g/cm^3 , respectively. The refractive index of the aged biomass burning aerosol was assumed to be $1.54 - 0.018i$ [Haywood et al., 2003]. Figure 4.25 shows the number, mass, and scattering coefficient normalized CCN spectra. The solid line represents the mean, while the shaded area represents +/- one standard deviation.

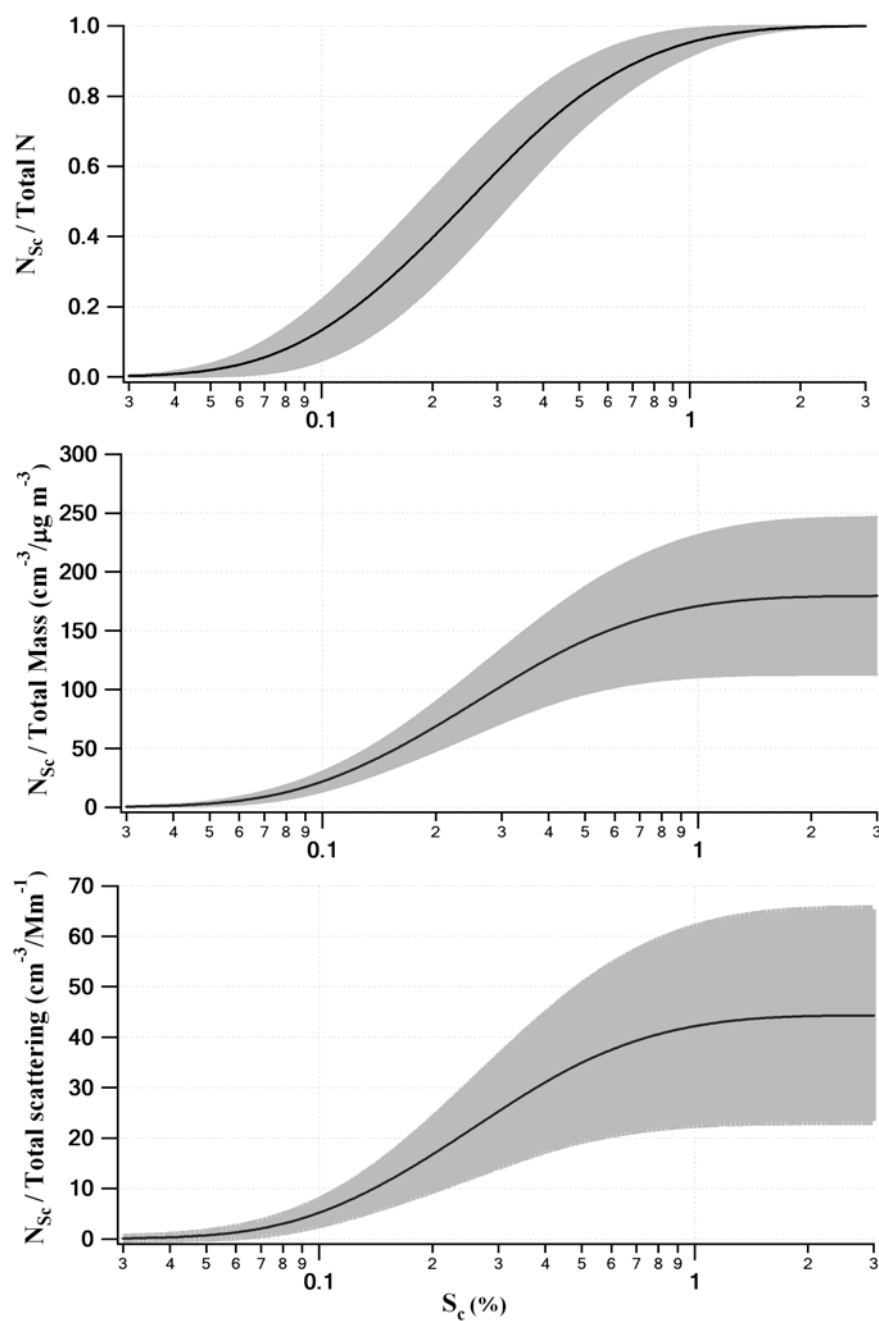


Figure 4.25. CCN spectra normalized by aerosol number concentration (top), mass concentration (middle), and scattering coefficient (bottom). The solid line represents the mean value and the shaded area bounds \pm one standard deviation.

4.5.5 Impact of biomass burning on cloud droplet concentrations

To evaluate the relationship between aerosol concentration and resulting cloud droplet concentration, it is often assumed that peak supersaturation in cloud is constant. While this approach may suffice when perturbations to the aerosol concentration are small, it may lead to significant error when there is considerable spread in the critical supersaturation distribution. By activating near cloud base, low critical supersaturation particles will deplete the water vapor concentration and will lower the resulting peak supersaturation. In some scenarios, it is possible to reduce cloud droplet concentrations by introducing particles with very low critical supersaturations. This type of perturbation is done intentionally during hygroscopic seeding of clouds, which is aimed at reducing cloud droplet concentrations to enhance coalescence efficiency, and ultimately, precipitation efficiency. Supermicron sodium chloride particles are typically used in hygroscopic seeding operations. The data described above were used in a cloud parcel model both to evaluate the overall activation efficiency of the biomass burning aerosol in different cloud types, and to determine whether the addition of hygroscopic sulfate particles might suppress activation of a significant fraction of the biomass burning aerosol, and thereby result in a decreased cloud droplet concentration. Dr. Graham Feingold of the NOAA Environmental Technology Laboratory developed and ran the model used for this analysis. The model results for all 11 measurement sets are shown in Figure 4.26. As expected, increasing updraft velocity results in increasing cloud droplet concentrations. For the majority of cases considered, the addition of the sulfate aerosol population resulted in an increase in cloud droplet concentration.

However, for both 0.1 and 0.2 m s⁻¹ updraft velocities, there were cases for which the sulfate aerosol introduction caused a reduction in cloud droplet concentration. These cases are reflected in Figure 4.27, which shows the ratio of the cloud droplet concentration resulting when both the biomass burning aerosol and the sulfate aerosol are included in the model to that when only the biomass burning aerosol is included. Values less than 1.0 correspond to a sort of natural hygroscopic seeding of the clouds. Regardless of whether the added sulfate increases or decreases cloud droplet concentrations, it will also prevent activation of some subset of the biomass burning aerosol. By reducing the rainout efficiency of the biomass burning aerosol, the added pollution aerosol may enhance its integrated direct radiative impact.

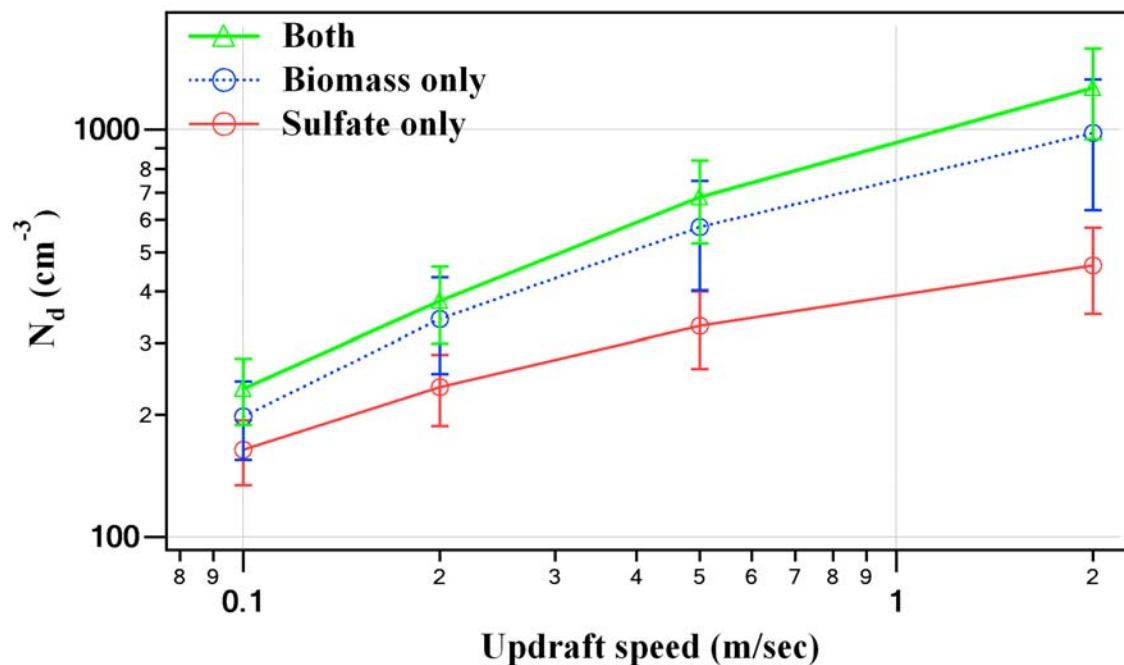


Figure 4.26. Cloud droplet number concentration as a function of updraft speed.

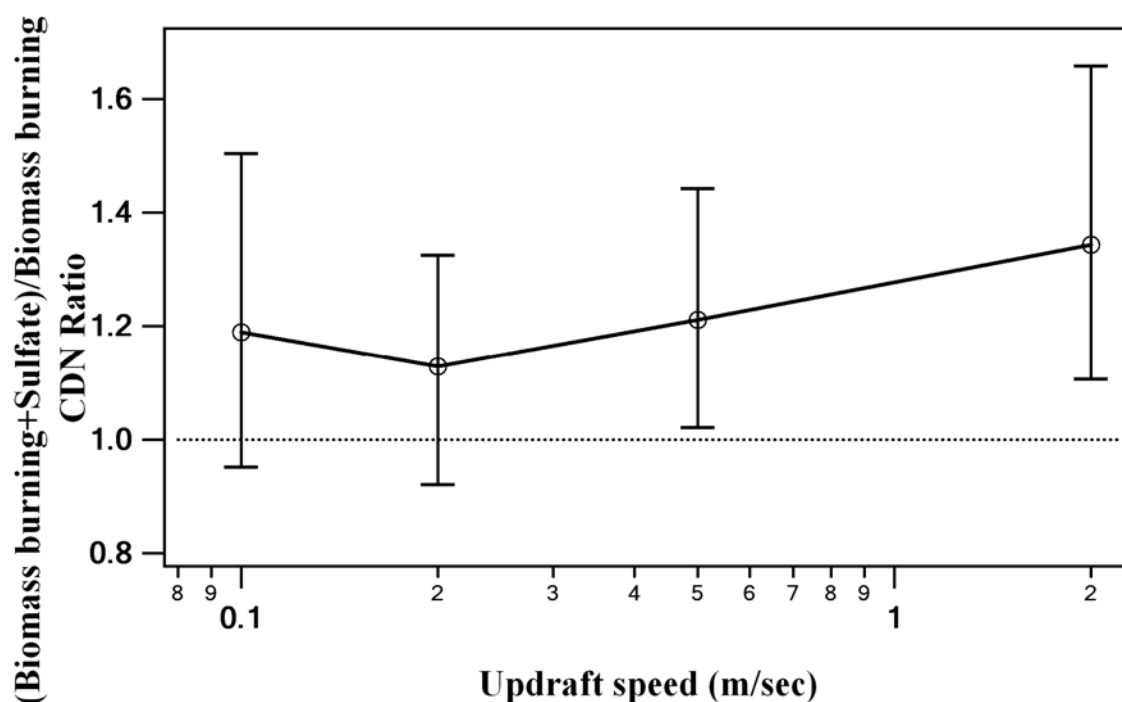


Figure 4.27. Ratio of cloud drop number concentration calculated when both the biomass burning and sulfate aerosol entered the modeled cloud to that when only the biomass burning aerosol entered.

4.6 Summary and conclusions

Aerosol size distributions and size-resolved hygroscopicity and volatility were measured over a four-day period in College Station, TX during a period when smoke from fires on the Yucatan Peninsula was transported across the Gulf of Mexico into Texas. Growth factor distributions were fitted with between one and four lognormals to identify distinct particle types. The fractional categorization based on the hygroscopicity measurements was coupled with measured size distributions to create independent size distributions for the biomass burning aerosol and each of the other particle types. The size distributions and representative hygroscopic properties of each of the particle types were then used to infer critical supersaturation distributions. This approach permits

examination of the activation properties of the biomass burning aerosol even when other aerosol types are present at high concentrations. The average inferred CCN concentrations were 869, 1918, and 2206 (cm^{-3}) at 0.15, 0.5, and 1.0% critical supersaturations, respectively. The impact of the biomass burning aerosol on cloud droplet concentrations was evaluated through a cloud parcel model. For certain aerosol measurements and cloud updraft velocities, predicted cloud droplet concentrations were lower when the observed sulfate aerosol was considered together with the biomass burning aerosol relative to that when only the biomass burning aerosol was considered. By suppressing activation of the less hygroscopic biomass burning particles, pollution aerosols may actually help preserve the smoke aerosol by reducing wet deposition rates. Furthermore, this represents a scenario in which pollution aerosol may cause a slight reduction in cloud albedo.

CHAPTER V

INVESTIGATION OF THE OPTICAL PROPERTIES OF AN AGED BIOMASS BURNING AEROSOL

During May of 2003, smoke from fires in the Yucatan Peninsula was transported across the Gulf of Mexico and into Texas where it caused significant enhancement in measured aerosol concentrations and reduced visibility. During this event, a differential mobility analyzer (DMA) / tandem differential mobility analyzer (TDMA) system was used to characterize the size distribution and size-resolved hygroscopicity and volatility of the aerosol. The hygroscopicity data were used to separate the sparingly hygroscopic biomass burning particles from other aerosol types. By coupling the size-resolved fraction of particles attributed to the fires with the overall size distribution, it was possible to construct a biomass burning aerosol-only size distribution. This distribution, and the aerosol properties derived from the TDMA data, were used to calculate the mass extinction efficiency and the humidity-dependent aerosol extinction coefficient (b_{ext}) and extinction-to-backscattering lidar ratio (S) for the biomass burning aerosol.

5.1 Introduction

Biomass burning aerosols can have significant impacts on local, regional, and even global radiative budgets. Despite a number of studies directed at quantifying the impact of biomass burning aerosols, there is still considerable uncertainty regarding the radiative forcing associated with increasing concentrations [IPCC, 2001]. The relative

abundance of light absorbing black carbon and non-absorbing organic carbon in a biomass burning aerosol will control the sign of its radiative impact, while both the composition and concentration will control the magnitude. *Haywood et al.* [2003] investigated the physical and optical properties of regional haze dominated by biomass burning aerosol. They determined the optical properties of the smoke using measured size distributions and refractive indices based on measured composition. However, they neglected the effects of relative humidity on scattering. *Colarco et al.* [2004] measured the smoke transported from Canadian forest fires to the surface near Washington, D.C. They examined the spatial distribution of the aerosol using the Total Ozone Mapping Spectrometer (TOMS) aerosol index and by computing trajectories for air parcels initialized in the source area.

A number of recent studies have examined the impact of seasonal biomass burning in the Yucatan Peninsula region of Central America. *Kreidenweis et al.* [2001] examined chemical and radiative characteristics of the smoke transported from fires in Mexico and Central America into the United States during fires in 1998. *Rogers and Bowman* [2001] studied the transport of smoke from those fires to the continental United States. *Hand et al.* [2002] used measured aerosol size distributions to estimate the impact of the smoke on visibility during the Big Bend regional aerosol and visibility observation study (BRAVO). They found that the highest organic carbon concentrations were observed during the spring time when the region was influenced by the fires in the Yucatan. The aim of this study is to determine the aerosol light extinction properties of

biomass burning aerosols transported to the U.S. from the Yucatan Peninsula during a period when there were widespread fires in that region in May of 2003.

5.2 2003 May smoke event

Intentionally set fires in agricultural regions on and near the Yucatan Peninsula generate elevated concentrations of particulates that impact aerosol loadings in the U.S. every spring. The severity of these episodes varies widely depending on the rainfall received preceding the burning season and the meteorology that is responsible for the transport to the U.S. Biomass burning aerosol loadings in Texas during May of 2003 were significantly higher than during the previous four years. Our group took advantage of this unique opportunity to measure the concentration and properties of this aged aerosol in College Station, Texas. Figure 5.1 shows the location of College Station (Texas A&M University) along with additional sites at which particulate matter measurements were made during the smoke episode. Additional data were recorded by the Texas Commission on Environmental Quality (TCEQ) at several sites throughout Texas, and at the Interagency Monitoring of Protected Visual Environments (IMPROVE) network sites at Big Band National Park (BBNP) and Wichita Mountains (WM). Although aerosol composition was not directly measured in College Station, the range of measurements made with our TDMA system was sufficient to permit examination of many of the important properties of the biomass burning aerosol. Our group made detailed aerosol measurements only in College Station.

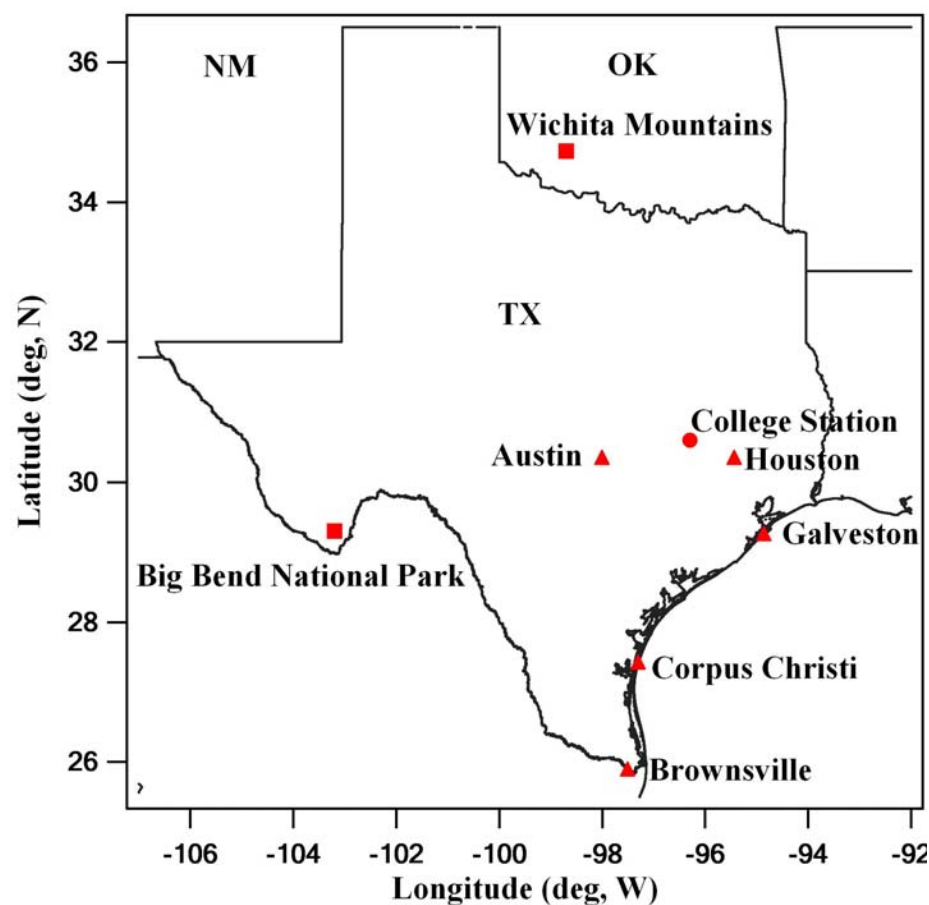


Figure 5.1. Locations of measurement sites (Circle: Texas A&M University, triangle: TCEQ, square: IMPROVE).

To examine how representative those measurements were of the impacted region, meteorological and air quality data collected by a number of agencies have been considered. Calculated backtrajectories and TOMS satellite data were used to connect the elevated aerosol loadings observed in Texas and nearby states to the regions impacted by burning, while the TOMS data were combined with surface measurements of aerosol mass concentration and aerosol optical properties to evaluate the spatial extent

of the event. We calculated 3-day back trajectories ending in College Station, Texas during the episode for four different levels from 990 to 910 hPa using the National Centers for Environmental Prediction (NCEP) reanalysis data. All of these trajectories confirmed that air was transported from the Yucatan to Texas. Figure 5.2 shows two examples (7 and 10 of May 2003) of back trajectories, with both sets originating in the region influenced by biomass burning. Figure 5.3 shows the TOMS aerosol index for two selected times during the measurement period. The first image on 7 of May shows elevated absorbing aerosol concentrations in a swath connecting the Yucatan and southeast Texas with a maximum index of 2.4. The 10 May image shows even higher aerosol loadings apparently originating near the same location in the Yucatan with a maximum index of 2.8. Unfortunately, gaps in the TOMS coverage during this time made it difficult to identify the entire smoke plume.

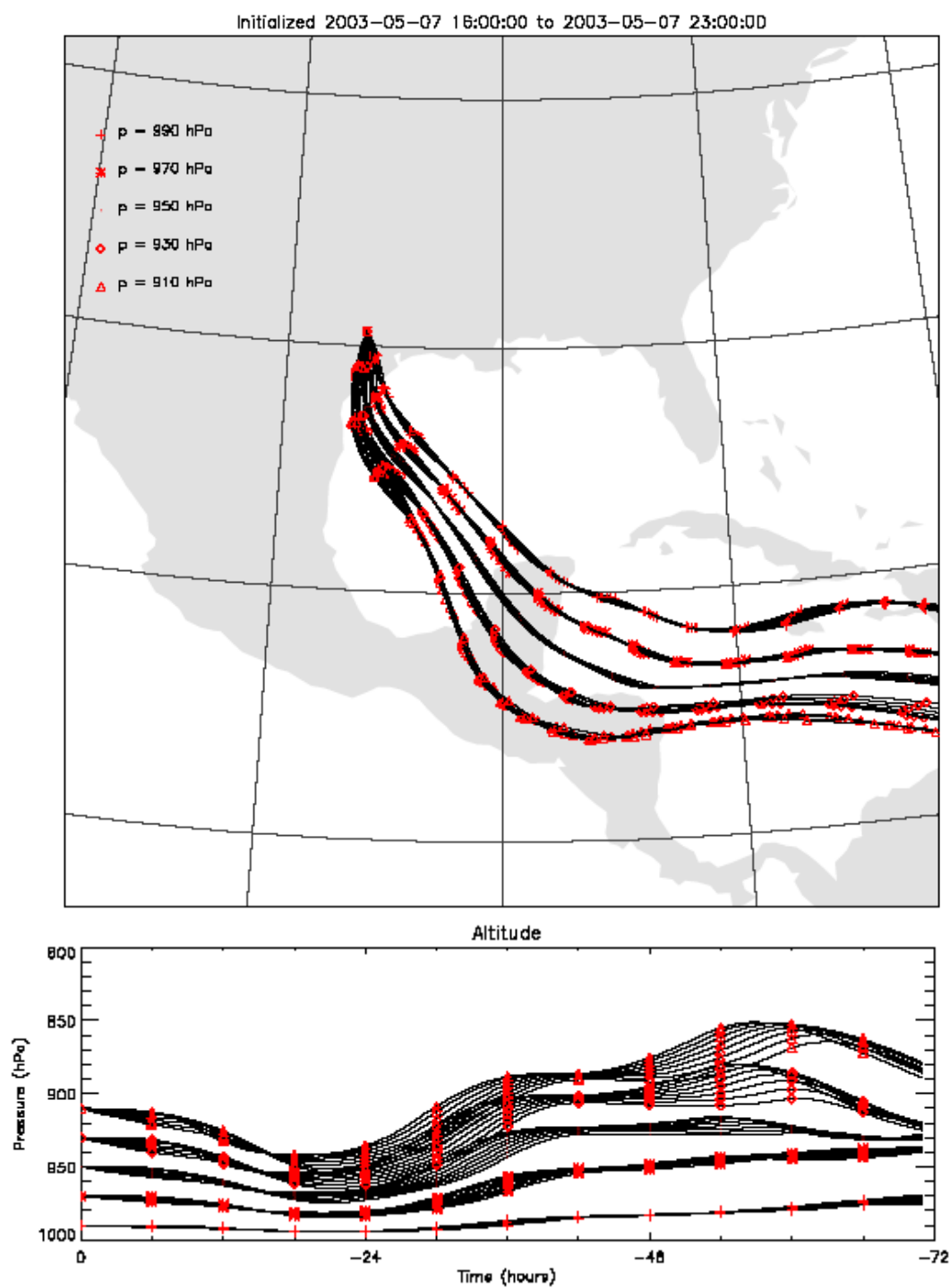


Figure 5.2a. Example back trajectories ending in College Station, Texas on 7 May 2003.

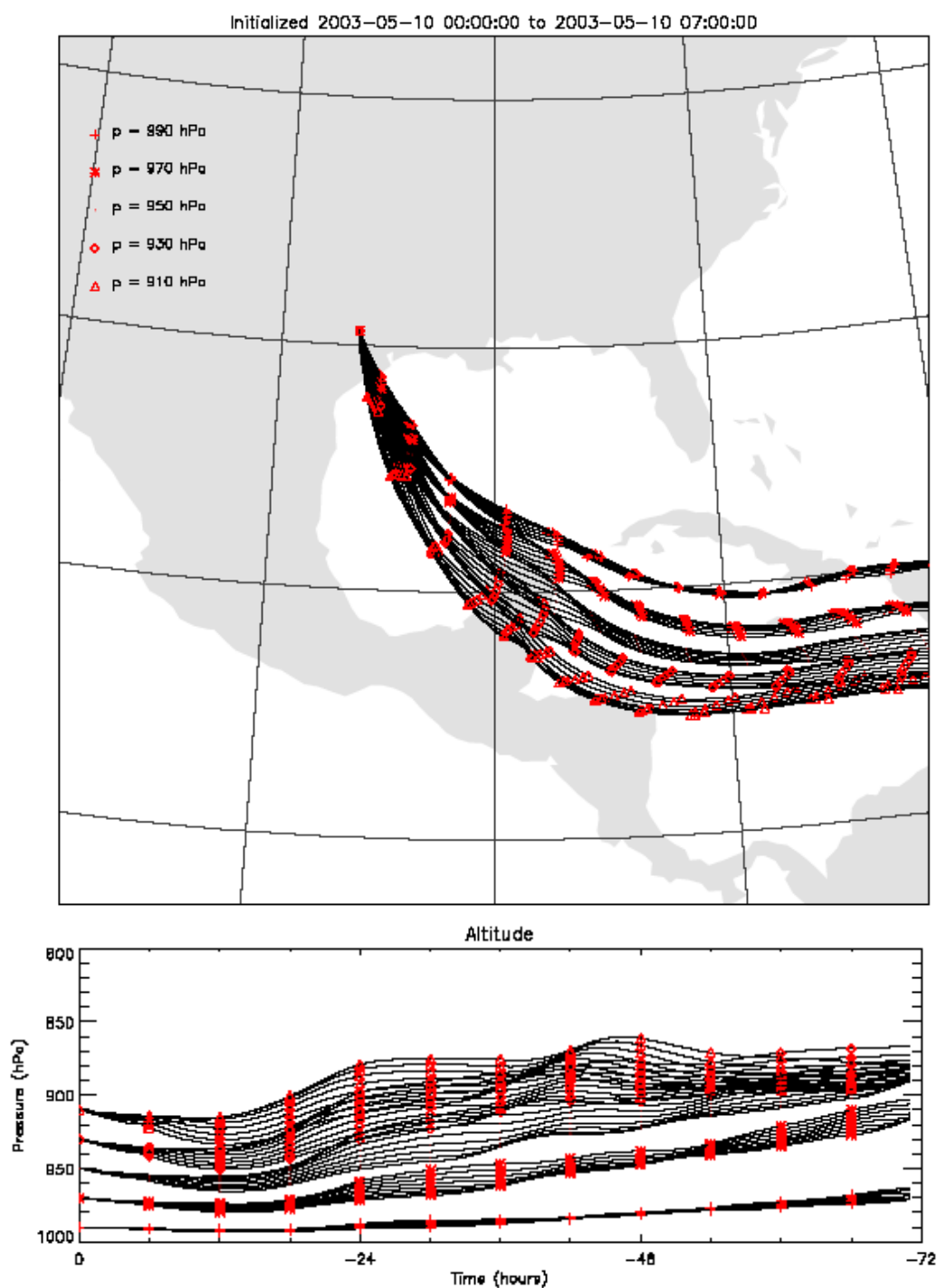


Figure 5.2b. Example back trajectories ending in College Station, Texas on 10 May 2003.

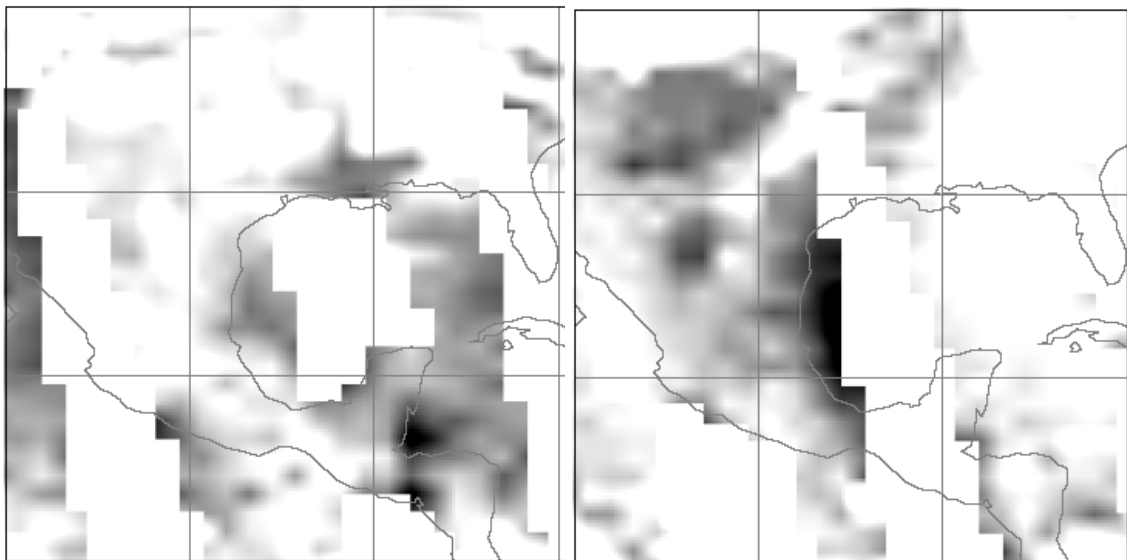


Figure 5.3. Earth Probe GRID TOMS Aerosol index on 7 (left) and 10 May 2003 (right). Index maxima and minima for the two days are 2.4 and -2.5, and 2.8 and -2.1, respectively.

IMPROVE is a monitoring program designed to protect visibility in 156 specific areas of concern, referred to as Class I areas. Of these Class I areas, two are considered here due to their relative proximity to College Station. Figure 5.4 shows the calculated aerosol extinction coefficients at Big Bend National Park, Texas (BBNP) and Wichita Mountains, Oklahoma (WM) during April and May of 2003. Sulfates, nitrates, organic carbon, elemental carbon, soil mass, and coarse mass concentration measured at these sites are used to calculate the aerosol type-specific extinction coefficients. This figure shows both the total extinction coefficient and the contribution to this total by organic carbon (OC) and black carbon (BC). Carbonaceous particles are focused upon here due to their abundance in biomass burning aerosol. The BC contribution is relatively small for all days but it is slightly elevated during the smoke episode. OC concentrations at both locations increase more significantly.

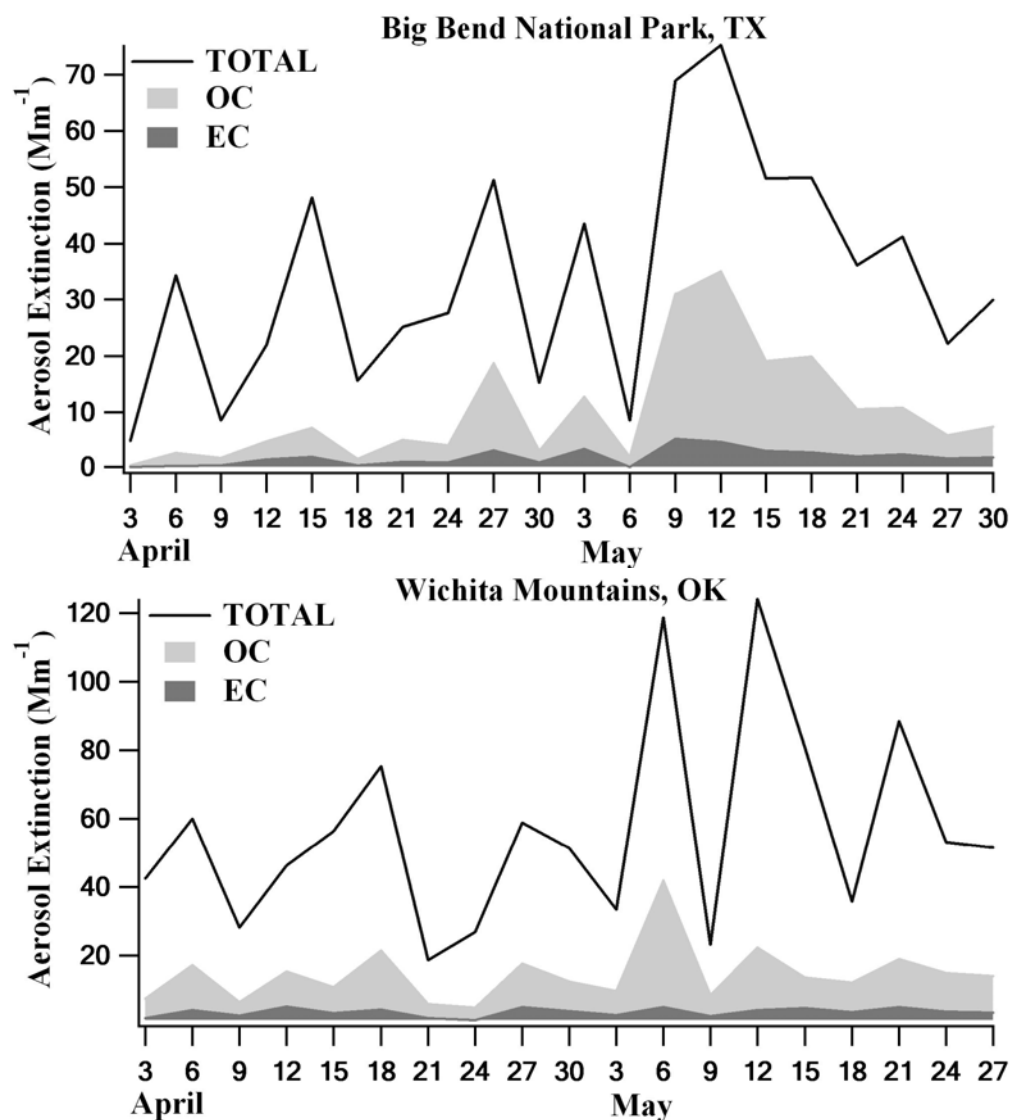


Figure 5.4. Aerosol extinction coefficients calculated from compositionally-resolved aerosol mass concentration at Big Bend National Park and Wichita Mountains during April-May 2003.

Aerosol size distributions and hygroscopic growth factors were measured in College Station, TX between May 7 and 11, 2003 during the biomass burning episode. Elevated aerosol concentrations were observed from May 6 through May 11 throughout much of Texas from the southernmost tip in Brownsville north through Corpus Christi,

Austin, and Dallas. Based on the calculated trajectories and satellite retrievals described above, biomass burning aerosols were transported from Mexico and adjacent countries in the Yucatan Peninsula area. The episode ended on May 11 as a cold front passed through the region, reversing wind direction and enhancing vertical transport of the pollutants. Figure 5.5 shows traces of visibility and relative humidity recorded at Easterwood Airport in College Station. The rapid increase in visibility on May 11 marks the passage of the cold front discussed above. Measurements of PM_{2.5} mass concentration do not provide the compositional detail necessary to identify compounds associated with smoke. To roughly identify the enhancement due to smoke in 2003, the measured PM_{2.5} concentration is compared with the average PM_{2.5} measured over the same period of time in 2002. Comparisons of this type for Galveston and Houston are shown in Figure 5.6. The observed enhancement of almost a factor of six in already polluted areas such as Houston suggests the smoke contributed to a substantial fraction of the overall concentration.

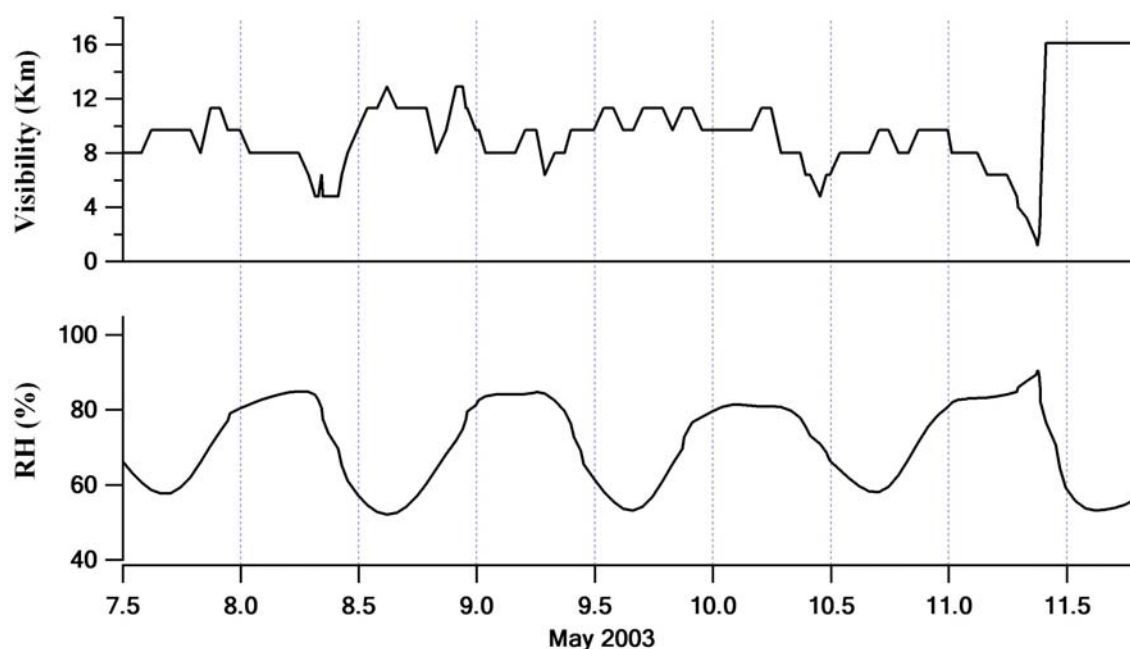


Figure 5.5. Time series of visibility and relative humidity recorded at Easterwood airport in College Station. Along the x-axis, 9.0 corresponds to midnight on May 9, and 9.5 corresponds to noon on May 9.

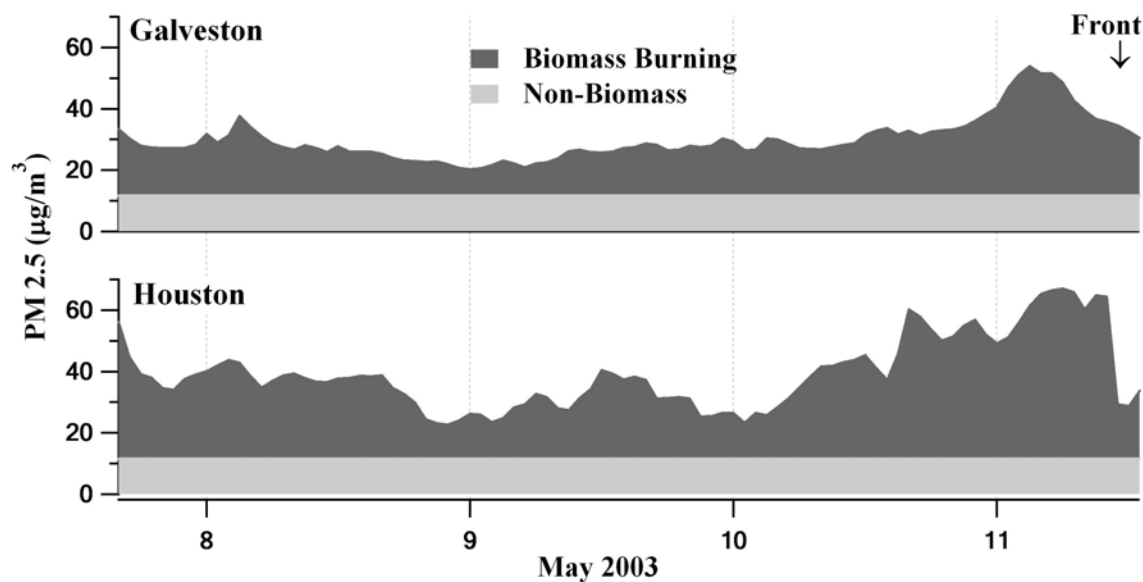


Figure 5.6. PM_{2.5} concentrations in Galveston and Houston during the smoke episode in 2003. The light shaded region represents the average PM_{2.5} concentration measured at these locations over the same time period in 2002.

5.3 In situ measurements

5.3.1 Aerosol size and growth factor measurements

Aerosol size distributions measured using a differential mobility analyzer (DMA) and size-resolved hygroscopic growth distributions measured using a tandem differential mobility analyzer (TDMA) were used to infer the size-dependent concentration of different aerosol types. Hygroscopic properties of particles have been studied using Humidified TDMA systems in several areas [Swietlicki *et al.*, 1999, 2000; Kreidenweis *et al.*, 2001; Hameri *et al.*, 2001]. For this study, the measured hygroscopicity is used both to isolate the size-dependent fractional contribution of each of the particle types present, and to predict the response of the size distribution to changes in RH. The schematic of the DMA / TDMA system used in this study is shown in Figure 5.7. The components of the system were continuously controlled through National Instruments LabVIEW-based software. Sequential measurement of the total size distribution and the size-resolved hygroscopicity of a range of particle sizes is accomplished by alternating the flow path within the system through a number of computer controlled solenoid valves. A complete set of measurements required approximately 6 hours.

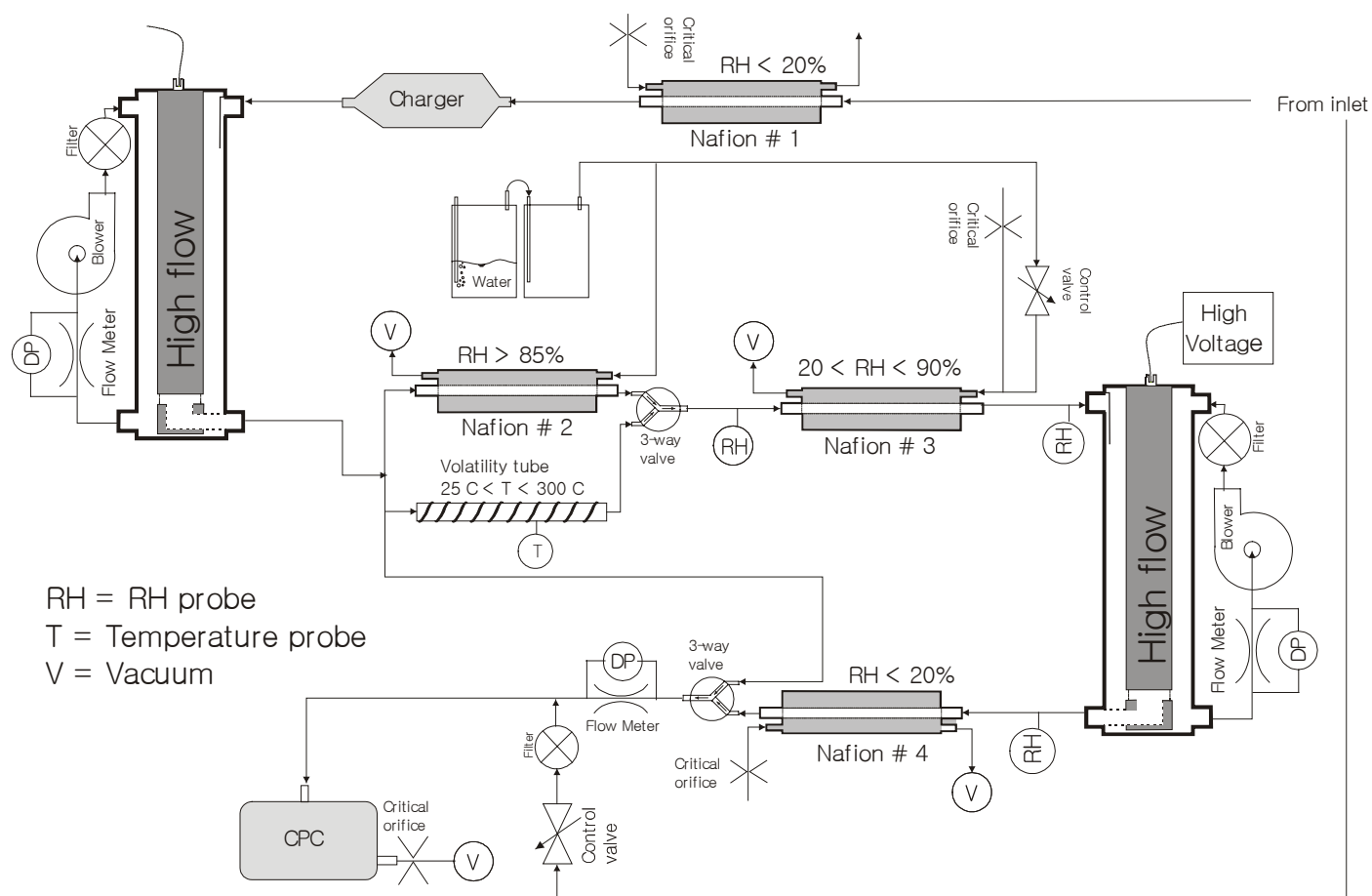


Figure 5.7. Schematic of the DMA / TDMA system operated in College Station.

5.3.2 RH Scan and humidified temperature scan

To complement the size distributions and fixed-RH hygroscopic growth measurements, the hygroscopic response of the aerosol over a wide RH range was measured for a subset of the particle sizes (50, 100, and 200 nm). These measurements will be referred to as RH scans, and the TDMA in this operational mode referred to as a humidity scanning TDMA (HS-TDMA) in the discussion that follows. The hygroscopic growth of certain compounds such as ammonium sulfate is not uniquely related to RH.

Instead, hysteresis is observed as the aerosol is exposed to increasing and then decreasing RH. Because this hygroscopic growth hysteresis can be used to identify the compounds present in the aerosol, the HS-TDMA sequentially measures growth factors along any hysteresis loop that may be present.

The response of the aerosol to elevated temperatures was also measured. Although neither hygroscopicity nor volatility is uniquely related to aerosol composition, consideration of both can often constrain the aerosol composition to a greater degree than is achievable when considering one or the other. When used to evaluate the volatility of the aerosol, the TDMA will be referred to as a Humidity-Temperature TDMA (HT-TDMA), and the measurements made will be referred to as temperature scans. In this mode of operation, the size-resolved particles separated by the upstream DMA are introduced into a heated tube in which the temperature is varied from 300 °C to ~ 40 °C. The aerosols that do not fully volatilize are then exposed to a relative humidity of about 85%. This coupled volatilization / humidification permits identification of the volatility behavior of different particle populations as will be discussed in the results below.

5.4 Analysis procedure

5.4.1 Distribution parameterizations

The lognormal distribution often provides a good fit for aerosol distributions and is routinely used in atmospheric applications [Seinfeld and Pandis, 1998]. For this study, all measured size, hygroscopicity, and volatility distributions were fitted with between one and four lognormals, each of which is described by,

$$\frac{dN_i}{d \log D_p} = \frac{N_i}{\sqrt{2\pi} \cdot \log(\sigma_{g,i})} \exp \left[-\frac{(\log D_p - \log D_{pg,i})^2}{2 \cdot (\log \sigma_{g,i})^2} \right], \quad (5.1)$$

where N_i is the total number concentration, $D_{pg,i}$ is the geometric mean diameter, and $\sigma_{g,i}$ is the geometric standard deviation for mode i .

5.4.2 Isolation of the biomass burning aerosol by hygroscopicity-based partitioning

The hygroscopic growth factor (D_p / D_p^*) is defined as the ratio of the hydrated diameter of the aerosol at elevated RH (85 % for this study), D_p , to the initially separated particle diameter at low RH, D_p^* . Throughout the study period, hygroscopic growth factors of particles having diameters of 25, 50, 100, 200, 300, 450, and 600 nm were measured approximately once every six hours. Figure 5.8 shows an example of hygroscopic growth factor distributions measured at 09:40 CDT on May 10, 2003. The similar appearance of the distributions for all but the smallest and largest particles suggests the dominance of a single particle type, which, in this case, is the biomass burning aerosol. As shown in the figure, most distributions contained two distinct

hygroscopic modes. Additionally, a third mode was often needed to describe the distributions using lognormals.

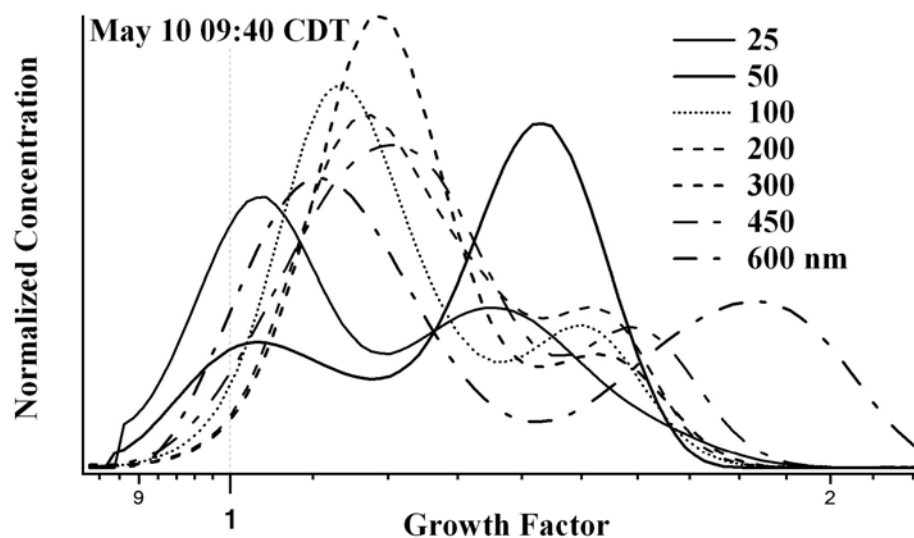


Figure 5.8. Hygroscopic growth factor distribution measured at 09:40 CDT 10 May 2003.

Aerosols can be classified into discrete categories based upon hygroscopicity. For example, black carbon and dust are non-hygroscopic aerosols with growth factors of about 1.0. Organic aerosol particles exhibit limited growth, the magnitude of which is dependent upon the water solubility and molecular weight of the organic compounds. *Kotchenruther and Hobbs* [1998] measured hygroscopic growth factors of between 1.00 and ~ 1.12 for $80\% < RH < 100\%$ for Brazilian hazes influenced by biomass burning. Aerosols composed of inorganic compounds such as sodium chloride and ammonium sulfate are more hygroscopic. The growth factors of ammonium sulfate, ammonium bisulfate, and ammonium nitrate particles at 85% RH are 1.53, 1.59, and 1.56,

respectively. For all particles that exhibit intermediate growth factors, it has been assumed that the aerosol is a combination of insoluble compounds and sulfates. Using the median hygroscopic growth factors parameterized by lognormal fitting, the aerosol was partitioned into five aerosol categories referred to here as hydrophobic, local organic, biomass burning, organic / sulfate, and sulfate. Although the “local organic” aerosol type had a hygroscopic growth factor similar to that of the biomass burning particles, an unexpected bimodal biomass burning aerosol size distribution resulted when the distinction between the particle types was not made. The organic / sulfate particle type had hygroscopicity intermediate of that of the biomass burning and pure sulfate aerosols. The association between these mixed composition particles and the biomass burning aerosol is unknown. Coagulation of biomass burning and sulfate particles and / or cloud processing of biomass burning particles may be responsible. Averaged growth factors of the lognormals describing each of the five particle types are summarized in Table 5.1.

Table 5.1. Averaged growth factors for 25 - 600 nm diameter particles.

Date / time	Hydrophobic	Local Organic	Biomass Burning	Organic / Sulfate	Sulfate
May 7 16:10	1.00	1.19	1.19	1.36	1.65
8 02:00	1.00	1.20	1.20	1.28	1.54
8 09:30	1.00	1.09	1.09	1.24	1.51
8 17:10	1.00	1.09	1.09	1.25	1.52
9 02:25	1.00	1.08	1.08	1.20	1.53
9 09:55	1.00	1.15	1.15	1.31	1.56
9 17:30	1.00	1.14	1.14	1.28	1.57
10 02:20	1.00	1.14	1.14	1.34	1.60
10 09:40	1.00	1.11	1.11	1.30	1.55
10 17:00	1.00	1.15	1.15	1.31	1.53
11 02:00	1.00	1.14	1.14	1.25	1.47

The fractional categorization was combined with the concurrently measured aerosol size distributions to produce size distributions for each of the five aerosol types considered. All of the aerosol size distributions measured during the biomass burning episode are shown in Figure 5.9. The thick solid line represents the number size distribution measured at 09:40 CDT on May 10, 2003. Data collected at that time will be used below to describe the technique employed to isolate the properties of the biomass burning aerosol.

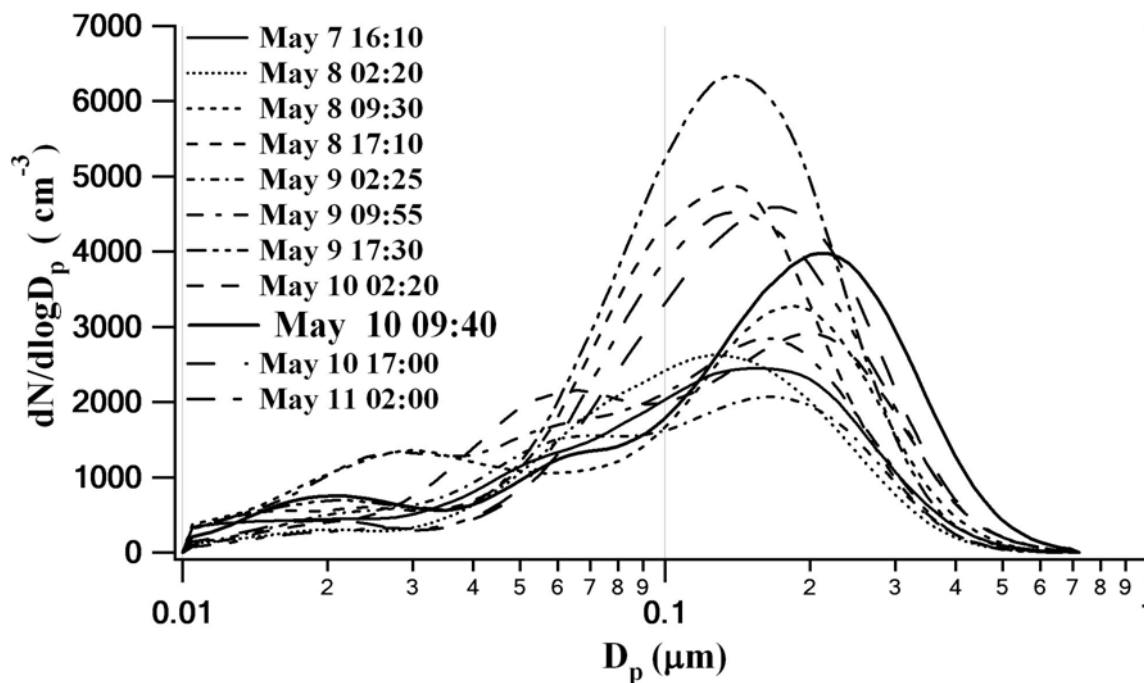


Figure 5.9. All aerosol size distributions measured during the smoke episode.

Since TDMA measurements were limited to particles between 25 and 600 nm, while size distributions spanned a size range between 10 and 700 nm, the fractional contributions of each of the particle types determined using the hygroscopic growth factor distributions were extrapolated. Ultimately, individual size distributions for hydrophobic, local organic, biomass burning, mixed organic / sulfate, and sulfate aerosols were calculated as the product of the total aerosol size distributions and the size-dependent fraction of each of the five different particle types. Isolation of the biomass burning aerosol size distribution in this way permitted investigation of its optical properties. A graphical example of the procedure used is shown in Figure 5.10. The top graph shows the size-dependent fractional contribution of each of the five particle types determined from the hygroscopic growth factor distributions. The bottom graph shows the overall size distribution along with the distributions for each of the particle types, which are simply described by the product of the overall size distribution and the particle type fractions.

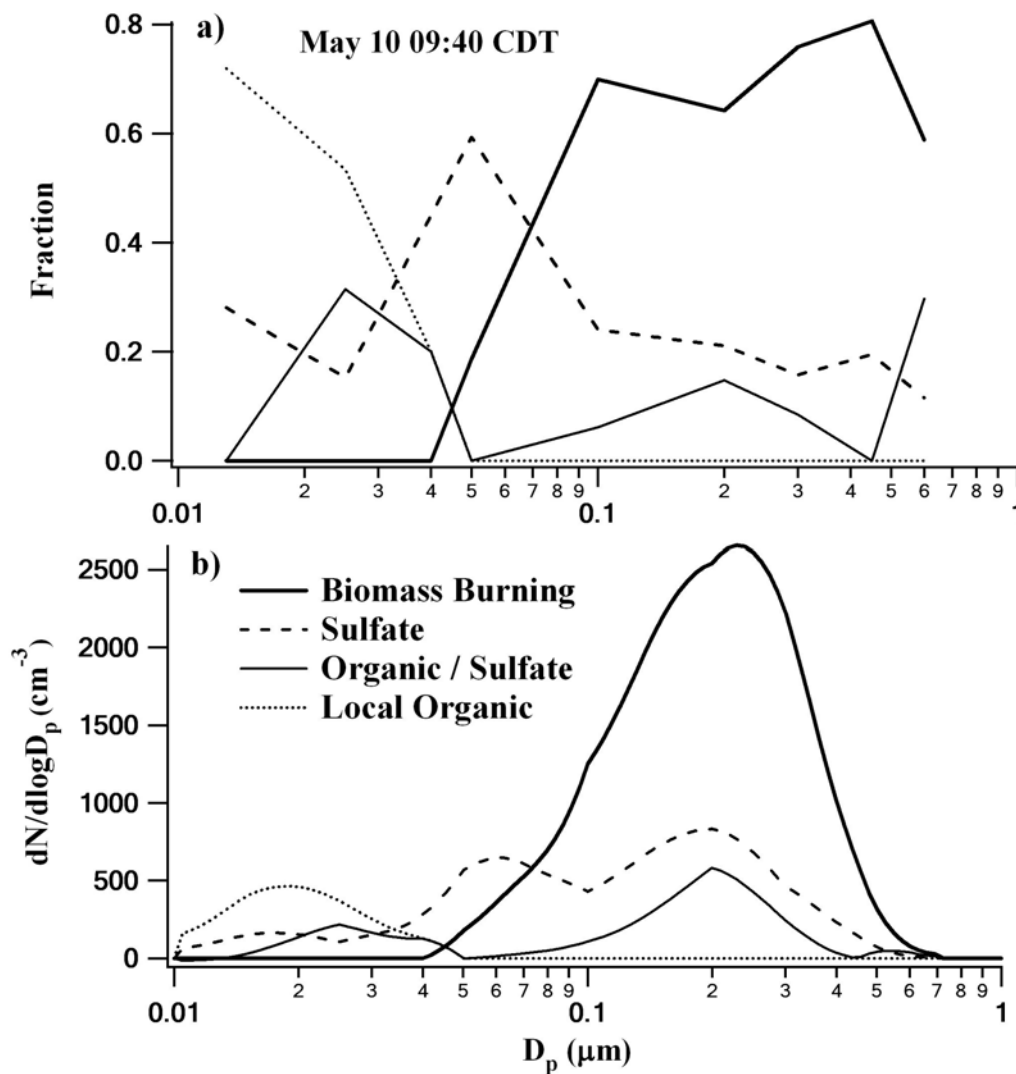


Figure 5.10. Top graph shows the size-dependent fractional contribution of each of the particle types considered to the overall size distribution. The bottom graph shows the measured total size distribution and the calculated distributions for each of the different particle types.

5.4.3. Optical properties calculations

The aerosol extinction coefficient is related to the size-dependent concentration and composition of an aerosol through

$$\sigma_{ext} = \sum_{i=1}^n \int_0^{\infty} \frac{\pi}{4} D_p^2 Q_{ext}(m, \alpha, i) \frac{dN_i}{d \log D_p} d \log D_p, \quad (5.2)$$

where i represents the distinct aerosol components considered, D_p is the particle diameter over which the integral is performed, $Q_{ext}(m, \alpha, i)$ is the Mie particle extinction efficiency, which is function of the complex refractive index (m) and size parameter with wavelength λ ($\alpha = \pi D_p / \lambda$), $dN / d \log D_p$ is the size distribution of species i measured by the DMA / TDMA. The refractive index of aged biomass burning aerosol was assumed to be $1.54 - 0.018i$ [Haywood *et al.*, 2003]. The refractive indices of the other aerosol types were estimated by assuming the particles were composed of mixtures of ammonium bisulfate, elemental carbon, and organic carbon. The absence of a hysteresis loop in the RH-dependent growth factor of the sulfate particles suggests they were probably either composed of ammonium bisulfate or sulfuric acid. For the calculations discussed below, ammonium bisulfate was assumed. The organic to elemental carbon mass ratio was assumed to be 20 for the biomass burning aerosol. The ratio of the largely insoluble carbonaceous content of the aerosol to the soluble inorganic content was calculated based on the hygroscopic behavior. Extinction, scattering, and backscattering distributions for the biomass burning and non-biomass burning aerosols were calculated both for dry conditions and at variable RH. These distributions were then integrated to determine the total extinction coefficient at 550 nm, and the extinction-to-backscattering ratios at 532 and 1064 nm. The mass concentration of the biomass burning aerosol was calculated assuming a density of 1.5 g/cm^3 . This is approximately half way between that observed by Reid and Hobbs [1998] and Ross *et al.*

[1998] of 1.35 and 1.8 g/cm³, respectively. This mass concentration is used to determine the mass extinction efficiency of the aerosol. The extinction-to-backscattering ratio, $S = \frac{\sigma_{ext}}{\sigma_{back}}$, is valuable for interpretation of lidar data. S was calculated for both 532 and 1064 nm. The dependence of this parameter on RH was also considered.

5.5 Results and discussion

5.5.1 Particle type fractions and size distributions

The measured aerosol size distributions and size-resolved hygroscopic growth factor distributions are shown in the contour plots in Figures 5.11 and 5.12, respectively. Although the distributions varied throughout the period, each possessed a mode centered at between about 0.15 and 0.25 μm . Total number concentrations ranged from 1770 to 3800 cm⁻³ with an average of 2580 cm⁻³ during the sampling period. The maxima in many of the contour plots in Figure 5.12 at a growth factor of about 1.1 is due to the presence of a significant concentration of biomass burning particles throughout the measured size range. Although multiple modes were almost always present in the measured distributions, they are sometimes difficult to discern in the presence of the more concentrated biomass burning particles. The five single particle-type size distributions were determined by combining measured size distributions with the fractional contribution of each particle type determined from the hygroscopic growth distributions. Biomass burning aerosols contributed more to the total number concentration than any of the other particle types.

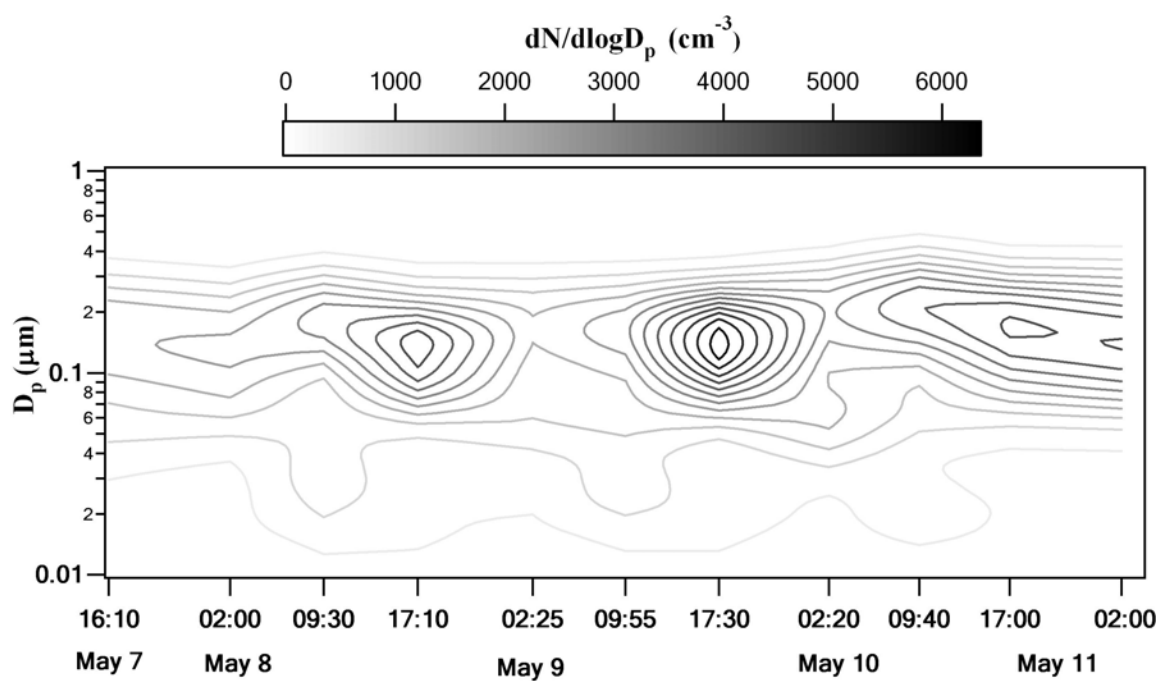


Figure 5.11. Evolution of the aerosol number size distribution during the four-day sampling period.

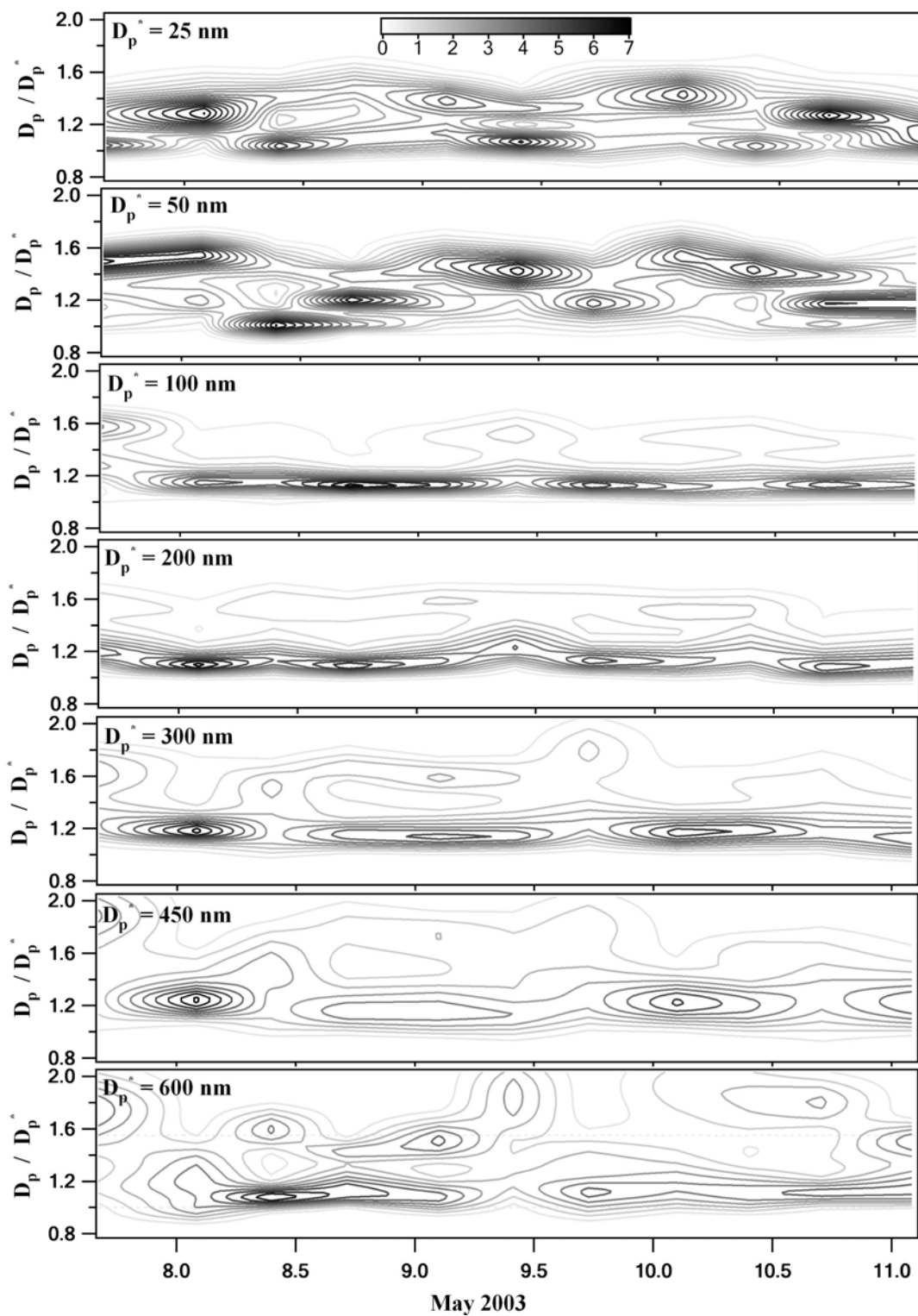


Figure 5.12. Hygroscopic growth factor distributions for each of the seven particle sizes for which measurements were made.

Figure 5.13a shows examples of HS-TDMA measurements for particles having dry diameters of 50, 100, and 200 nm. Separation between the curves tracing the solid and hollow markers would indicate the presence of particle types that exhibit hygroscopic growth hysteresis. With very few exceptions, such deliquescent particles were not observed. Trimodal growth profiles were usually present for $RH > 60\%$. This indicates the presence of as many as three particle types exhibiting distinct hygroscopic behavior. Up to four modes were observed at high RH. The relative concentration of particles within each of the growth factor modes is reflected by the marker size. Figure 5.13b shows examples of HT-TDMA data collected during the smoke episode. The gradual decrease in particle size with increasing temperature is characteristic of organic aerosols that are typically composed of a wide range of compounds, each of which volatilizes at a different temperature. In contrast, particles that are more hygroscopic at lower temperatures volatilize over a rather narrow temperature range centered at approximately $220\text{ }^{\circ}\text{C}$, which is typical of sulfate-containing particles. Although the HS-TDMA and HT-TDMA data are not used directly in the optical calculations discussed below, these data provide greater insight into the composition and properties of the aerosol than the fixed-RH measurements.

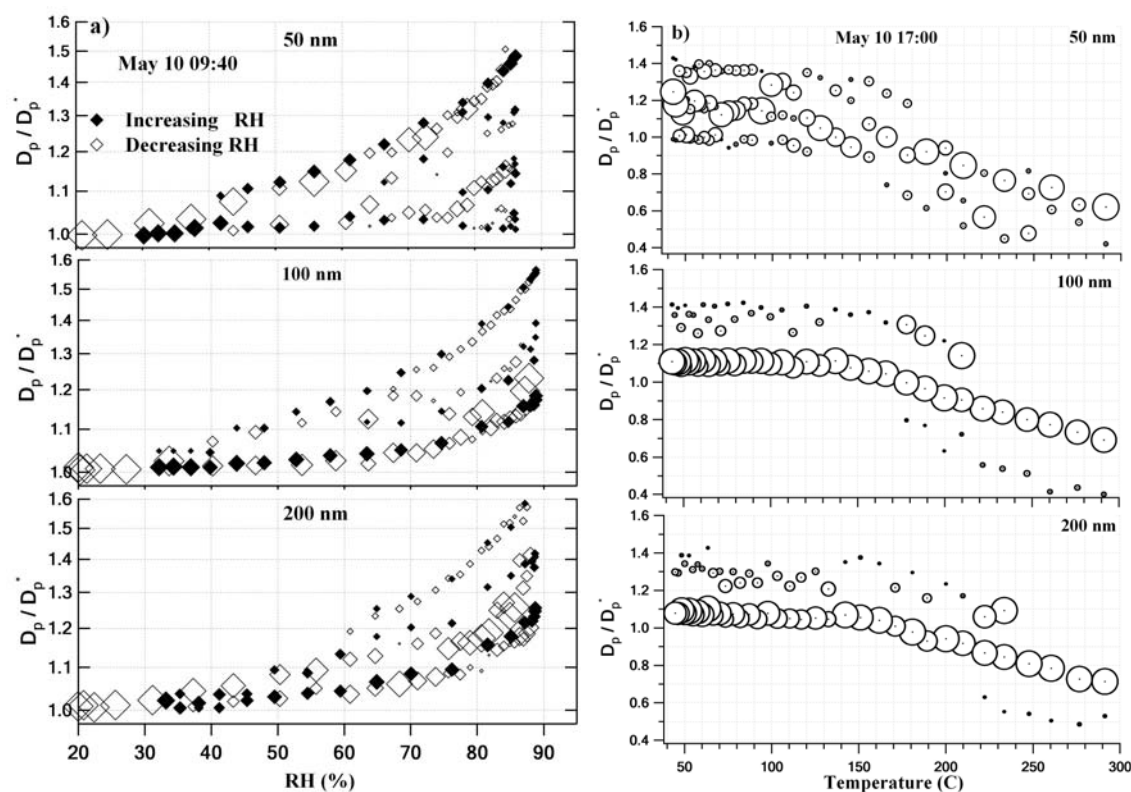


Figure 5.13. a) HS-TDMA measurements and b) HT-TDMA measurements on 10 May 2003. Solid markers represent growth factors measured as the RH was decreased, while hollow markers represent growth factors measured as the RH was increased. Separation between these measurements at a given RH indicates that deliquescent particles are present. Marker size reflects the concentration within each mode when multiple modes were present.

5.5.2 Partitioned size distribution

Figure 5.14 shows the five single particle-type size distributions determined by combining measured size distributions with the fractional contribution of each particle type determined from the hygroscopic growth distributions. Biomass burning aerosols contributed more to the total number concentration than any of the other particle types. The source of the sulfate aerosol is unknown. Sulfur dioxide emitted through biomass burning will form sulfates during transport. However, the sulfate produced in this way would likely just condense on the co-emitted biomass burning aerosols rather than forming new particles. The hygroscopicity of the sulfate class of particles identified here suggests the insoluble content was relatively low. It is speculated here that the sulfate particles were formed outside of the biomass burning aerosol plume and mixed with the smoke closer to the sampling site. The population of particles having hygroscopicity intermediate of the sulfate and biomass burning aerosol could have resulted from coagulation or cloud processing of the smoke. However, results from a simple coagulation model did not support the former of these hypotheses. The hydrophobic population is believed to be composed of primary elemental and organic carbon containing particles. The size distribution of this particle class is consistent with our previous observations in the Houston area. This, coupled with a weak association with the smoke aerosol concentration, suggests these particles may have local sources. Table 5.2 shows aerosol number size distribution parameters for the five aerosol types.

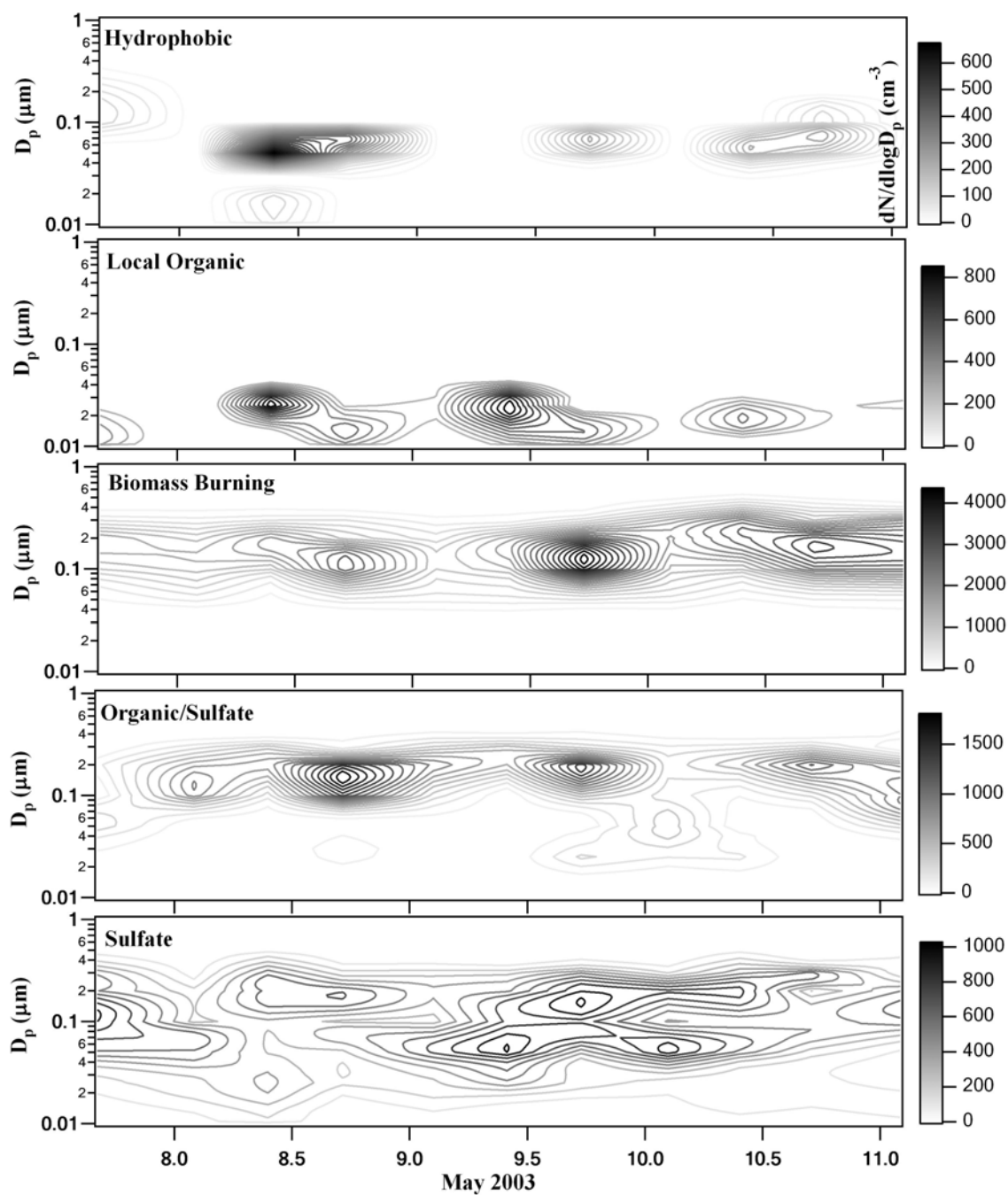


Figure 5.14. Partitioned size distributions.

Table 5.2. Aerosol number size distribution lognormal parameters for the five aerosol types identified in the hygroscopic growth factor distributions.

Time/ Mode		Hydrophobic			Local Organic			Biomass			Organic / Sulfate			Sulfate		
		N	D_{pg}	σ_g	N	D_{pg}	σ_g	N	D_{pg}	σ_g	N	D_{pg}	σ_g	N	D_{pg}	σ_g
May 7 16:10	1	59.3	0.14	1.56	124.6	0.01	1.34	652.7	0.14	1.64	39.1	0.03	1.49	701.5	0.10	2.07
	2				68.4	0.03	1.38	167.0	0.21	1.29	102.9	0.06	1.33	29.6	0.29	1.16
8 02:00	1	4.4	0.06	1.29	30.6	0.02	1.36	154.6	0.07	1.38	232.6	0.11	1.34	235.1	0.04	1.92
	2	0.6	0.53	1.11	1.5	0.04	1.15	745.9	0.14	1.64	220.8	0.19	1.40	157.2	0.07	1.35
	3													87.67	0.17	1.36
8 09:30	1	37.6	0.01	1.30	291.9	0.03	1.40	887.7	0.16	1.53	196.7	0.15	1.46	319.2	0.03	2.01
	2	194.4	0.05	1.33							123.6	0.24	1.29	393.0	0.20	1.67
8 17:10	1	116.6	0.06	1.31	82.5	0.01	1.24	1327.8	0.11	1.55	50.8	0.03	1.32	90.0	0.03	1.48
	2				128.5	0.02	1.51	74.1	0.28	1.19	772.0	0.14	1.46	113.0	0.07	1.28
	3													273.4	0.18	1.42
9 02:25	1				173.1	0.03	1.75	79.4	0.06	1.31	71.7	0.10	1.34	121.8	0.02	1.55
	2							586.7	0.13	1.68	320.8	0.20	1.43	248.1	0.06	1.39
	3													190.2	0.19	1.50
9 09:55	1				407.3	0.02	1.55	462.2	0.09	1.58	240.3	0.23	1.38	162.4	0.03	1.38
	2							527.2	0.17	1.40				256.2	0.06	1.35
	3													416.3	0.13	1.68
9 17:30	1	64.4	0.06	1.28	174.7	0.01	1.36	2133.9	0.13	1.57	96.1	0.03	1.35	75.1	0.03	1.34
	2				19.8	0.03	1.20				569.6	0.17	1.45	252.0	0.07	1.40
	3													462.3	0.17	1.53
10 02:20	1				83.5	0.02	1.42	828.2	0.12	1.73	269.3	0.05	1.67	409.3	0.06	1.51
	2				183.5	0.04	1.20	439.4	0.25	1.39	140.7	0.20	1.49	252.8	0.19	1.35
10 09:40	1	69.5	0.06	1.33	206.8	0.02	1.50	1054.7	0.16	1.65	71.8	0.03	1.39	69.0	0.02	1.48
	2							462.3	0.27	1.36	196.3	0.20	1.40	211.9	0.06	1.37
	3													406.5	0.19	1.57
10 17:00	1	81.9	0.07	1.38	115.5	0.02	1.46	1869.7	0.15	1.68	398.6	0.18	1.43	52.8	0.02	1.38
	2	12.2	0.14	1.17	7.8	0.04	1.14							307.5	0.10	1.77
	3													101.1	0.28	1.18
11 02:00	1				84.1	0.03	1.34	1639.2	0.14	1.66	587.4	0.11	1.71	51.0	0.02	1.34
	2							212.8	0.26	1.24				347.8	0.13	1.63
	3													12.1	0.42	1.19

$N(\text{cm}^{-3})$: Number concentration; $D_{pg}(\mu\text{m})$: Geometric mean diameter

σ_g : Geometric standard deviation

5.5.3 Calculated extinction coefficients with relative humidity

The evolution of the biomass burning-only differential extinction coefficient distribution over the sampling period is shown in Figure 5.15. Whereas the biomass burning aerosol number concentration was greatest on May 9, the increased particle size observed later in the sampling period resulted in an increased extinction coefficient. The enhancement in extinction with relative humidity is expected to be far less for the sparingly hygroscopic biomass burning aerosol than for other aerosol types such as sulfates. This expectation is supported by the minimal separation between the extinction coefficient calculated for an aerosol at 40% RH and that calculated for the same aerosol at 60 and 85% RH, as is shown in Figure 5.16. In contrast, the contributions to the total extinction coefficient by the sulfate and organic / sulfate mixtures increase significantly with increased RH. The hydrophobic and local organic particle classes are not shown in the figure since they contribute little to the overall extinction coefficient. Figure 5.17 shows the relative importance of the biomass burning, sulfate, and organic / sulfate particles to the overall extinction coefficient. Despite the fact that the biomass burning aerosol is sparingly hygroscopic, it still results in more than half the total extinction coefficient at 85% RH for much of the sampling period.

The impact of each of the aerosol types on local visibility is dependent on both the size distributions and the local ambient RH. Figure 5.18 shows the contributions to the calculated extinction coefficient at ambient RH of each of the three primary aerosol types. As was true for the fixed-RH calculations, the biomass burning aerosol extinction coefficient increases only slightly as RH increases overnight and in the early morning.

The time resolution shown in this figure reflects that of the RH measurements (one hour) and not the aerosol measurements (six hours).

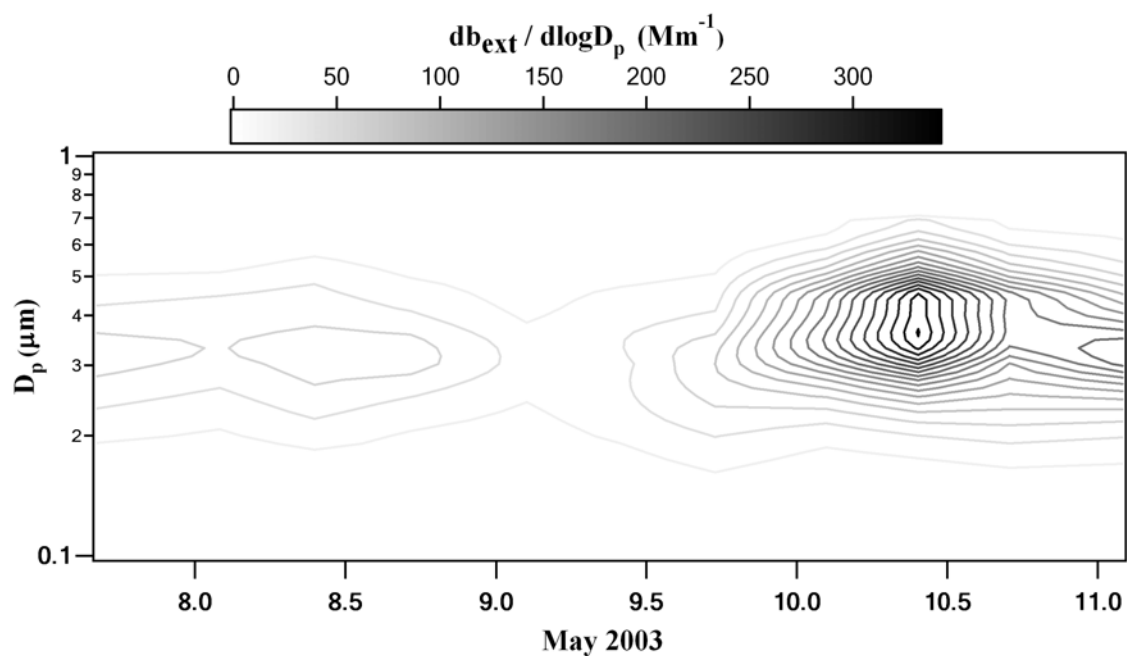


Figure 5.15. Contour plot of biomass burning aerosol extinction coefficient distribution for a wavelength of 550 nm.

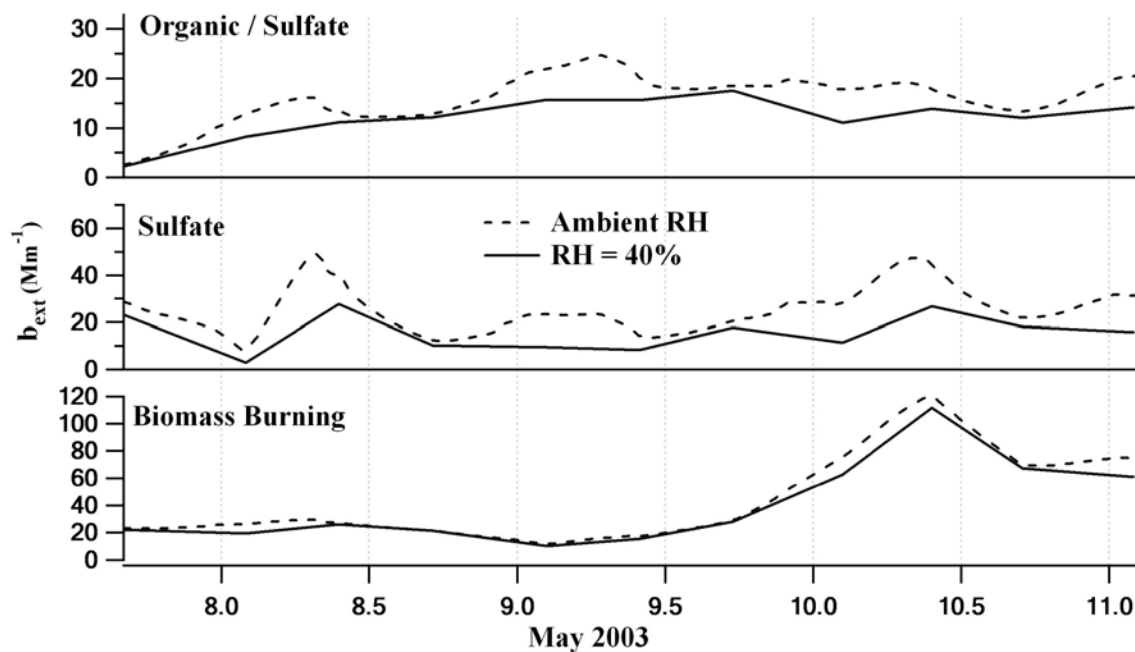


Figure 5.16. Aerosol extinction coefficients at ambient and 40% RH at a wavelength of 550 nm.

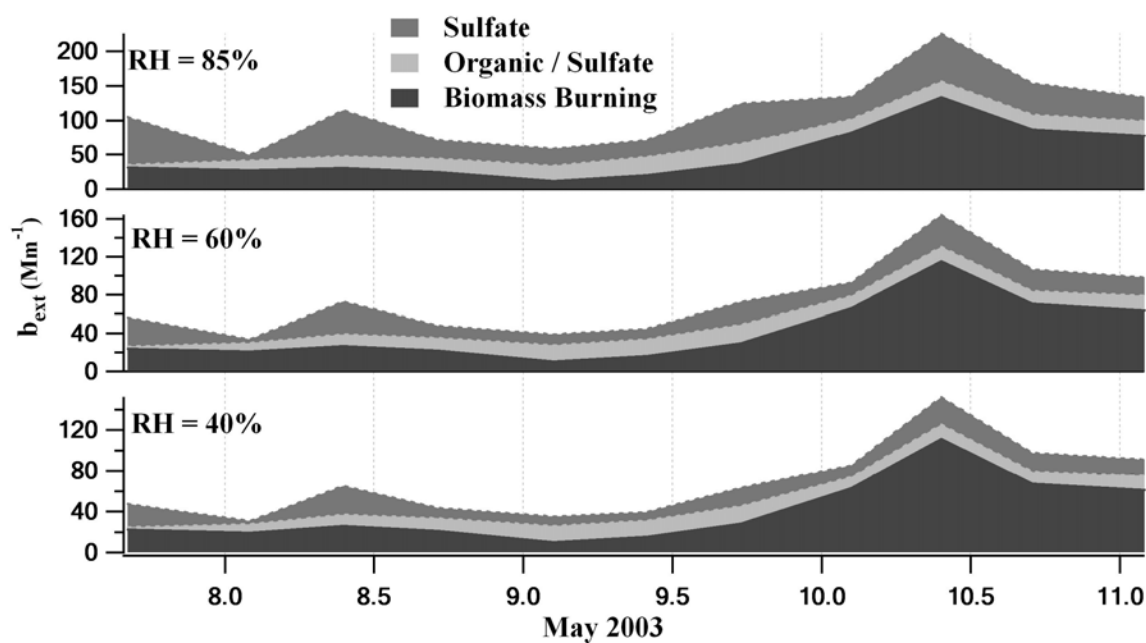


Figure 5.17 Variation of aerosol extinction coefficients at 550 nm as a function of relative humidity.

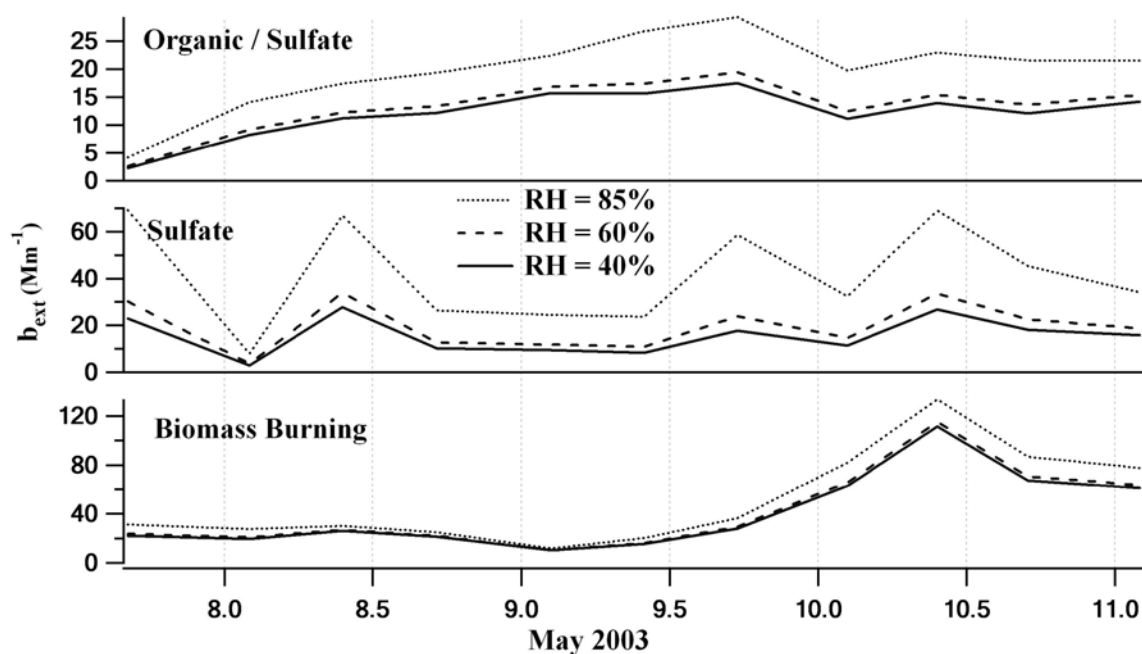


Figure 5.18. Dependence of specific aerosol class extinction coefficients at 550 nm on relative humidity.

Mass extinction efficiencies provide a convenient means for relating measured or modeled mass concentration of an aerosol to its radiative impact. The IMPROVE program recommends value of $4 \text{ m}^2/\text{g}$ and $10 \text{ m}^2/\text{g}$ for organic carbon and elemental carbon aerosols, respectively. Figure 5.19 shows mass extinction efficiencies for biomass burning and non-biomass burning aerosols calculated using the size distributions determined for each of the particle classes. The values calculated for the biomass burning aerosol ranges from 4 to $6 \text{ m}^2/\text{g}$, which is consistent with values reported by Haywood *et al.* [2003]. The mass extinction efficiency of the biomass burning aerosol was greatest on May 10 when the size distribution shifted slightly to larger diameter.

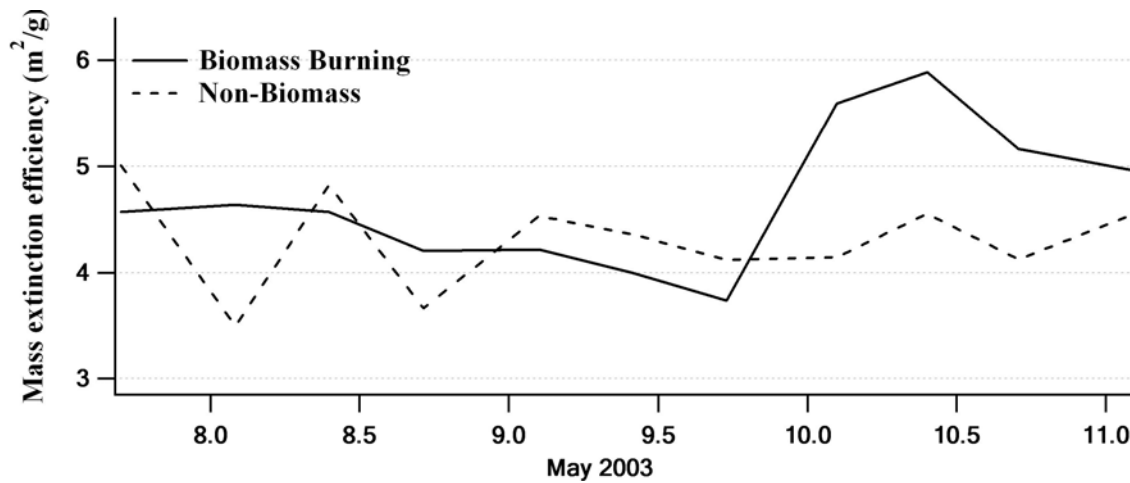


Figure 5.19. Mass extinction efficiency for biomass and non-biomass burning aerosols for a wavelength of 550 nm.

The extinction-to-backscattering ratio, $S = \frac{\sigma_{ext}}{\sigma_{back}}$, is an important parameter for

interpretation of lidar data. *Ackermann* (1998) showed that S typically varies from 15 to 75 steradians (sr) for a typical continental aerosol size distribution and refractive index. *Masonis et al.* [2003] showed that S averaged 25.4 sr for marine aerosol at 532 nm, while *Anderson et al.* [2000] described an average between 64 and 40 sr for stagnant and rapid transport air mass categories, respectively. They found that S varied between 50 and 90 sr at 532 nm for smoke layers in the Southern Hemisphere. The RH-dependent lidar ratio was calculated using the biomass burning aerosol size distributions for wavelengths of 532 and 1064 nm. The accuracy of these calculations depends upon the extent to which the extinction and backscattering distributions are truncated since only particles smaller than 700 nm were measured. Figure 5.20 shows the differential extinction and 180° backscattering distributions at 532 nm and 1064 nm on 10 09:40

May 2003 at RH=40% and at ambient RH. The extinction coefficient is most sensitive to particles with diameters between 300 and 500 nm, while the backscattering coefficient distribution had maxima at 210, 380, and 520 nm for 532nm, but only at 380 nm for 1064 nm. Although both the extinction and backscattering distributions were non-zero at the maximum particle size measured, the magnitude of the error caused by truncation is believed to be relatively small.

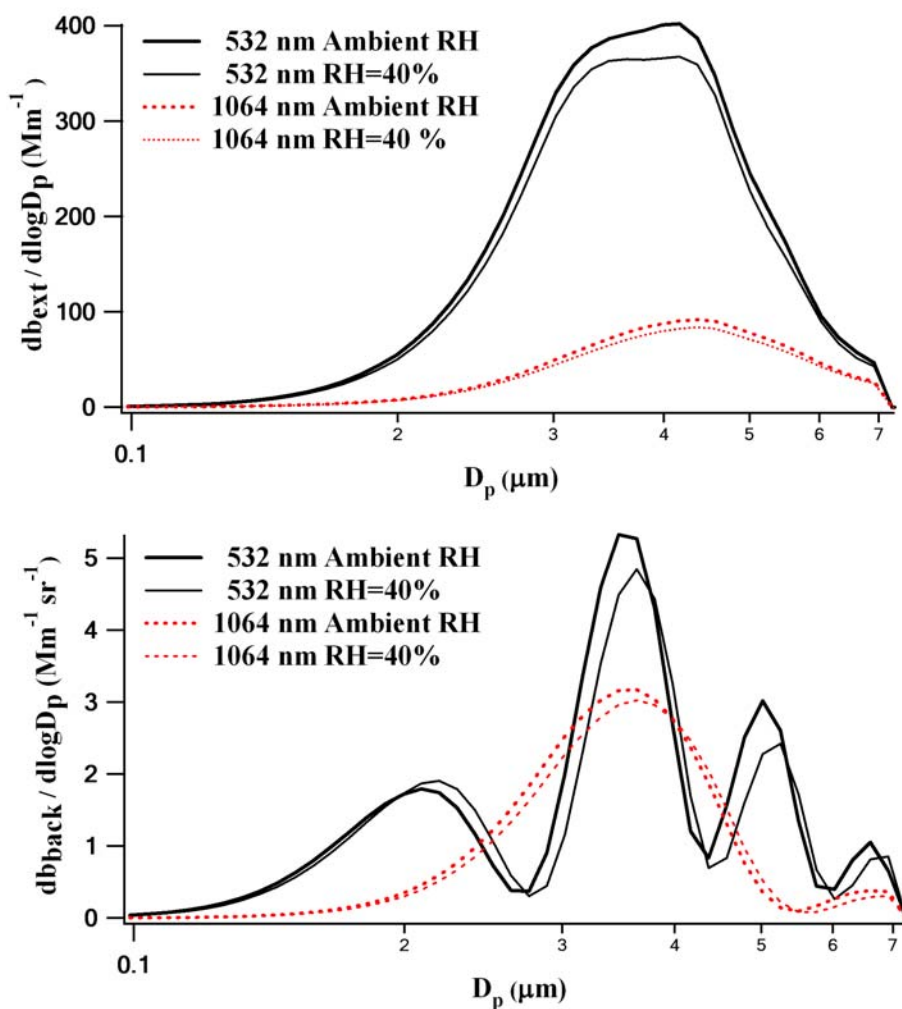


Figure 5.20. Extinction and back scattering coefficients at 532 nm and 1064 nm as functions of particle diameter and RH at 09:40 on 10 May 2003.

As was done with the extinction coefficient, the lidar ratio was also calculated at ambient RH for the biomass burning aerosol. Figure 5.21 shows S for both 532 and 1064 nm wavelengths at ambient RH throughout the sampling period. S varied between 61 and 105 sr, with a mean value of 82 sr, at 532 nm, and between 23 and 43 sr, with a mean value of 30 sr, for a wavelength of 1064 nm. These values are in good agreement with values of 50 – 90 sr at 532 nm measured within smoke layers in the Southern Hemisphere [Anderson *et al.*, 2000].

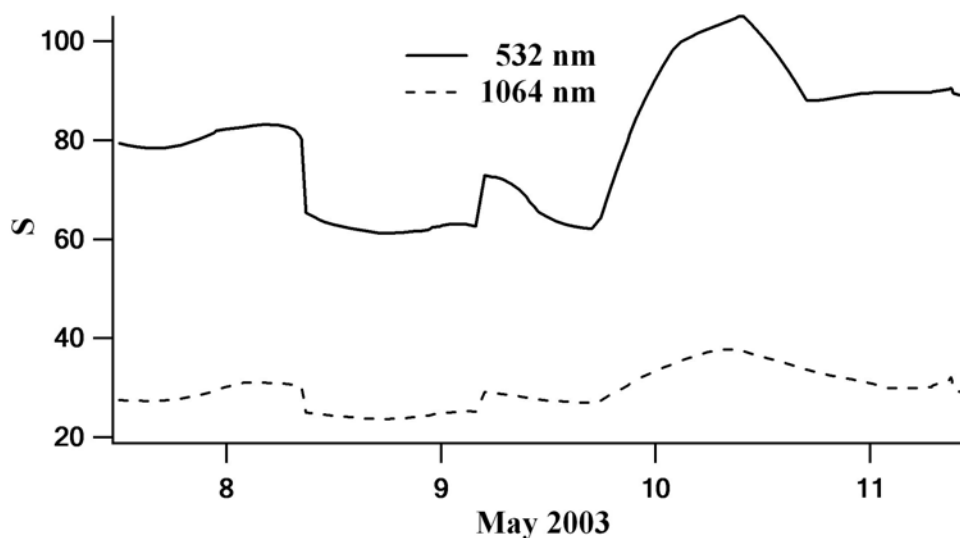


Figure 5.21. Time series of the calculated lidar ratio at 532 and 1064 nm at ambient RH.

To identify the influence of RH on the lidar ratio, the calculations were repeated at 30, 40, 50, 60, 70, 80, 85, and 90 % RH. Figure 5.22 shows the time- and RH-dependent S during the measurement period at both 532 nm and 1064 nm wavelengths. The ratios lie between 60 and 110 sr for 532 nm and between 23 and 46 sr for 1064 nm. Generally, S increased with RH, and the highest S values were observed on 10 of May

when the concentration of biomass burning aerosol was highest. Figure 5.23 shows the study-average RH-dependent S normalized by S calculated at 30% RH. The solid lines represent the mean for each RH and the vertical lines are standard deviations determined from all of the measurements. Although the lidar ratio generally increases with increasing RH, there is substantial variability even for this rather limited dataset.

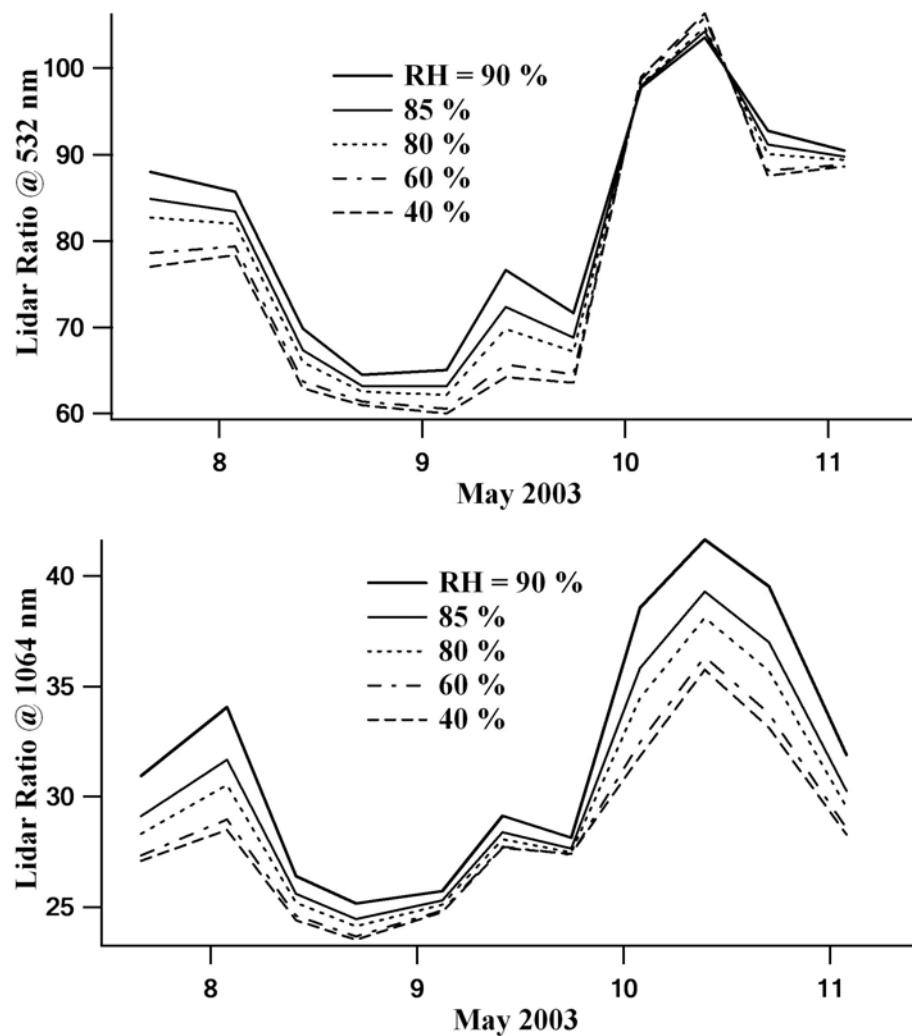


Figure 5.22. Time series of the lidar ratio at 532 nm and 1064 nm as a function of RH.

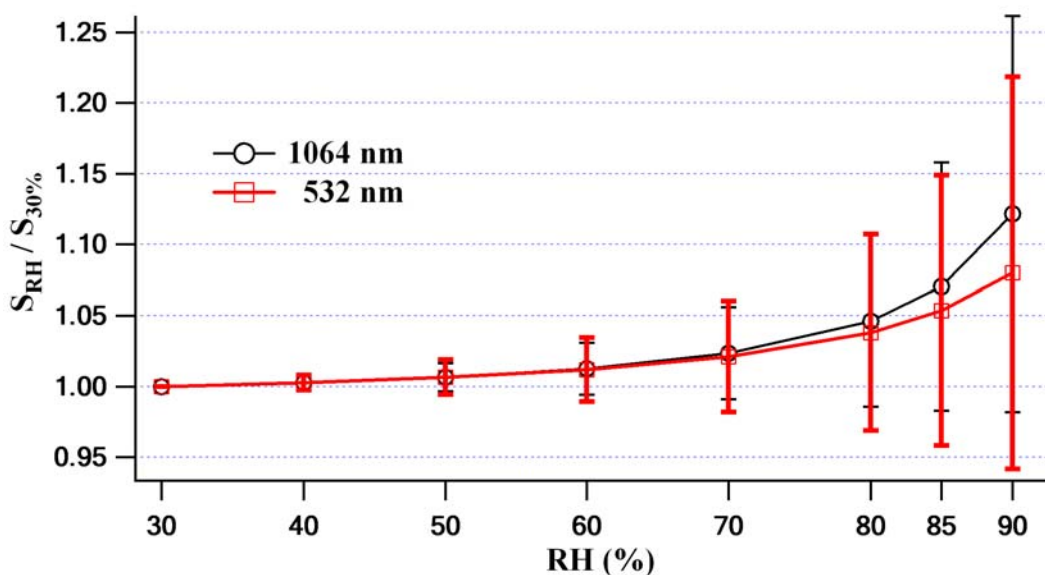


Figure 5.23. RH-dependence of the lidar ratio normalized by the lidar ratio calculated at 30% RH. The means and standard deviations are shown for each RH.

5.6 Summary

A DMA / TDMA system was used to characterize the size distribution and size-resolved hygroscopicity and volatility of a smoke-dominated aerosol in College Station, TX from May 7 ~ 11 of 2003. Smoke from fires in the Yucatan Peninsula was transported across the Gulf of Mexico and into Texas throughout this period. The collected hygroscopicity data were used to separate the sparingly hygroscopic biomass burning particles from other aerosol types. Measured size distributions, and the aerosol properties derived from the TDMA data, were used to calculate RH-dependent aerosol extinction coefficients at a wavelength of 550 nm. These extinction coefficients, and mass concentrations derived from the same data, were used to calculate the mass extinction efficiency for the different aerosol types identified. The data were also used to calculate extinction-to-backscattering lidar ratios for biomass burning aerosols at the

common lidar wavelengths of 532 and 1064 nm. The approach used to isolate the size distributions of each of the particle types identified permits examination of the optical properties of biomass burning particles even in conditions in which other particle types are more abundant. This provides a method for characterizing changes in biomass burning aerosols that occur over periods of days, which would typically not be possible due to the accumulation of additional particle types over time.

CHAPTER VI

SUMMARY AND CONCLUSIONS

In this dissertation, I describe a method for examining the optical and cloud forming properties of specific classes of aerosols. The underlying objective of this work is to contribute to an improved understanding of the direct and indirect effects of aerosols on climate. In Chapter II, I describe use of data collected during the Asian Aerosol Characterization Experiment (ACE-Asia) to examine the composition and homogeneity of a complex aerosol generated in the deserts and urban regions of China and other Asian countries. An aircraft-based tandem differential mobility analyzer was used for the first time during this campaign to examine the size-resolved hygroscopic properties of particles having diameters between 40 and 586 nm. The study location offered a unique opportunity to investigate the impact of anthropogenic emissions on naturally-generated dust particles. Hygroscopic growth factors at 90% RH typically exceeded 1.4, suggesting the soluble fraction of the aerosol was relatively high. The mean standard deviation of the measured growth factor distributions, which is related to the compositional heterogeneity of the aerosol, increased with increasing particle size, although this trend often reversed for the largest particles considered. Overall, hygroscopicity was observed to increase with proximity to the surface, and with increasing size. One cause of the observed height dependence is the frequent presence of non-hygroscopic dust particles at higher levels that, closer to the surface, were either not observed or had been coated with soluble compounds such as sulfate.

Chapter III describes results from the Asian Dust Above Monterey (ADAM-2003) study designed both to evaluate the degree to which models can predict the long-range transport of Asian dust, and to examine the physical and optical properties of that aged dust upon reaching the California coast. During several of the flights, distinct layers of dust that had been preserved during the transit across the Pacific were observed. These layers were typically present between 2 and 4 km asl. By coupling the measured size distributions with a size-dependent fractional categorization based on the hygroscopic growth measurements, independent size distributions for the dust and other aerosol types were created. Within the sampled layers, both the overall mass concentration and light extinction coefficient were dominated by the larger dust particles. Light scattering coefficients predicted based on the measured size distributions compared well with those directly measured with a nephelometer. The calculated mass extinction efficiency of the dust aerosol was somewhat higher than that observed during other studies suggesting that the size distribution had shifted towards smaller size as gravitational settling removed the largest dust particles.

Chapter IV describes use of aerosol size distributions and hygroscopic growth measured in College Station, Texas to investigate the cloud nucleating properties of a biomass burning aerosol generated from fires on the Yucatan Peninsula. Whereas most other studies designed to investigate biomass burning aerosol have been conducted close to the aerosol source, the data described in this chapter provide details of the properties of an aged smoke aerosol. Measured aerosol size distributions and size-resolved hygroscopicity and volatility were used to infer critical supersaturation distributions of

the distinct particle types that were observed during this period. The average inferred CCN concentrations were 869, 1918, and 2206 (cm^{-3}) at 0.15, 0.5, and 1.0% critical supersaturations, respectively. The predicted CCN concentrations were used in a cloud model to determine the impact of the different aerosol types on the expected cloud droplet concentration. For certain aerosol measurements and cloud updraft velocities, predicted cloud droplet concentrations were lower when the observed sulfate aerosol was considered together with the biomass burning aerosol relative to that when only the biomass burning aerosol was considered. By suppressing activation of the less hygroscopic biomass burning particles, pollution aerosols may actually help preserve the smoke aerosol by reducing wet deposition rates. Furthermore, this represents a scenario in which pollution aerosol may cause a slight reduction in cloud albedo.

Chapter V describes use of the measurements discussed in Chapter IV to examine the optical properties of the smoke-dominated aerosol. As was done to isolate the CCN spectra of the biomass burning aerosol, the collected hygroscopicity data were used to separate the sparingly hygroscopic smoke particles from other aerosol types. The approach used to isolate the size distributions of each of the particle types identified permits examination of the optical properties of biomass burning particles even in conditions in which other particle types are more abundant. The size distributions of the smoke and other particle types, coupled with the aerosol properties derived from the TDMA data, were used to calculate RH-dependent aerosol extinction coefficients at a wavelength of 550 nm. This provides a method for characterizing

changes in biomass burning aerosols that occur over periods of days, which would typically not be possible due to the accumulation of additional particle types over time.

REFERENCES

- ADAM-2003 Science plan, U.S. Navy:
http://www.nrlmry.navy.mil/aerosol/Case_studies/adam/adam_2003_science_plan20030328.pdf, Accessed June 2004.
- Ackermann, J., The Extinction-to-Backscatter Ratio of Tropospheric Aerosol: A Numerical Study, *Journal of Atmospheric and Oceanic Technology*, *15*, 1043-1050, 1998.
- Anderson, T. L., D. S. Covert, S. F. Marshall, M. L. Laucks, R. J. Charlson, A. P. Waggoner, J. A. Ogren, R. Caldow, R. L. Holm, F. R. Quant, G. J. Sem, A. Wiedensohler, N. A. Ahlquist, and T. S. Bates, Performance Characteristics of a High-Sensitivity, Three-Wavelength, Total Scatter/Backscatter Nephelometer, *Journal of Atmospheric and Oceanic Technology*, *13*, 967-986, 1996.
- Anderson, T. L., S. J. Masonis, D. S. Covert, R. J. Charlson, and M. J. Rood, In Situ Measurement of the Aerosol Extinction-to-Backscatter Ratio at a Polluted Continental Site, *Journal of Geophysical Research-Atmospheres*, *105*, 26907-26915, 2000.
- Andreae, M. O., D. Rosenfeld, P. Artaxo, A. A. Costa, G. P. Frank, K. M. Longo, and M. A. F. Silva-Dias, Smoking Rain Clouds Over the Amazon, *Science*, *303*, 1337-1342, 2004.
- Bahreini, R., J. L. Jimenez, J. Wang, R. C. Flagan, J. H. Seinfeld, J. T. Jayne, and D. R. Worsnop, Aircraft-Based Aerosol Size and Composition Measurements During Ace-Asia Using an Aerodyne Aerosol Mass Spectrometer, *Journal of Geophysical Research-Atmospheres*, *108*(D23), 8645, doi:10.1029/2002JD003226, 2003.
- Bergin, M. H., G. R. Cass, J. Xu, C. Fang, L. M. Zeng, T. Yu, L. G. Salmon, C. S. Kiang, X. Y. Tang, Y. H. Zhang, and W. L. Chameides, Aerosol Radiative, Physical, and Chemical Properties in Beijing During June 1999, *Journal of Geophysical Research-Atmospheres*, *106*, 17969-17980, 2001.
- Carrico, C. M., P. Kus, M. J. Rood, P. K. Quinn, and T. S. Bates, Mixtures of Pollution, Dust, Sea Salt, and Volcanic Aerosol During Ace-Asia: Radiative Properties as a Function of Relative Humidity, *Journal of Geophysical Research-Atmospheres*, *108*, 8650-8668, 2003.
- Christopher, S. A., J. Chou, J. L. Zhang, X. Li, T. A. Berendes, and R. M. Welch, Shortwave Direct Radiative Forcing of Biomass Burning Aerosols Estimated Using Virs and Ceres Data, *Geophysical Research Letters*, *27*, 2197-2200, 2000.

- Cocker, D. R., N. E. Whitlock, R. C. Flagan, and J. H. Seinfeld, Hygroscopic Properties of Pasadena, California Aerosol, *Aerosol Science and Technology*, *35*, 637-647, 2001.
- Colarco, P. R., M. R. Schoeberl, B. G. Doddridge, L. T. Marufu, O. Torres, and E. J. Welton, Transport of Smoke From Canadian Forest Fires to the Surface Near Washington, D. C.: Injection Height, Entrainment, and Optical Properties, *Journal of Geophysical Research-Atmospheres*, *109*, D06203, doi:10.1029/2003JD004248, 2004.
- Collins, D. R., H. H. Jonsson, J. H. Seinfeld, R. C. Flagan, S. Gasso, D. A. Hegg, P. B. Russell, B. Schmid, J. M. Livingston, E. Ostrom, K. J. Noone, L. M. Russell, and J. P. Putaud, In Situ Aerosol-Size Distributions and Clear-Column Radiative Closure During Ace-2, *Tellus Series B-Chemical and Physical Meteorology*, *52*, 498-525, 2000.
- Cooke, W. F., C. Lioussé, H. Cachier, and J. Feichter, Construction of a 1 Degrees X 1 Degrees Fossil Fuel Emission Data Set for Carbonaceous Aerosol and Implementation and Radiative Impact in the Echam4 Model, *Journal of Geophysical Research-Atmospheres*, *104*, 22137-22162, 1999.
- Cooke, W. F. and J. J. N. Wilson, A Global Black Carbon Aerosol Model, *Journal of Geophysical Research-Atmospheres*, *101*, 19395-19409, 1996.
- Covert, D. S., J. L. Gras, A. Wiedensohler, and F. Stratmann, Comparison of Directly Measured CCN With CCN Modeled From the Number-Size Distribution in the Marine Boundary Layer During Ace 1 at Cape Grim, Tasmania, *Journal of Geophysical Research-Atmospheres*, *103*, 16597-16608, 1998.
- Dick, W. D., P. Saxena, and P.H. McMurry, Estimation of water uptake by organic compounds in submicron aerosols measured during the Southeastern Aerosol and Visibility Study, *Journal of Geophysical Research-Atmospheres*, *105*, 1471(999JD901001), 2000.
- Draxler, R. R. and G.D. Rolph, HYSPLIT (HYbrid Single-Particle Lagrangian Integrated Trajectory) Model access via NOAA ARL READY Website (<http://www.arl.noaa.gov/ready/hysplit4.html>), 2003.
- Fraser, M. P. and K. Lakshmanan, Using Levoglucosan as a Molecular Marker for the Long-Range Transport of Biomass Combustion Aerosols, *Environmental Science & Technology*, *34*, 4560-4564, 2000.
- Gao, S., D. A. Hegg, and H. Jonsson, Aerosol Chemistry, and Light-Scattering and Hygroscopicity Budgets During Outflow From East Asia, *Journal of Atmospheric Chemistry*, *46*, 55-88, 2003.
- Gasparini, R., R. J. Li, and D. R. Collins, Integration of Size Distributions and Size-

- Resolved Hygroscopicity Measured During the Houston Supersite for Compositional Categorization of the Aerosol, *Atmospheric Environment*, 38, 3285-3303, 2004.
- Hameri, K., M. Vakeva, P. P. Aalto, M. Kulmala, E. Swietlicki, J. Zhou, W. Seidl, E. Becker, and C. D. O'dowd, Hygroscopic and Ccn Properties of Aerosol Particles in Boreal Forests, *Tellus Series B-Chemical and Physical Meteorology*, 53, 359-379, 2001.
- Hand, J. L., S. M. Kreidenweis, D. E. Sherman, J. L. Collett, S. V. Hering, D. E. Day, and W. C. Malm, Aerosol Size Distributions and Visibility Estimates During the Big Bend Regional Aerosol and Visibility Observational (Bravo) Study, *Atmospheric Environment*, 36, 5043-5055, 2002.
- Haywood, J. and O. Boucher, Estimates of the Direct and Indirect Radiative Forcing Due to Tropospheric Aerosols: A Review, *Reviews of Geophysics*, 38, 513-543, 2000.
- Haywood, J. M., S. R. Osborne, P. N. Francis, A. Keil, P. Formenti, M. O. Andreae, and P. H. Kaye, The Mean Physical and Optical Properties of Regional Haze Dominated by Biomass Burning Aerosol Measured From the C-130 Aircraft During Safari 2000, *Journal of Geophysical Research-Atmospheres*, 108(D13), 8473, doi:10.1029/2002JD002226, 2003.
- Huebert, B. J., T. Bates, P. B. Russell, G. Y. Shi, Y. J. Kim, K. Kawamura, G. Carmichael, and T. Nakajima, An Overview of Ace-Asia: Strategies for Quantifying the Relationships Between Asian Aerosols and Their Climatic Impacts, *Journal of Geophysical Research-Atmospheres*, 108(D23), 8633, 10.1029/2003JD003550, 2003.
- Husar, R. B., D. M. Tratt, B. A. Schichtel, S. R. Falke, F. Li, D. Jaffe, S. Gasso, T. Gill, N. S. Laulainen, F. Lu, M. C. Reheis, Y. Chun, D. Westphal, B. N. Holben, C. Gueymard, I. McKendry, N. Kuring, G. C. Feldman, C. McClain, R. J. Frouin, J. Merrill, D. Dubois, F. Vignola, T. Murayama, S. Nickovic, W. E. Wilson, K. Sassen, N. Sugimoto, and W. C. Malm, Asian Dust Events of April 1998, *Journal of Geophysical Research-Atmospheres*, 106, 18317-18330, 2001.
- Intergovernmental Panel on Climate Change (IPCC), *Climate Change 2001: The Scientific Basis*, Edited by Houghton, J., Y. Ding, D. J. Griggs, M. Noguer, P. J. van der Linden *et al.*, Cambridge Univ. Press, New York, 2001.
- Jacob, D. J., J. A. Logan, and P. P. Murti, Effect of Rising Asian Emissions on Surface Ozone in the United States, *Geophysical Research Letters*, 26, 2175-2178, 1999.
- Jaffe, D., T. Anderson, D. Covert, R. Kotchenruther, B. Trost, J. Danielson, W. Simpson, T. Berntsen, S. Karlsdottir, D. Blake, J. Harris, G. Carmichael, and I. Uno, Transport of Asian Air Pollution to North America, *Geophysical Research Letters*, 26, 711-714, 1999.

- Kotchenruther, R. A. and P. V. Hobbs, Humidification Factors of Aerosols From Biomass Burning in Brazil, *Journal of Geophysical Research-Atmospheres*, *103*, 32081-32089, 1998.
- Kreidenweis, S. M., L. A. Remer, R. Bruintjes, and O. Dubovik, Smoke Aerosol From Biomass Burning in Mexico: Hygroscopic Smoke Optical Model, *Journal of Geophysical Research-Atmospheres*, *106*, 4831-4844, 2001.
- Li, X., S. A. Christopher, J. Chou, and R. M. Welch, Estimation of Shortwave Direct Radiative Forcing of Biomass-Burning Aerosols Using New Angular Models, *Journal of Applied Meteorology*, *39*, 2278-2291, 2000.
- Liousse, C., J. E. Penner, C. Chuang, J. J. Walton, H. Eddleman, and H. Cachier, A Global Three-Dimensional Model Study of Carbonaceous Aerosols, *Journal of Geophysical Research-Atmospheres*, *101*, 19411-19432, 1996.
- Lohmann, U. and G. Lesins, Stronger Constraints on the Anthropogenic Indirect Aerosol Effect, *Science*, *298*, 1012-1015, 2002.
- Maring, H., D. L. Savoie, M. A. Izaguirre, L. Custals, and J. S. Reid, Vertical Distributions of Dust and Sea-Salt Aerosols Over Puerto Rico During Pride Measured From a Light Aircraft, *Journal of Geophysical Research-Atmospheres*, *108*(D19), 8587, doi:10.1029/2002JD002544, 2003.
- Masonis, S. J., T. L. Anderson, D. S. Covert, V. Kapustin, A. D. Clarke, S. Howell, and K. Moore, A Study of the Extinction-to-Backscatter Ratio of Marine Aerosol During the Shoreline Environment Aerosol Study, *Journal of Atmospheric and Oceanic Technology*, *20*, 1388-1402, 2003.
- Mayol-Bracero, O. L., P. Guyon, B. Graham, G. Roberts, M. O. Andreae, S. Decesari, M. C. Facchini, S. Fuzzi, and P. Artaxo, Water-Soluble Organic Compounds in Biomass Burning Aerosols Over Amazonia - 2. Apportionment of the Chemical Composition and Importance of the Polyacidic Fraction, *Journal of Geophysical Research-Atmospheres*, *107*, 8091-8106, 2002.
- McKendry, I. G., J. P. Hacker, R. Stull, S. Sakiyama, D. Mignacca, and K. Reid, Long-Range Transport of Asian Dust to the Lower Fraser Valley, British Columbia, Canada, *Journal of Geophysical Research-Atmospheres*, *106*, 18361-18370, 2001.
- Menon, S., V. K. Saxena, P. Durkee, B. N. Wenny, and K. Nielsen, Role of Sulfate Aerosols in Modifying the Cloud Albedo: A Closure Experiment, *Atmospheric Research*, *61*, 169-187, 2002.
- Merrill, J. T., M. Uematsu, and R. Bleck, Meteorological Analysis of Long-Range Transport of Mineral Aerosols Over the North Pacific, *Journal of Geophysical*

- Research-Atmospheres*, 94, 8584-8598, 1989.
- Murray, N. D., R. E. Orville, and G. R. Huffines, Effect of Pollution From Central American Fires on Cloud-to-Ground Lightning in May 1998, *Geophysical Research Letters*, 27, 2249-2252, 2000.
- Nenes, A., S. Ghan, H. Abdul-Razzak, P. Y. Chuang, and J. H. Seinfeld, Kinetic Limitations on Cloud Droplet Formation and Impact on Cloud Albedo, *Tellus Series B-Chemical and Physical Meteorology*, 53, 133-149, 2001.
- Peng, Y. R., U. Lohmann, R. Leaitch, C. Banic, and M. Couture, The Cloud Albedo-Cloud Droplet Effective Radius Relationship for Clean and Polluted Clouds From RACE and Fire.ACE, *Journal of Geophysical Research-Atmospheres*, 107, 4106-4112, 2002.
- Penner, J. E., H. Eddleman, and T. Novakov, Towards the Development of a Global Inventory for Black Carbon Emissions, *Atmospheric Environment Part a-General Topics*, 27, 1277-1295, 1993.
- Price, H. U., D. A. Jaffe, P. V. Doskey, I. McKendry, and T. L. Anderson, Vertical Profiles of O₃, Aerosols, CO and NMHCs in the Northeast Pacific During the Trace-P and Ace-Asia Experiments, *Journal of Geophysical Research-Atmospheres*, 108(D20), 8799, doi:10.1029/2002/JD002930, 2003.
- Ramanathan, V., P. J. Crutzen, J. T. Kiehl, and D. Rosenfeld, Atmosphere - Aerosols, Climate, and the Hydrological Cycle, *Science*, 294, 2119-2124, 2001.
- Raymond, T. M. and S. N. Pandis, Cloud Activation of Single-Component Organic Aerosol Particles, *Journal of Geophysical Research-Atmospheres*, 107, 4787-4795, 2002.
- Reid, J. S. and P. V. Hobbs, Physical and Optical Properties of Young Smoke From Individual Biomass Fires in Brazil, *Journal of Geophysical Research-Atmospheres*, 103, 32013-32030, 1998.
- Reid, J. S., H. H. Jonsson, H. B. Maring, A. Smirnov, D. L. Savoie, S. S. Cliff, E. A. Reid, J. M. Livingston, M. M. Meier, O. Dubovik, and S. C. Tsay, Comparison of Size and Morphological Measurements of Coarse Mode Dust Particles From Africa, *Journal of Geophysical Research-Atmospheres*, 108(D19), 8593-8621, doi:10.1029/2002JD002485, 2003.
- Roberts, G. C., P. Artaxo, J. C. Zhou, E. Swietlicki, and M. O. Andreae, Sensitivity of CCN Spectra on Chemical and Physical Properties of Aerosol: A Case Study From the Amazon Basin, *Journal of Geophysical Research-Atmospheres*, 107(D20), 8070-8088, doi:10.1029/2001JD000583, 2002.

- Roberts, G. C., A. Nenes, J. H. Seinfeld, and M. O. Andreae, Impact of Biomass Burning on Cloud Properties in the Amazon Basin, *Journal of Geophysical Research-Atmospheres*, 108(D2), 4062-4081, doi:10.1029/2001JD000985, 2003.
- Rogers, C. M. and K. P. Bowman, Transport of Smoke From the Central American Fires of 1998, *Journal of Geophysical Research-Atmospheres*, 106, 28357-28368, 2001.
- Rosenfeld, D., TRMM Observed First Direct Evidence of Smoke From Forest Fires Inhibiting Rainfall, *Geophysical Research Letters*, 26, 3105-3108, 1999.
- Ross, J. L., P. V. Hobbs, and B. Holben, Radiative Characteristics of Regional Hazes Dominated by Smoke From Biomass Burning in Brazil: Closure Tests and Direct Radiative Forcing, *Journal of Geophysical Research-Atmospheres*, 103, 31925-31941, 1998.
- Rotstayn, L. D., Indirect Forcing by Anthropogenic Aerosols: A Global Climate Model Calculation of the Effective-Radius and Cloud-Lifetime Effects, *Journal of Geophysical Research-Atmospheres*, 104, 9369-9380, 1999.
- Seinfeld, J. H., G. R. Carmichael, R. Arimoto, W. C. Conant, F. J. Brechtel, T. S. Bates, T. A. Cahill, A. D. Clarke, S. J. Doherty, P. J. Flatau, B. J. Huebert, J. Kim, K. M. Markowicz, P. K. Quinn, L. M. Russell, P. B. Russell, A. Shimizu, Y. Shinozuka, C. H. Song, Y. H. Tang, I. Uno, A. M. Vogelmann, R. J. Weber, J. H. Woo, and X. Y. Zhang, Ace-Asia - Regional Climatic and Atmospheric Chemical Effects of Asian Dust and Pollution, *Bulletin of the American Meteorological Society*, 85, 367-380, 2004.
- Seinfeld, J. H. and S.N. Pandis, *Atmospheric Chemistry and Physics: From Air Pollution to Climate Change*, 1360 pp., John Wiley, New York, 1998.
- Swietlicki, E., J. C. Zhou, O. H. Berg, B. G. Martinsson, G. Frank, S. I. Cederfelt, U. Dusek, A. Berner, W. Birmili, A. Wiedensohler, B. Yuskiewicz, and K. N. Bower, A Closure Study of Sub-Micrometer Aerosol Particle Hygroscopic Behaviour, *Atmospheric Research*, 50, 205-240, 1999.
- Swietlicki, E., J. C. Zhou, D. S. Covert, K. Hameri, B. Busch, M. Vakeva, U. Dusek, O. H. Berg, A. Wiedensohler, P. Aalto, J. Makela, B. G. Martinsson, G. Papaspiropoulos, B. Montes, G. Frank, and F. Stratmann, Hygroscopic Properties of Aerosol Particles in the Northeastern Atlantic During Ace-2, *Tellus Series B-Chemical and Physical Meteorology*, 52, 201-227, 2000.
- Vancuren, R. A., Asian Aerosols in North America: Extracting the Chemical Composition and Mass Concentration of the Asian Continental Aerosol Plume From Long-Term Aerosol Records in the Western United States, *Journal of Geophysical Research-Atmospheres*, 108, 4623-4643, 2003.

- Wang, J., R. C. Flagan, J. H. Seinfeld, H. H. Jonsson, D. R. Collins, P. B. Russell, B. Schmid, J. Redemann, J. M. Livingston, S. Gao, D. A. Hegg, E. J. Welton, and D. Bates, Clear-Column Radiative Closure During Ace-Asia: Comparison of Multiwavelength Extinction Derived From Particle Size and Composition With Results From Sun Photometry, *Journal of Geophysical Research-Atmospheres*, *107(D23)*, 4688, doi:10.1029/2002JD002426, 2002.
- Xiao, H., G. R. Carmichael, J. Durchenwald, D. Thornton, and A. Bandy, Long-Range Transport of SO_x and Dust in East Asia During the Pem B Experiment, *Journal of Geophysical Research-Atmospheres*, *102*, 28589-28612, 1997.

VITA

Yong Seob Lee was born in Pusan, Korea on November 6, 1965. He earned his Bachelor of Science degree in Earth Sciences from Pusan National University in Pusan, Korea in February 1988. He had military service as a weather forecasting officer at KwangJu and KimHae Air-force Base from August 1988 to July 1994. He received his M.S. in Earth Sciences from Pusan National University in February of 1994. He worked for Korea Meteorological Administration as a research scientist from June 1996 to July 2000.

Yong Seob currently resides with his wife YoungJin Park and two sons, MyeongShin and JaeShin in College Station, Texas. He may be reached via email at *yslee15@hanmail.net* or U.S. mail c/o Department of Atmospheric Sciences, Texas A&M University, 77843-3150.